

CYCLODEXTRIN-DERIVED POLYMER NETWORKS FOR APPLICATIONS IN
SELECTIVE MOLECULAR ADSORPTION

A Dissertation

by

BAILEY K. PHILLIPS

Submitted to the Graduate and Professional School of
Texas A&M University
in partial fulfillment of the requirements for the degree of

DOCTOR OF PHILOSOPHY

Chair of Committee,	Lei Fang
Committee Members,	Sarbajit Banerjee
	John A. Gladysz
	Mohammad Naraghi
Head of Department,	Simon W. North

December 2021

Major Subject: Chemistry

Copyright 2021 Bailey K. Phillips

ABSTRACT

The development of sustainable cyclodextrin-derived polymer networks and their potential applications in selective molecular adsorption is described. Macrocyclic-derived polymer networks represent a promising class of adsorbents that have been applied in solution phase adsorption, vapor adsorption, and vapor sensing. Despite their promising properties, these materials still face challenges in large-scale synthesis and processing.

This dissertation begins with an introduction into the properties of macrocyclic-derived functional materials and a brief overview of their applications followed by a discussion of the challenges and future perspectives for the field.

The design and synthesis of cyclodextrin-derived polymer networks (CD-PN) is described in the second chapter. This new synthetic strategy is sustainable, suitable for large-scale production, and optimizes adsorption potential by enabling a high density of macrocyclic binding sites within the polymer network. The selective adsorption of organic molecules from aqueous solutions is demonstrated with CD-PNs exhibiting remarkable selective adsorption abilities.

Chapter three describes the development of polymer nanoparticles based on CD-PN. Non-aqueous, inverse emulsion polymerization was utilized for the synthesis of cyclodextrin-derived polymer nanoparticles (CD-PNP). The nanoparticle morphology enhances the accessibility of the cyclodextrin binding sites, while enabling solution processing of CD-PNP and facilitating their feasible incorporation into functional devices.

The fourth chapter describes the vapor adsorption applications of CD-PNPs towards benzene, toluene, ethylbenzene, and xylenes (BTEX). Benzene sorption isotherms and saturated vapor adsorption experiments were utilized to explore the adsorption properties of CD-PNPs. CD-PNPs boasted comparable adsorption capacities with benchmark materials, while exhibiting significantly improved selectivity. The application of this selectivity was explored in BTEX sensing with a composite chemiresistor device. The selectivity observed in BTEX adsorption by β -CD-PNP was maintained in the composite device responses to BTEX vapors. The presence of β -CD-PNP also significantly enhanced the device sensitivity.

Overall, this dissertation presents a versatile and sustainable synthetic strategy to develop functional cyclodextrin-based polymer networks. The feasible synthetic strategy allows for in situ crosslinking to form various morphologies, such as nanoparticles, to unlock the full potential of the macrocyclic material. This work highlights the promising applications of macrocycle-derived functional materials, while demonstrating the importance of material design for optimizing the corresponding material properties.

DEDICATION

This work is dedicated to my mother and father for the unwavering support and encouragement they have always given me throughout my life.

ACKNOWLEDGEMENTS

First, I would like to thank my PhD Advisor, Dr. Lei Fang for his support, guidance, and encouragement throughout my graduate studies at Texas A&M University. He set the example of what a professional researcher is and has truly helped to shape me into the scientist I am today. I have been very lucky to have such a kind and understanding advisor to help guide me towards a research-based career.

I would also like to thank my committee member Dr. Sarbajit Banerjee for his advice and support both as a committee member and valuable collaborator. I would also like to thank my other committee members Dr. John A. Gladysz and Dr. Mohammad Naraghi for their valuable guidance and support throughout my graduate studies at Texas A&M University.

I am also thankful to my group members for their thoughtful discussions, encouragement, and for always being available to help me with their expertise. I have had the opportunity to work with many great scientists in the Fang Group including Dr. Congzhi Zhu, Dr. Jongbok Lee, Dr. Tianyu Yuan, Dr. Alex J. Kalin, Dr. Chenxu Wang, Dr. Sai Che, Dr. Xiaozhou Ji, Mariela Vazquez, Anthony U. Mu, Che-Hsuan Chang, Yirui Cao, Bo-Ji Peng, Chenxuan Li, Octavio Miranda, Mingwan Leng, and Abani. I would also like to thank Dr. Wei Hu for his invaluable contributions to my graduate studies.

I would like to thank my collaborators Prof. Sarbajit Banerjee, Prof. Mohammed Al-Hashimi, Prof. Xinman Tu, Prof. Hong-Cai Zhou, and Prof. Matthew Sheldon for their support of my graduate studies both academically and through the generous use of

instrumentation. I would also like to thank my student collaborators Hengyu Lin, Dr. Peiran Wei, Joseph Handy, and Mingzhen Zhao. I am also grateful to all the staff in the Department of Chemistry and Materials Characterization Facility at Texas A&M University for their kind support.

I would also like to thank Dr. Ray Green at Texas A&M University-Commerce for supporting me throughout my undergraduate studies and encouraging me to pursue doctoral studies. I would like to thank Dr. Stephen Starnes at Texas A&M University-Commerce for encouraging me to pursue chemistry and for giving me my first look into scientific research.

Finally, I would specially like to thank my parents, Jerrie and Deanna Phillips, for their support and encouragement through the highs and lows of graduate school. I want to thank my brother, Jacob, sister, Sydney, and brother-in-law, Jason, for always being there and supporting me. I would also like to thank the rest of my family for always encouraging me. I would like to thank my Fiancé, Victor, for being there to help me in every possible way and encouraging me when I needed it most, especially during these final months. I would also like to thank my friends that have been there for me and made graduate school fun, despite all the hard work. Lastly, I would like to thank my best friend, Laura, for always being available to support and encourage me as we went through graduate school together.

CONTRIBUTORS AND FUNDING SOURCES

Contributors

This work was supervised by a dissertation committee consisting of Professor Lei Fang (chair of committee), Professor Sarbajit Banerjee, and Professor John A. Gladysz of the Department of Chemistry, and Professor Mohammad Naraghi of the Department of Aerospace Engineering.

The initial synthetic design of β -CD-PN was investigated by Dr. Wei Hu. Raw XPS spectra and adsorption rate data (**Figure 2.3**) in chapter 2 were also acquired by Dr. Wei Hu. The TGA data depicted in chapter 2 were collected by Dr. Chenxu Wang, while the TGA data in chapter 3 were collected by Chenxuan Li. Solid-state nuclear magnetic resonance spectra in chapter 2 were obtained by Dr. Vladimir Bakhmoutov. Optical microscope images in chapter 3 were taken with the help of Dr. Peiran Wei, who also contributed valuable guidance during the early stages of emulsion formulation discussed in chapter 3 and during the design of the sensing chamber in chapter 4. Dynamic light scattering spectra were collected by Mingzhen Zhao. Abani aided in the multi-batch synthesis of α -CD-PNP and Glu-PNP and the collection of saturated vapor adsorption data for α -CD-PNP and Glu-PNP. Benzene and toluene sorption isotherms experiments were conducted by Hengyu Lin. Nanoparticle annealing was conducted by Joseph Handy. Use of the TAMU Materials Characterization Facility is acknowledged.

All other work conducted for the dissertation was completed by the student independently.

Funding Sources

This work was supported by the Qatar National Priority Research Program (NPRP10-0111-170152) and the Robert A. Welch Foundation (A-1898).

NOMENCLATURE

α -CD	α -Cyclodextrin
α -CD-PN	α -Cyclodextrin-Derived Polymer Network
α -CD-PNP	α -Cyclodextrin-Derived Polymer Nanoparticles
AC/(NAC)	Activated Carbon
AOT	Aerosol OT (Dioctyl Sulfosuccinate Sodium Salt)
β -CD	β -Cyclodextrin
β -CD-PN	β -Cyclodextrin-Derived Polymer Network
β -CD-PNP	β -Cyclodextrin-Derived Polymer Nanoparticles
BPA	Bisphenol A
BTEX	Benzene, Toluene, Ethylbenzene, and Xylenes
C[4]A	<i>p</i> -tert-butylCalix[4]Arene
C[6]A	<i>p</i> -tert-butylCalix[6]Arene
C[8]A	<i>p</i> -tert-butylCalix[8]Arene
C[4]RA	Calix[4]Resorcarene
CMP	Conjugated Microporous Polymer
CNT	Carbon Nanotubes
C _{PP}	Critical Packing Parameter
CTAB	Cetyltrimethylammonium Bromide (Cetrimonium Bromide)
DLS	Dynamic Light Scattering
EPI-CDP	Epichlorohydrin-Cyclodextrin Polymer

FET/OFET	Field-Effect Transistors/Organic Field-Effect Transistors
FTIR	Fourier Transform Infrared Spectroscopy
Glu-PN	Glucose Polymer Network
Glu-PNP	Glucose Polymer Nanoparticles
LOD	Limit of Detection
MOF	Metal-Organic Framework
MSA	Methanesulfonic Acid
MIP	Molecularly imprinted polymer
MIPNP	Molecularly imprinted polymer nanoparticles
NMP	N-Methyl-2-Pyrrolidone
NP	Nanoparticle
P-CDP	Porous β -Cyclodextrin Polymer
ppb	Parts Per Billion
ppm	Parts Per Million
QCM	Quartz Crystal Microbalance
SEM	Scanning Electron Microscopy
SS NMR	Solid-State Nuclear Magnetic Resonance
SMU	Source Measure Unit
TFN	Tetrafluoroterephthalonitrile
TGA	Thermogravimetric Analysis
VOC	Volatile Organic Compound
XPS	X-Ray Photoelectron Spectroscopy

TABLE OF CONTENTS

	Page
ABSTRACT	ii
DEDICATION	iv
ACKNOWLEDGEMENTS	v
CONTRIBUTORS AND FUNDING SOURCES.....	vii
NOMENCLATURE.....	ix
TABLE OF CONTENTS	xi
LIST OF FIGURES.....	xiv
LIST OF TABLES	xix
1. INTRODUCTION.....	1
1.1. Supramolecular Chemistry: Host-Guest Interactions.....	1
1.2. Macrocyclic Supramolecular Receptors.....	3
1.3. Macrocyclic-Based Functional Materials.....	8
1.3.1. Synthesis.....	9
1.3.2. Solution Phase Applications.....	11
1.3.3. Applications in Vapor Adsorption	14
1.3.4. Applications in Vapor Sensing.....	15
1.4. Conclusion and Perspectives.....	20
2. CYCLODEXTRIN-DERIVED POLYMER NETWORKS FOR SOLUTION PHASE ADSORPTION AND SEPARATION	22
2.1. Introduction	22
2.2. Polymer Network Design.....	23
2.3. Synthesis and Characterization	24
2.4. Solution Phase Adsorption.....	27
2.4.1. Adsorption Efficiency and Selectivity	28
2.4.2. Adsorption Capacity.....	30
2.4.3. Robustness and Recyclability.....	31
2.5. Model Column Adsorption	32

2.6. Molecular Separation	35
2.7. Conclusion.....	37
2.8. Experimental Details	38
2.8.1. General Methods	38
2.8.2. Synthetic Procedures	39
2.8.3. X-Ray Photoelectron Spectroscopy.....	41
2.8.4. Solid-State NMR	43
2.8.5. Fourier Transform Infrared Spectroscopy	44
2.8.6. Elemental Analysis Calculation	46
2.8.7. CD-PN Film Fabrication	46
2.8.8. Scanning Electron Microscopy	47
2.8.9. Structure Size Modeling.....	49
2.8.10. Adsorption Performance.....	49
2.8.11. Cyclodextrin-Based Polymer Comparison.....	54
3. CYCLODEXTRIN-DERIVED POLYMER NANOPARTICLES	59
3.1. Introduction	59
3.1.1. Polymer Nanoparticles	61
3.1.2. Nanoparticle Emulsion Polymerization.....	63
3.2. β -Cyclodextrin-Derived Polymer Nanoparticle Emulsion Polymerization	66
3.2.1. Emulsion Formulation.....	66
3.2.2. Polymerization Reaction Condition Screening	71
3.2.3. β -CD-PNP Characterization.....	75
3.3. Conclusion.....	77
3.4. Experimental Details	78
3.4.1. General Methods	78
3.4.2. Synthetic Procedures	79
3.4.3. Dynamic Light Scattering	81
3.4.4. Scanning Electron Microscope Size Distribution	81
3.4.5. Fourier Transform Infrared Spectroscopy	81
4. BTEX ADSORPTION AND SENSING BY CROSSLINKED CYCLODEXTRIN POLYMER NANOPARTICLES	83
4.1. Introduction	83
4.1.1. Environmental Context.....	83
4.1.2. BTEX Adsorption.....	84
4.1.3. BTEX Electrical Vapor Sensing.....	89
4.2. β -CD-PNP BTEX Vapor Adsorption.....	94
4.2.1. Benzene Sorption Isotherms.....	94
4.2.2. BTEX Saturated Vapor Adsorption	102
4.3. BTEX Vapor Sensing.....	107
4.3.1. Vapor Sensor Fabrication.....	107

4.3.2. Sensing Chamber Design	110
4.3.3. BTEX Sensing.....	112
4.4. Conclusion.....	118
4.5. Experimental Details.....	120
4.5.1. General Methods	120
4.5.2. Toluene Sorption Isotherms	121
4.5.3. Saturated Vapor Adsorption.....	129
4.5.4. Sensor Fabrication.....	130
4.5.5. Scanning Electron Microscopy	132
4.5.6. Sensing Chamber Construction.....	133
4.5.7. I-V Curve Characterization	134
4.5.8. BTEX Vapor Sensing.....	135
5. CONCLUSIONS.....	140
5.1. Summary	140
5.2. Perspectives.....	142
5.2.1. BTEX Sensing.....	142
5.2.2. Molecular Separation	143
5.2.3. Nuclear Waste Extraction and Storage.....	146
5.2.4. Mixed Polymer Membrane Separation.....	147
REFERENCES.....	151

LIST OF FIGURES

	Page
Figure 1.1. General structures of common macrocycles.	4
Figure 1.2. (a) Synthesis of P-CDP from β -CD and TFN. (b) N_2 sorption isotherm of P-CDP (P = equilibrium pressure; P_0 = saturation pressure). (c) The cumulative pore volume of P-CDP. (d) Structures and relevance of tested organic micropollutants. (e) Time-dependent adsorption of each pollutant (0.1 mM) by P-CDP (1 mg ml^{-1}). (f) Removal efficiency of each pollutant by P-CDP (blue), NAC (red) or EPI-CDP (green). Reprinted and adapted by permission from Nature Publishing Group: Springer Nature, <i>Nature</i> , “Rapid removal of organic micropollutants from water by a porous β -cyclodextrin polymer.” Alsbaiee, A., Smith, B., Xiao, L. et al., <i>Nature</i> , 2016, 529, 190–194. Copyright 2016 Nature Publishing Group [12].	13
Figure 2.1. (a) Synthetic scheme and proposed reaction scheme of CD-PN; (b) FTIR spectra and (c) TGA plot comparison of β -CD-PN and β -cyclodextrin.	25
Figure 2.2. Molecular structures and dimensions of the dyes tested as model analytes. (a) bisphenol A; (b) methylene blue; (c) rose bengal; (d) rhodamine B; (e) congo red.	28
Figure 2.3. Adsorption efficiency of model dye molecules by β -CD-PN as a function of time.	30
Figure 2.4. Langmuir-Freundlich adsorption isotherms of β -CD-PN towards (a) methylene blue ($R=0.9907$) and (b) bisphenol A ($R=0.9609$) (Q_{max} = maximum adsorption capacity; Q_e = equilibrium adsorption; C_e = equilibrium concentration).	31
Figure 2.5. (a) Adsorption performance of β -CD-PN to methylene blue after variable chemical treatments (Q = adsorption after treatment, Q_0 = baseline adsorption). (b) Recyclability of β -CD-PN methylene blue adsorption where cycle 0 is the first use.	32
Figure 2.6. (a) Schematic representation and digital photograph of column separation using β -CD-PN as the adsorbent (flow rate $\sim 0.4 \text{ mL/s}$); (b) structures of tested small molecular dyes; column dye adsorption data of (c) β -CD-PN (d) α -CD-PN (e) Glu-PN and (f) activated carbon (C = eluent concentration, C_0 = feed concentration). In Figure 6f, all dye adsorption data are overlapping except for Congo red.	34

Figure 2.7. Adsorption performance of a mixture of 0.005 mM methylene blue (blue data points) + 0.1 mM rhodamine B (pink data points) by (a) β -CD-PN (b) α -CD-PN (c) Glu-PN and (d) activated carbon. In Figure 3d, the data points for methylene blue and rhodamine B are overlapping.....	36
Figure 2.8. Synthesis of α - and β -CD-PN via MSA-mediated condensation.....	39
Figure 2.9. Synthesis of Glu-PN via MSA-mediated condensation.....	40
Figure 2.10. Correlation between the reaction temperature and C1s XPS peak of β -cyclodextrin (beta-CD) and β -CD-PN prepared under varying temperatures (50-110°C).....	42
Figure 2.11. XPS C1s C—C deconvoluted peaks of β -cyclodextrin and β -CD-PN prepared under varying temperatures.	42
Figure 2.12. Solid-state CP/MAS ^{13}C NMR spectra of β -CD-PN and β -cyclodextrin (β -CD).	44
Figure 2.13. FTIR spectra comparison of β -CD-PN and β -CD-PN-Film.....	45
Figure 2.14. CD-PN film fabrication method.	47
Figure 2.15. SEM image of β -CD-PN sample powderized by a commercial coffee grinder.....	48
Figure 2.16. The top view SEM images of β -CD-PN film.	48
Figure 2.17. The cross-section view SEM image of β -CD-PN film.	49
Figure 2.18. Adsorption efficiency of different organic molecules by β -CD-PN. The adsorption efficiency is an average of 4 trials.	51
Figure 3.1. Amphiphile shape factors and summary of the aggregate structures that can be predicted from the critical packing parameter C_{pp} . Reprinted from [136]....	65
Figure 3.2. General formulation and reaction scheme towards the synthesis of β -CD-PNP.....	67
Figure 3.3. (a) Structures of AOT and CTAB surfactants; (b) General illustration of the synergistic interactions between the cationic and anionic cosurfactant system.	70
Figure 3.4. Optical microscope images of β -CD-PNP synthesis emulsion (top) and scanning electron microscope images of β -CD-PNP (bottom) synthesized	

with varying emulsion phase ratios (continuous phase: dispersed phase) (a) 10:1; (b) 20:1; (c) 40:1 (continuous phase = toluene, dispersed phase = MSA).
72

Figure 3.5. (a) Scanning electron microscope images of β -CD-PNP; (b) Dynamic light scattering size distribution curve of β -CD-PNP (1, 2, and 3 are individual measurements that are averaged to determine average particle size); (c) Size distribution curve from SEM image analysis of β -CD-PNP.75

Figure 3.6. (a) FT-IR Spectra of β -CD-PN (blue) and β -CD-PNP (green); (b) Thermogravimetric analysis comparison of β -cyclodextrin (red), β -CD-PN (blue), and β -CD-PNP (green).77

Figure 4.1. Benzene sorption isotherm for β -CD-PNP. Maximum adsorption at 4.84 mmol/g (378.1 mg/g) at 0.078 atm, 294.15 K (P = absolute pressure; P_0 = saturation pressure, ~ 0.079 atm).95

Figure 4.2. Benzene sorption isotherm for annealed β -CD-PNP-400°C-1h (400°C = annealing temperature; 1 hour = annealing time). Maximum adsorption at 3.31 mmol/g (258.5 mg/g) at 0.078 atm, 294.15 K (P = absolute pressure; P_0 = saturation pressure, ~ 0.079 atm).96

Figure 4.3. Benzene sorption isotherm for annealed β -CD-PNP-800°C-1h (800°C = annealing temperature; 1 hour = annealing time). Maximum adsorption at 2.64 mmol/g (206.2 mg/g) at 0.078 atm, 294.15 K (P = absolute pressure; P_0 = saturation pressure, ~ 0.079 atm).97

Figure 4.4. Benzene sorption isotherm for α -CD-PNP. Maximum adsorption at 1.46 mmol/g (114.0 mg/g) at 0.078 atm, 294.15 K (P = absolute pressure; P_0 = saturation pressure, ~ 0.079 atm).98

Figure 4.5. Benzene sorption isotherm for Glu-PNP. Maximum adsorption at 0.16 mmol/g (12.5 mg/g) at 0.078 atm, 294.15 K (P = absolute pressure; P_0 = saturation pressure, ~ 0.079 atm).99

Figure 4.6. Benzene sorption isotherm for β -CD-PN. Maximum adsorption at 0.74 mmol/g (57.8 mg/g) at 0.078 atm, 294.15 K (P = absolute pressure; P_0 = saturation pressure, ~ 0.079 atm).100

Figure 4.7. Benzene sorption isotherm for activated carbon. Maximum adsorption at 6.27 mmol/g (489.7 mg/g) at 0.078 atm, 294.15 K (P = absolute pressure; P_0 = saturation pressure, ~ 0.079 atm).101

Figure 4.8. BTEX saturated vapor adsorption data for β -cyclodextrin-derived materials and activated carbon. β -CD-PNP-400°C-1h and β -CD-PNP-800°C-1h are annealed nanoparticles.	104
Figure 4.9. Comparison of BTEX saturated vapor adsorption data for β -/ α -cyclodextrin- and glucose-based nanoparticles and activated carbon.	106
Figure 4.10. (a) General schematic of β -CD-PNP/CNT composite chemiresistor device architecture; (b) SEM image of β -CD-PNP/CNT composite film; (c) digital photograph of β -CD-PNP/CNT composite chemiresistor device.	108
Figure 4.11. (a) General schematic of the sensing chamber design demonstrating air flow and connectivity (Note: dimensions are not to scale); (b) Digital photograph of the whole sensing chamber set up (left) with a zoomed in look at the sensing chamber itself (right).....	111
Figure 4.12. Real-time sensor response to BTEX vapors for (a) CNT control and (b) β -CD-PNP/CNT composite device. (benzene = blue, toluene = red, ethylbenzene = purple, <i>o</i> -xylene = green, <i>m</i> -xylene = grey; $\Delta R = (R_{\text{vapor}} - R_0)$, $R_0 = R_{\text{air}}$).	113
Figure 4.13. Real-time sensor response comparison for CNT control device (benzene = red, <i>m</i> -xylene = green) and β -CD-PNP/CNT composite device (benzene = blue, <i>m</i> -xylene = grey).....	115
Figure 4.14. Real-time β -CD-PNP/CNT composite response vs time to varying concentrations of benzene. Concentrations in ppm are listed above each response.	118
Figure 4.15. Toluene sorption isotherm for β -CD-PNP. Maximum adsorption at 3.31 mmol/g (305.0 mg/g) at 0.032 atm, 294.15 K (P = absolute pressure; P_0 = saturation pressure, ~ 0.032 atm).....	122
Figure 4.16. Toluene sorption isotherm for β -CD-PNP-400°C-1h (400°C = annealing temperature; 1 hour = annealing time). Maximum adsorption at 3.12 mmol/g (287.5 mg/g) at 0.032 atm, 294.15 K (P = absolute pressure; P_0 = saturation pressure, ~ 0.032 atm).	123
Figure 4.17. Toluene sorption isotherm for β -CD-PNP-800°C-1h (800°C = annealing temperature; 1 hour = annealing time). Maximum adsorption at 3.06 mmol/g (281.9 mg/g) at 0.032 atm, 294.15 K (P = absolute pressure; P_0 = saturation pressure, ~ 0.032 atm).	124

Figure 4.18. Toluene sorption isotherm for α -CD-PNP. Maximum adsorption at 2.24 mmol/g (206.4 mg/g) at 0.032 atm, 294.15 K (P = absolute pressure; P ₀ = saturation pressure, ~ 0.032 atm).....	125
Figure 4.19. Toluene sorption isotherm for Glu-PNP. Maximum adsorption at 0.09 mmol/g (8.3 mg/g) at 0.032 atm, 294.15 K (P = absolute pressure; P ₀ = saturation pressure, ~ 0.032 atm).....	126
Figure 4.20. Toluene sorption isotherm for β -CD-PN. Maximum adsorption at 1.70 mmol/g (156.6 mg/g) at 0.032 atm, 294.15 K (P = absolute pressure; P ₀ = saturation pressure, ~ 0.032 atm).....	127
Figure 4.21 Toluene sorption isotherm for activated carbon. Maximum adsorption at 5.36 mmol/g (493.9 mg/g) at 0.032 atm, 294.15 K (P = absolute pressure; P ₀ = saturation pressure, ~ 0.032 atm).	128
Figure 4.22. SEM image of β -CD-PNP/CNT composite demonstrating close interaction of nanoparticles and nanotubes.....	132
Figure 4.23. SEM images of CNT film formed via vacuum filtration.....	133
Figure 4.24. I-V curve and resistance calculation of CNT chemiresistive device.	134
Figure 4.25. I-V curve and resistance calculation of β -CD-PNP/CNT composite device.	135
Figure 4.26. Plot of baseline measurement prior to vapor exposure fitted with fifth order polynomial.	138
Figure 4.27. Plot of benzene concentration versus the sensor response. (Purple line = fitted power function; red line = extrapolated line from linear portion of fitted curve used to calculate LOD).	139
Figure 5.1. Coupling reactions utilized to synthesize a) Niraparib and b) Lasmiditan. (Coupling labels 1-3 are used for guiding the discussion; bonds formed via coupling are highlighted in red).....	145
Figure 5.2. Example separations that could be achieved with CD-PNP-based mixed polymer membranes (blue represents cellulose acetate polymer membrane; purple represents CD-PNPs).....	149

LIST OF TABLES

	Page
Table 2.1. Table of XPS C1s peak positions and areas for β -CD and β -CD-PN prepared under varying temperatures.	43
Table 2.2. FTIR peak assignments of β -CD-PN and β -cyclodextrin.....	45
Table 2.3. Comparison of crosslinked cyclodextrin-based polymers.	55
Table 3.1. β -CD-PNP emulsion polymerization reaction time screening (*Nanoparticle product not fully dried giving excess yield).	73
Table 3.2. FTIR peak assignments of β -CD-PN and β -CD-PNP.....	82
Table 4.1. Summary of benzene adsorption capacities of a variety of porous materials.	86
Table 4.2. Summary of toluene adsorption capacities of a variety of porous materials.	87
Table 4.3. Comparison of BTEX sensors with the calculated response improvement of their device compared with their control device. (*Value estimated from figures provided in manuscript; Response enhancement = Experimental Device Response/Control Device Response).....	116
Table 4.4. Benzene and toluene adsorption capacities calculated from sorption isotherms.....	129

1. INTRODUCTION*

1.1. Supramolecular Chemistry: Host-Guest Interactions

Supramolecular chemistry, regarded as the “chemistry beyond the molecule”, encompasses the noncovalent, intermolecular interactions and the subsequent molecular assemblies of both simple and complex chemical systems.¹ A variety of binding forces of varying strengths are employed in supramolecular chemistry, such as electrostatic interactions, hydrogen bonding, π interactions, and hydrophobic effects.² Strategic utilization of one or more of these binding forces can lead to the spontaneous assembly of highly ordered structures, such as micelles. Host-guest systems are among the simplest of supramolecular assemblies, however, they are the key components in many applications ranging from environmental remediation to medicine.

In host-guest chemistry, molecular recognition occurs to form a host-guest complex. The nature and strength of this binding event is a culmination of many small effects. Generally, molecular recognition is thermodynamically driven, however, due to the myriad of contributing forces, the overall binding event is complex and can be difficult to predict. Tuning the host-guest interactions of a supramolecular system seems promising for controlling molecular recognition and subsequent assemblies, however, in practice this is not easily accomplished. Enthalpy-entropy compensation, in particular, is a common phenomenon observed in molecular recognition that complicates the design of host-guest

*Reproduced (adapted) with permission from “Electrical Vapor Sensing with Macrocyclic Molecular Receptors” Phillips, B.; Banerjee, S.; Tu, X.; Fang, L. *Supramol. Chem.* **2020**, *32*, 165-177. Copyright 2020 Taylor and Francis Group. <https://www.tandfonline.com>

systems.³ This phenomenon indicates that as binding becomes more enthalpically favorable, it simultaneously becomes entropically unfavorable because as the binding strength increases, the free motion of the analyte is restricted. This inverse relationship tends to generate a plateau in binding events even when the host-guest binding interaction is modified. To overcome this plateau, interactions outside of the main host-guest interaction are essential.

Nevertheless, an understanding of the overall enthalpic and entropic contributions to a binding event can greatly aid in the strategic utilization of molecular recognition in applications. In general, the free energy of a binding event is determined by the sum of differential solvation effects and host-guest interactions.² Differential solvation take into account the favorability of the solvent-host interactions, solvent-guest interactions, and solvent-solvent interactions. Simply put, when a binding event occurs, solvent-solvent interactions replace solvent-host and solvent-guest interactions. If the solvent-guest and solvent-host interactions are less favorable than solvent-solvent interactions, then overall binding is favorable. This difference coupled with the favorability of the host-guest interaction determine the total Gibbs free energy of the solution and whether a binding event can spontaneously occur. The hydrophobic effect is a specific example of differential solvation effects at work. Beyond solvation effects, other phenomenon, such as complementarity and preorganization, can greatly affect the thermodynamics of molecular recognition.⁴ Complementarity and preorganization go hand-in-hand when describing host-guest systems. Complementarity between host and guest molecules is achieved when a host has the appropriate structure to complement the structure of the

guest. Complementarity is typically achieved via the reorganization of host molecules to favorably fit guest molecules, however the energetic cost of reorganization can be extensive leading to overall unfavorable binding. Preorganization comes into play when host molecules are structurally preorganized to fit the guest molecules so minimal reorganization energy is expended. Macrocyclic molecules, in particular, take advantage of this concept to achieve highly energetically favorable guest binding.

1.2. Macrocyclic Supramolecular Receptors

Macrocyclic molecules are cyclic macromolecules that have a well-defined, persistent shape.⁵ It is well known that macrocyclic molecules can bind specific analytes with high selectivity and affinity.⁶ The molecular recognition properties inherent in macrocycles enable their employment as supramolecular hosts for applications associated with separation,^{7,8} energy storage,⁹ drug delivery,^{10,11} environmental remediation,^{12,13} and sensing.⁶ The host-guest interactions of a macrocycle are largely governed by the size and shape of the cavity, which is determined by the structure, number, and connectivity of the repeating units.^{14,15} The preorganized, rigid or semi-rigid binding pocket also determines the selectivity of the host-guest interaction. Analytes possessing a complementary size and shape with that of the macrocycle's cavity can dock into the pocket with maximized enthalpy gain and a small entropy cost.^{2,16} Beyond size and shape, the potential for non-covalent interactions also plays an important role in macrocyclic host-guest interactions. In these cases, even weak non-covalent interactions can play crucial roles in the selectivity and affinity. One common example is the binding of an aromatic guest within a cyclophane

host possessing an aromatic core, such as calixarene and pillar[n]arene. During the host-guest interaction, the quadrupole moments of the aromatic analyte can align in a favourable manner with the quadrupole moments of the macrocycle core, leading to a highly favorable binding.² These weak interactions drive cyclophanes to bind aromatic guests selectively over aliphatic guest, although the latter possesses a better matched size with the host.²

New macrocycles are consistently being synthesized and explored, however, for the constraints of this introduction, well-established macrocycles will be predominantly discussed. There are currently 5 major classes of macrocycles, namely calixarenes, pillararenes, cucurbiturils, porphyrins, and cyclodextrins (**Figure 1.1**).

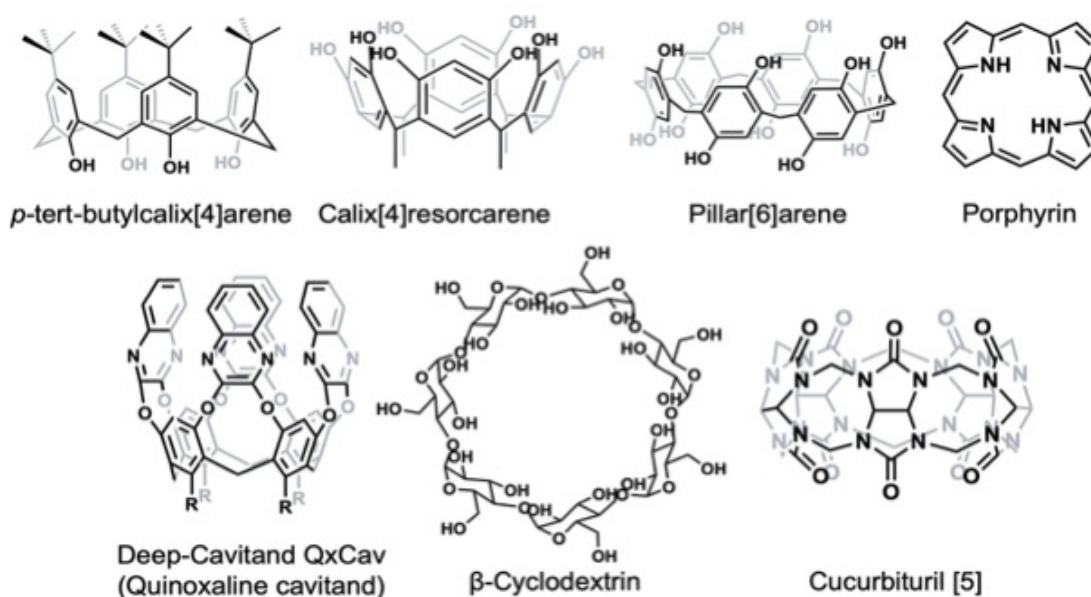


Figure 1.1. General structures of common macrocycles.

Calixarenes are among the most well-studied macrocycles to date.⁶ The flexibility, size, and conformation of calixarenes can be tailored through carefully designed synthesis and structural modification.^{18,19} Calixarenes are amphiphilic in nature, containing a hydrophobic cavity with one hydrophobic rim, typically decorated with alkyl groups, and one hydrophilic rim typically functionalized with hydroxyl groups.²⁰ Although a wide variety of calixarene derivatives have been developed, the most common types are *p*-tert-butylcalix[4]arene (C[4]A), *p*-tert-butylcalix[6]arene (C[6]A), *p*-tert-butylcalix[8]arene (C[8]A), and calix[4]resorcarene (C[4]RA). In general, calixarenes tend to have broad, semi-flexible bowl-like cavities and can take on a variety of conformations.²¹ The receptor properties of calixarenes are largely determined by their size and conformation, with more stable conformations demonstrating higher-binding affinities.^{20,22} Calixarenes have been employed as molecular receptors for metal ions, anions, and neutral organic molecules.²⁰

Deep-cavitands are a class of macrocycle derived from calixarenes, calix[4]resorcarene in particular, that tend to have a deeper binding pocket leading them to be thought of as container molecules.^{23,24} They are typically built up from a base macrocycle (*e.g.*, calix[4]resorcarene) by appending additional rows of panels yielding a deeper binding pocket for guests. If the cavity is lined with aromatic building blocks, a thin layer of negative charge along the walls would be created.²⁵ Deep-cavitands are not yet commercially available, making their applications perhaps less convenient than that of classic calixarenes. However, their deep binding pockets can lead to enhanced selectivity compared with other macrocyclic supramolecular receptors by further rejecting bulkier analytes that would be energetically less favorable.

Pillar[n]arenes are a newer class of macrocycle first reported by Ogoshi et al. in 2008. They are composed of hydroquinone ether units linked by methylene bridges at para positions.²⁶ Pillar[n]arenes can be synthesized and further functionalized in a feasible and scalable manner.²⁷⁻²⁹ They possess a more rigid conformation compared with calixarenes, despite their structural similarity, as a result of the para-connection of the methylene bridges between the aromatic building units rather than the meta-connection on calixarenes. The enhanced rigidity renders higher selectivity and affinity of pillar[n]arenes towards specific complementary guests because there is a lesser entropy penalty for binding.³⁰

Cucurbiturils are pumpkin-shaped macrocycles composed of glycoluril units with two methylene bridges on each side.³¹ They possess high thermal and chemical stability, making them ideal molecular recognition candidates in aggressive chemical environments. Like other macrocycles, cucurbiturils have a hydrophobic inner cavity, but the rim is decorated with polar carbonyl groups. The carbonyl rims allow cucurbiturils to form strong intermolecular interactions with ionic and hydrogen bond donating moieties, while the hydrophobic cavity can encapsulate non-polar aromatic or aliphatic molecular building blocks.³¹ These features have propelled extensive research in their use as molecular receptors in the solution phase.²³

Porphyrins are naturally occurring 18π aromatic macrocycles composed of four pyrrole rings connected by meso-methine carbon atoms.³² Like other macrocycles, porphyrins can be modified for specific molecular recognition and sensing applications. The coplanar porphyrin molecules can be modified with functionalization either on the β

or meso positions.^{33,34} Porphyrins are commonly used as metal coordination ligands due to their strong metal complexation abilities. In contrast to other macrocycles, the source of binding for porphyrins is typically coordination with the nitrogen moieties, rather than from the macrocyclic shape.^{35,36}

Cyclodextrins are another well-explored, naturally occurring macrocycle owing to their commercial availability and ease of modification. They are uniquely glucose-derived macrocycles with glucopyranosidic repeating units and possess a hydrophobic inner cavity with hydrophilic outer rims.³⁷ Cyclodextrin-based materials can typically be dissolved or dispersed in polar solvents, mainly water. Consequently, it can bind non-polar organic analytes in water by driving organic analytes into the cavity through hydrophobic interactions. The vapor recognition properties of cyclodextrins, however, are largely determined by their shape and size, which impact the thermodynamic parameters as discussed earlier, instead of hydrophobic interactions.⁶ The three common types of cyclodextrins, α -cyclodextrin, β -cyclodextrin, and γ -cyclodextrin, differ in the number of glucopyranoside units, which in turn affects their cavity size. Their cavity sizes range from 4.7-5.2 Å, 6.0-6.4 Å, and 7.5-8.3 Å for α , β , and γ respectively.³⁸ This range of cavity sizes causes the various cyclodextrins to have different binding affinities to the same guests. Benzene, for example, is about 4.2 Å in size. It fits tightly into the α -cyclodextrin cavity via the formation of strong Van Der Waals interactions. However, the binding also leads to a large loss in conformational entropy, making it less favorable. Benzene binds in β -cyclodextrin with higher affinity because of the more spacious cavity that causes less

entropy loss while maintaining strong van der Waals interactions. With γ -cyclodextrin, benzene has almost no binding because the cavity is too large for cooperative van der Waals interactions to occur, despite the lack of conformational restriction.¹⁵

1.3. Macrocycle-Based Functional Materials

Although macrocycles inherently have promising binding properties, applying these properties in a practical manner can be difficult. In order to better utilize the molecular recognition properties of macrocycles, they can be integrated into larger architectures to form functional materials. Macrocycles have been incorporated into a wide variety of functional, porous polymer networks and crystalline materials with the promise of combining the advantages of supramolecular hosts and porous materials for selective molecular adsorption. These functional materials are typically crosslinked, which can be achieved with a variety of techniques due to the many functional groups present on the macrocyclic backbone. While the macrocycles impart selective binding into the final material, the porous, crosslinked nature of the polymer or crystalline framework introduces additional advantages, such as high surface area for enhanced guest uptake, solvent resistance, and mechanical robustness. These materials have indeed exhibited unprecedented efficiency and selectivity that was not accessible on conventional adsorbent materials, such as activated carbon.³⁹ As this field is continually growing, a number of reviews are available for a more in depth discussion.⁴⁰⁻⁴³ The syntheses along with a few

exemplary applications of these functional macrocyclic materials are discussed in the following sections.

1.3.1. Synthesis

Owing to the plethora of functional groups present on the macrocyclic rims of cyclodextrins, calixarenes, and pillararenes, a variety of methodologies utilizing common organic synthesis techniques can be employed to construct macrocycle-based solid materials. Perhaps the simplest approach to developing macrocycle-based functional materials is through classic recrystallization. Adaptive crystals of pillararene derivatives, along with a few other macrocycles, have been developed via this method. Such adaptive crystals are nonporous but have demonstrated exemplary vapor adsorption properties that will be discussed in **Section 1.3.3**. Despite the simplistic nature of recrystallization and the promising vapor adsorption properties of adaptive crystals, there are a few pitfalls to this method for preparing macrocyclic functional materials. Recrystallization can potentially be a time-consuming process, and the recrystallization parameters need to be carefully screened and applied to obtain optimal yields. Additionally, the noncovalent structure of adaptive crystals can limit their potential applications due to a lack of mechanical robustness and poor resistance to certain solvents.

In contrast, covalent crosslinking of macrocycles can yield highly robust, functional macrocyclic polymers. EPI-CD, which consists of cyclodextrin crosslinked with epichlorohydrin, is among the earliest crosslinked macrocyclic networks. In this synthesis, crosslinking is aided by sodium hydroxide, which deprotonates cyclodextrin allowing for nucleophilic substitution and epoxide ring-opening to occur on

epichlorohydrin.⁴⁴ Although this synthesis is relatively simple with commercially available materials, one major drawback of epichlorohydrin is its flammability, toxicity, and potential as a carcinogen.⁴⁵ While it is possible, the use of such hazardous materials is not ideal, especially for larger scale applications. In addition to the synthetic drawbacks, the flexibility of epichlorohydrin as a crosslinker is unfavorable for achieving structured macrocyclic materials. The flexibility can hinder binding site accessibility via pore collapse or network interpenetration. Another common method for synthesizing cyclodextrin networks uses tetrafluoroterephthalonitrile (TFN) as the crosslinker and employs nucleophilic substitution to achieve crosslinking (**Figure 1.2a**).¹² The development of this synthesis paved the way for a new class of cyclodextrin-derived materials with excellent adsorption of micropollutants from aqueous solutions. In contrast to epichlorohydrin, TFN is aromatic and adds a level of rigidity to the polymer backbone helping to ensure pore accessibility. Although the polymer design is improved by incorporating the TFN crosslinker, the overall risk factor of the synthesis, in terms of potential hazards, is similar, if not worse than EPI-CDP. TFN and tetrahydrofuran, the solvent utilized, are both toxic and target specific body systems with tetrahydrofuran also being carcinogenic.^{46,47} Polymer networks of calixarenes have also be synthesized with common organic reactions. Sonogashira-Hagihara cross-coupling has been utilized to crosslink brominated calix[4]arenes and alkyne-rich aromatic monomers to yield porous polymer networks.^{13,48} This strategy takes advantage of the high surface areas that crosslinked, alkyne-rich materials tend to possess and couples the high porosity with macrocyclic binding. However, as with the previously mentioned syntheses, the

Sonogashira-Hagihara coupling reaction employs toxic, flammable, and potentially carcinogenic reagents, such as tetrahydrofuran and N,N-Diisopropylethylamine, making it less favorable for scalability. The brief overview of these methods highlights the need for further innovation towards more sustainable, non-toxic synthetic routes to achieve high-performing, robust macrocyclic functional materials.

1.3.2. Solution Phase Applications

Owing to the hydrophobicity of their inner cavity, macrocycle-derived functional materials have been widely explored for aqueous solution adsorption applications.²³ The hydrophobic effect is the key driving force behind the excellent selective adsorption properties in aqueous solutions demonstrated by macrocyclic-based materials. As mentioned in **Section 1.1.**, the hydrophobic effect is an example of differential solvation effects at play. Although seemingly counterintuitive, the hydrophobic effect is primarily entropically driven.^{2,49} This favorable binding has been widely exploited by macrocyclic functional materials that have been applied in the removal of organic pollutants from aqueous solutions. Pioneering work reported in 2016 demonstrated the development of a porous β -cyclodextrin-based polymer (P-CDP) with excellent adsorption performance towards common organic pollutants.¹² In this work, β -cyclodextrin was crosslinked with tetrafluoroterephthalonitrile (TFN) to form a mesoporous polymer network with cyclodextrin binding sites built into the polymer backbone (**Figures 1.2a and 1.2b**). P-CDP exhibited excellent adsorption efficiency towards a myriad of common organic pollutants (**Figures 1.2d and 1.2e**). P-CDP also outperformed both activated carbon (NAC) and EPI-CDP, which prior to this work was the most common cyclodextrin-based

polymer (**Figure 1.2f**). This work demonstrated the great potential of cyclodextrin polymers in micropollutant adsorption and inspired a new class of cyclodextrin-TFN materials that are continually being explored.⁵⁰⁻⁵²

Calixarene- and pillararene-derived materials have also been explored for application in solution phase adsorption to remove organic pollutants from aqueous solutions. Sonogashira-Hagihara cross-coupling has been implemented to produce polycalix[4]arenes with various aromatic crosslinkers,¹³ while a pillar[5]arene-based 3D network was synthesized via crosslinking with *p*-phenylenediamine and further functionalized with hydrophilic moieties.⁵³ These materials exhibit high surface areas, fast adsorption rates, and adsorption efficiencies beyond activated carbons towards a variety of organic pollutants. Mixed macrocycle materials are also being explored to modify and improve adsorption performance towards a variety of pollutants.^{54,55} In general, these materials are promising for practical application with fast adsorption rates and high adsorption capacities. With the breadth of this field there are a number of reviews available for further reference.^{23,42,56-58} Although these examples demonstrate the excellent solution adsorption potential of macrocyclic materials, there is still room for improvement in terms of performance and scalable, sustainable syntheses. In addition to pure adsorption applications, a broad spectrum of macrocyclic materials has been developed for solution phase sensing.⁵⁹⁻⁶² However, within the scope of this introduction, these materials will not be discussed.

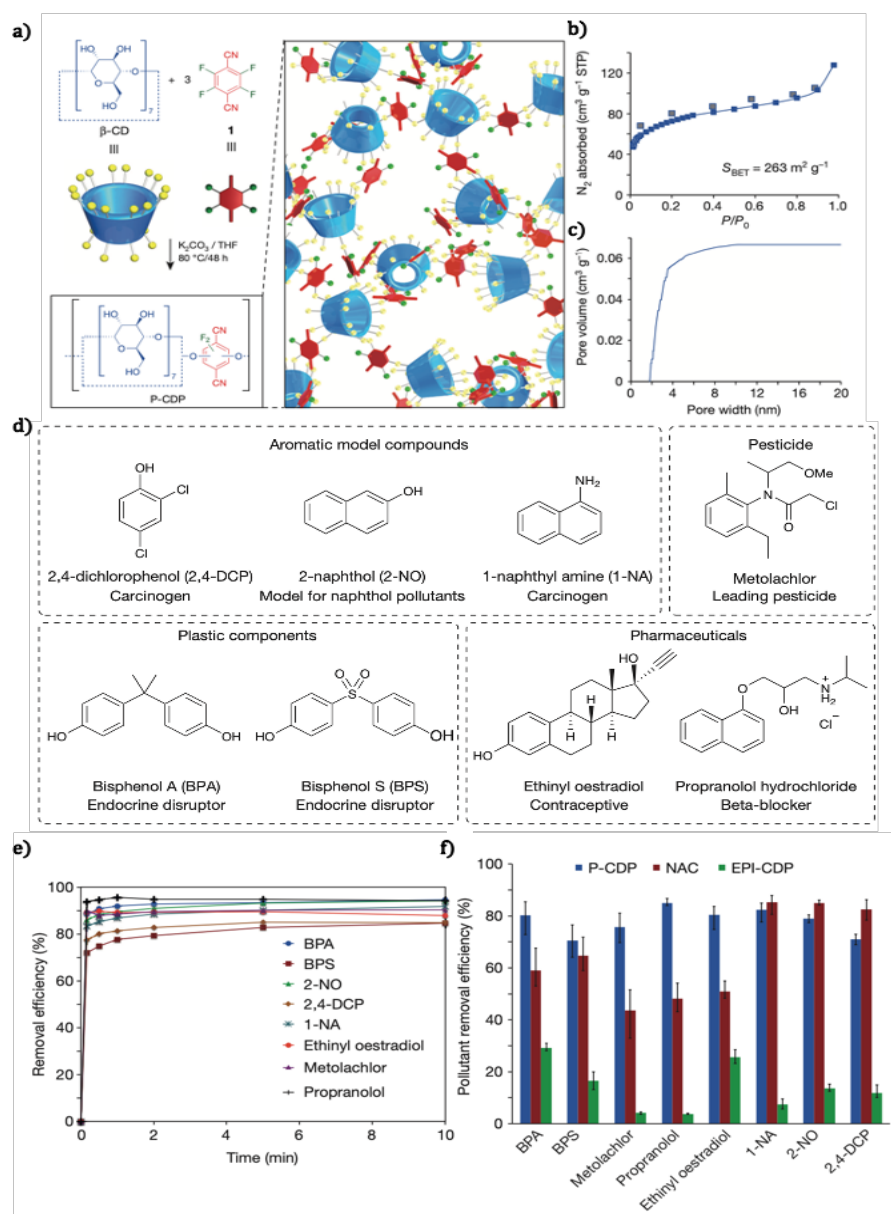


Figure 1.2. (a) Synthesis of P-CDP from β -CD and TFN. (b) N_2 sorption isotherm of P-CDP (P = equilibrium pressure; P_0 = saturation pressure). (c) The cumulative pore volume of P-CDP. (d) Structures and relevance of tested organic micropollutants. (e) Time-dependent adsorption of each pollutant (0.1 mM) by P-CDP (1 mg ml⁻¹). (f) Removal efficiency of each pollutant by P-CDP (blue), NAC (red) or EPI-CDP (green). Reprinted and adapted by permission from Nature Publishing Group: Springer Nature, *Nature*, “Rapid removal of organic micropollutants from water by a porous β -cyclodextrin polymer.” Alsaiee, A., Smith, B., Xiao, L. et al., *Nature*, 2016, 529, 190–194. Copyright 2016 Nature Publishing Group [12].

1.3.3. Applications in Vapor Adsorption

Rather than the differential solvation effects that drive solution phase adsorption, the preorganization inherent in macrocyclic materials drives the vapor phase inclusion of guests into the inner cavity. Selective vapor adsorption with macrocycle-based functional materials is currently dominated by adaptive crystals, which rely on a change in the crystal structure of the larger crystal architecture to differentiate organic vapors. The observed change in the crystal structure is initiated by preferential guest binding; this preferential binding has been exploited for applications in molecular separation.⁴⁰ Pillararenes in particular have been extensively employed as adaptive crystals for vapor phase separation.

Due to their rigid nature and hydroxylated rims, pillararenes often self-assemble into ordered structures. These materials have shown highly selective gas adsorption properties. Early work demonstrated the self-assembly of pillar[5]arene into an ordered supramolecular organic framework, which displayed selectivity towards carbon dioxide over nitrogen and methane.⁶³ More recently, adaptive pillar[n]arene crystals have demonstrated the ability to separate very similar compounds, such as styrene and ethylbenzene along with dihalobenzene isomers and xylene isomers, based on the inclusion or exclusion of the analytes in the macrocyclic cavity.^{7,64,65} Beyond adaptive crystals, macrocycles have also been incorporated into other crystalline materials like metal-organic frameworks (MOF). Cyclodextrin, in particular, has been widely explored as CD-MOF materials. These materials display promising vapor adsorption selectivity, with a γ -cyclodextrin-based CD-MOF differentiating *o*-xylene from its *p*-/*m*-xylene isomers.⁶⁶ This particular separation is unique, because although separation of xylene

isomers is commonly explored, typically selectivity is towards *p*-xylene while rejecting *o*/*m*-xylene isomers.^{65,67-69} The gas adsorption potential of calixarene-derived MOFs has also been explored demonstrating promising NO₂ adsorption.^{70,71}

Macrocycles have also been incorporated into polymer networks and employed in gas phase separations. For example, pillar[5]arene incorporated into conjugated microporous polymers (CMP) demonstrated excellent methane/propane separation by taking advantage of the porous nature of CMP and the selectivity of pillar[5]arene.⁷² Macrocyclic-based polymers that have been utilized in solution phase applications can also be impactful in vapor phase applications. P-CDP, for example, has been functionalized onto cotton fabric and employed in styrene vapor adsorption demonstrating the greatly enhanced adsorption properties that the cyclodextrin-based polymer can impart into fabrics.⁷³ Although the application of macrocyclic-based materials in vapor adsorption is a highly promising field, it has not yet been thoroughly explored. With that, no exhaustive reviews over the topic are available, however, a number of review papers touch on the topic and can be used for further reference.^{43,74-76}

1.3.4. Applications in Vapor Sensing

Macrocyclic molecules have been widely used as the receptors for sensing a variety of analytes because they can impart a high level of selectivity into the sensor based on their host-guest binding interactions. With an enforced and pre-organized shape, the often-rigid cavity in macrocyclic receptors thermodynamically enables the recognition of the subtle differences in size and shape among analytes, therefore preferentially binding the one with a complementary size and shape with that of the cavity.⁶ If carefully selected,

macrocyclic receptors can be highly selective and boast strong binding affinities for use in sensing.

Vapor sensing has become an important technique in many different fields. Such sensors based on graphene have been applied in environmental and industrial monitoring, medical diagnosis, and national security.⁷⁷ In these fields, efficient, accurate quantification of specific analytes is of the utmost importance for vapor sensing. At present, many vapor detection techniques rely on an on-site sampling followed by off-site analysis, which can be expensive and time-consuming.⁷⁸ Real-time monitoring is preferred for many applications, particularly detection of toxins, biomarkers, or explosives, to ensure safety.

The vapor sensing mechanism involves three general steps. First, kinetic adsorption of the analyte onto the receptor occurs, leading to a typically fast, sharp signal response, which indicates the binding of the analyte. Subsequently, the initial kinetic response is followed by a dynamic diffusion process consisting of simultaneous adsorption and desorption of the analyte within active layer of the molecular receptors. Finally, flushing with air facilitates total analyte desorption to restore the initial condition of the sensor, thus allowing its repeated use.^{79,80}

For vapor sensing, selectivity is an important yet challenging factor because most gas-phase analytes are similar to the interfering molecules in terms of their constitutional structure.⁸¹ Based on their ability to distinguish subtle analyte structural variances, macrocycles are ideal candidates to impart selectivity into vapor sensors. In addition to challenges in selectivity, signal transduction of the vapor binding events is not intrinsic and represents another major challenge. Different types of signal transduction have been

used to tackle this challenge leading to the development of macrocyclic fluorescence sensors,⁸² mass transducers,^{83,84} and electrical-based sensors.

Mass transducers, such as quartz crystal microbalances (QCM), were among the earliest methods to employ macrocycles in vapor sensing. In this technique, a voltage is applied to a piezoelectric material, namely quartz, causing it to oscillate at a specific frequency.⁸⁵ When there is a mass change on the QCM, i.e., adsorption occurs, the oscillation frequency change is directly related to the change in mass via the Sauerbrey equation. In a pioneering study, Lai et al. functionalized a QCM with cyclodextrin derivatives for sensitive benzene detection.⁸³ More recently QCM devices have been decorated with pillararenes derivatives to achieve sensitivity to a variety of organic vapors with the potential to discriminate benzene and toluene.⁸⁴

Fluorescence-based sensing has also commonly employed macrocycles produce highly sensitive and selective sensors.⁸⁶ In fluorescent-based sensing, fluorescence quenching is the most common sensing mechanism, however other mechanisms, such as fluorescence turn-on, spectral shifts, and lifetime changes, have also been explored. Relating these changes in fluorescence to the concentration of a specific analyte constitutes the basis of fluorescence sensing. In recent years, calixarene-based materials have been explored for fluorescence-based vapor sensing.⁸⁷ In one example, calix[4]arene units were incorporated into phenylene-alt-ethynylene-carbazolylene polymers and applied in solution and vapor sensing.⁸⁸ The solid-state sensor demonstrated highly sensitive quenching responses to nitroaromatic compounds indicating its potential in explosive detection.

Electrical vapor sensing also commonly enlists the selectivity of macrocycles. In electrical vapor sensors, the binding event triggers an electrical response, such as a change in the current/resistance, impedance, or capacitance of the device. The intensity of the response can be correlated with the amount of analyte that has been bound by the recognition sites allowing the detection and quantification of the present analyte. The tandem binding event and electrical response occurs almost instantaneously, allowing electrical vapor sensors to be fast-responding, real-time monitors. The signal change is dependent upon the molecular recognition, the conductive material, and the device architecture. The most common types of electrical vapor sensor devices are field-effect transistors (FET) and chemiresistors, which all share a similar sensing mechanism: a binding event modulates the electrical properties of the conducting/semiconducting active material to output the signal.⁸⁹ These various device architectures, along with others, have been used in other commercial applications extensively. In this context, electrical vapor sensors can be potentially mass produced with low-cost by taking advantage of the already existing technology and infrastructure of the FET and resistor industry. Despite the significant challenges imposed by electrical vapor sensors, recent advances in related fields highlight their simplicity, low-cost production, energy efficiency, and fast responses, demonstrating their potential as practical, real-time monitors for a variety of vapor analytes.^{21,69,89,90}

Like other sensing platforms, macrocycles can be incorporated into the device architecture of electrical vapor sensors to endow the device with selectivity in sensing. For example, in 2010, Sokolov et al. modified an organic field-effect transistor (OFET) with

coatings of calixarene macrocycles to achieve sensitivity and selectivity towards a series of volatile organic compounds (VOC). C[8]A and C-methylcalix[4]resorcarene (CM[4]RA) were both used to modify the OFETs to compare the effect of cavity size on device selectivity. Thin films of calixarene macrocycles were thermally evaporated onto OFET devices. The resulting change in current in response to a series of VOCs was monitored for the bare OFET, C[8]A-functionalised OFET, and CM[4]RA-functionalised OFET. The bare OFET device didn't show selectivity towards any specific analytes tested. In contrast, both C[8]A- and CM[4]RA- functionalised sensors showed significantly enhanced sensitivity. The C[8]A-sensor showed high selectivity towards ethyl acetate, while the CM[4]RA-functionalised devices displayed high sensitivity towards isopropanol. This preferential binding demonstrates how the preorganization of macrocycles varying in size and shape can yield different selectivities.⁹⁰

Macrocycle-derived polymer materials have also been incorporated into electrical vapor sensors. In 2007, Zeng et al. prepared a composite polymer-based gas sensor incorporating β -cyclodextrin as a selective sensing unit.⁸¹ The sensor was fabricated by first synthesizing a carbon black filled waterborne β -cyclodextrin-block-polydiethylene glycol hexandioic ester copolymer (β -CD-block-PDEA). This composite mixture was then drop cast onto prefabricated electrodes. The change in resistance was monitored for the vapors of a range of volatile organic solvents with varying sizes and permittivity values. For low permittivity molecules, there was no trend observed between permittivity and sensor response, while the smaller size induced stronger responses. These data indicated that energetically favourable size complementarity is a more important factor for this type

of vapor sensor than hydrophobic based interactions. For high permittivity molecules, on the other hand, neither permittivity nor size showed any correlation with the sensor response, indicating that more polar, high permittivity molecules had little to no interaction with the hydrophobic cyclodextrin cavity. These data further demonstrate the complexity of vapor sensing highlighting the importance of preorganization, size complementarity, and favourable hydrophobicity all together.

These examples give a brief insight into electrical vapor sensing and vapor sensing in general. However, many reviews discussing vapor sensing are available from varying perspectives for further reference.^{6,17,20,86,91,92}

1.4. Conclusion and Perspectives

In summary, macrocycles represent a promising class of selective supramolecular receptors. Their persistent shape and intrinsic cavities allow macrocycles to selectively bind analytes with a complementary size and shape. These properties can be exploited in functional materials through the development of dynamic crystalline materials and polymer networks. Macrocycle-derived functional materials have proven to be promising in a variety of adsorption-based applications in both solution and vapor phases. Despite the great advancement of macrocyclic materials, the development of sustainable, scalable syntheses towards functional macrocycle-based materials is still needed. Many of the current technologies utilize synthetic pathways that require toxic and expensive reagents, making them less favorable for practical application, even with excellent adsorption

properties. Beyond more practical syntheses, exploration into the vapor adsorption properties of macrocycle-derived polymers is also desired. Polymer materials present a myriad of advantages in terms of robustness, processibility, and performance. However, macrocycle-derived polymers have so far been primarily applied in solution phase owing to their enhanced robustness, yet the same advantages should apply in vapor phase applications.

Finally, continuing innovation in polymer design can optimize the properties of macrocycle-based polymer materials. Currently, covalently crosslinked materials are favorable in terms of robustness. However, the addition of a crosslinker leads to a dilution effect of the macrocyclic binding sites within the material by introducing larger pores and separating the macrocycle monomers. Syntheses directly crosslinking macrocycles could potentially lead to functional materials with a higher density of macrocyclic binding sites, while maintaining the robustness inherent in crosslinked materials. Additionally, direct crosslinking could improve the scalability of the synthesis by incorporating fewer reagents and removing the need for hazardous crosslinkers. With further development of sophisticated polymer materials that have macrocyclic molecular receptors built into the backbone, the design of functional composite materials can follow. There are many current challenges in environmental remediation that require robust, selective, and scalable materials. The development of such materials presents exciting and rewarding research opportunities for future exploration.

2. CYCLODEXTRIN-DERIVED POLYMER NETWORKS FOR SOLUTION PHASE ADSORPTION AND SEPARATION*

2.1. Introduction

Because selective molecular adsorption is a critical component to many applications, including but not limited to sensing, separation, and environmental remediation, the development of selective adsorbents is ongoing.^{17,23,93} Practical applications of these adsorbents typically require the materials to be robust under operational conditions, recyclable, and inexpensive to produce.^{94,95} In this context, porous materials have been extensively investigated with crosslinked porous polymer networks being particularly advantageous due to their structural tunability, facile synthesis, and resistance to dissolution.⁹⁵⁻⁹⁷ In recent years, macrocycles have been incorporated into crosslinked networks to combine their supramolecular binding properties with the robustness inherent in crosslinked materials.^{13,53} With this strategy, materials possessing unprecedented efficiency and selectivity, which was not previously accessible with conventional adsorbents, have been developed.³⁹

Despite exciting recent advancements in supramolecular host-incorporated adsorbent polymers, it is still challenging to deploy them in large-scale applications partially due to the need for inexpensive, efficient, and environmentally friendly synthesis

*“Cyclodextrin-Derived Polymer Networks for Selective Molecular Adsorption” Phillips, B.; Wang, C.; Tu, X.; Chang, C.-H.; Banerjee, S.; Al-Hashimi, M.; Hu, W.; Fang, L. *Chem. Commun.* **2020**, *56*, 11783-11786. Reproduced and adapted from Ref. [103] with permission of The Royal Society of Chemistry.

of these materials. From a perspective of macrocyclic starting materials, cyclodextrins are ideal because they can be produced in a sustainable, low-cost manner.^{98,99} Cyclodextrins are composed of glucopyranosidic repeating units that possess rich hydroxyl functional groups on the outer side of the macrocycle facilitating the use of simple organic reactions to incorporate them into larger architectures. In addition, the inner cavity of cyclodextrin is relatively hydrophobic endowing them with unique features having a hydrophobic cavity lined with hydrophilic groups. These favorable attributes, along with their known supramolecular host behavior, inspired the design of a new cyclodextrin-derived polymer network in which the desirable sustainability and scalability for practical application are conserved.

2.2. Polymer Network Design

The amphiphilic nature of cyclodextrins endow their derivative materials with unique properties. The outer rims of cyclodextrin are rich in hydroxyl functional groups enabling potential self-condensation reactions for crosslinking without the addition of any other crosslinking partner. Once crosslinked into a solid network, the juxtaposition of the hydrophobic cavity and hydrophilic outer side of the macrocycle typically yields a hydrophilic polymer network that can selectively capture hydrophobic guest molecules inside the cyclodextrin cavity.² Herein, by taking full advantage of these features of cyclodextrin, we developed an extraordinarily facile and scalable synthesis of linker-less cyclodextrin-derived polymer networks (CD-PNs), and demonstrated their excellent selectivity towards adsorbing organic molecules in aqueous media.

The synthesis of CD-PN was designed with sustainability in mind employing only green reagents. The simple direct crosslinking of cyclodextrin carries a number of advantages for practical adsorption applications. First, the important macrocyclic constitution of the cyclodextrin unit was expected to be preserved during the crosslinking, so that the resulting CD-PNs inherit the capability of selective guest adsorption from cyclodextrin. Second, this reaction takes advantage of using inexpensive and non-toxic methanesulfonic acid (MSA) as the catalyst and solvent simultaneously, without the addition of any other reagent, ensuring the sustainability and scalability of the synthesis.^{100,101} Last but not least, the cyclodextrin monomer is crosslinked directly with no additional spacer affording the CD-PNs with the theoretical potential for a maximized density of macrocyclic binding sites. Overall, this approach affords robust materials, while being highly sustainable and scalable for future industrial application.

2.3. Synthesis and Characterization

To directly crosslink β - or α -cyclodextrin macrocycles, an MSA-mediated condensation reaction was developed to afford the polymer networks β -CD-PN and α -CD-PN, respectively (**Figure 2.1a**). During the synthesis, cyclodextrin monomers were dissolved in MSA and heated at 110°C for ~48 h without any protection from water or oxygen, followed by simple washing with water as the work up. In this acid-promoted reaction, the hydroxyl groups on glucopyranoside units from different cyclodextrin monomers undergo ether condensation to crosslink them into a polymer network.

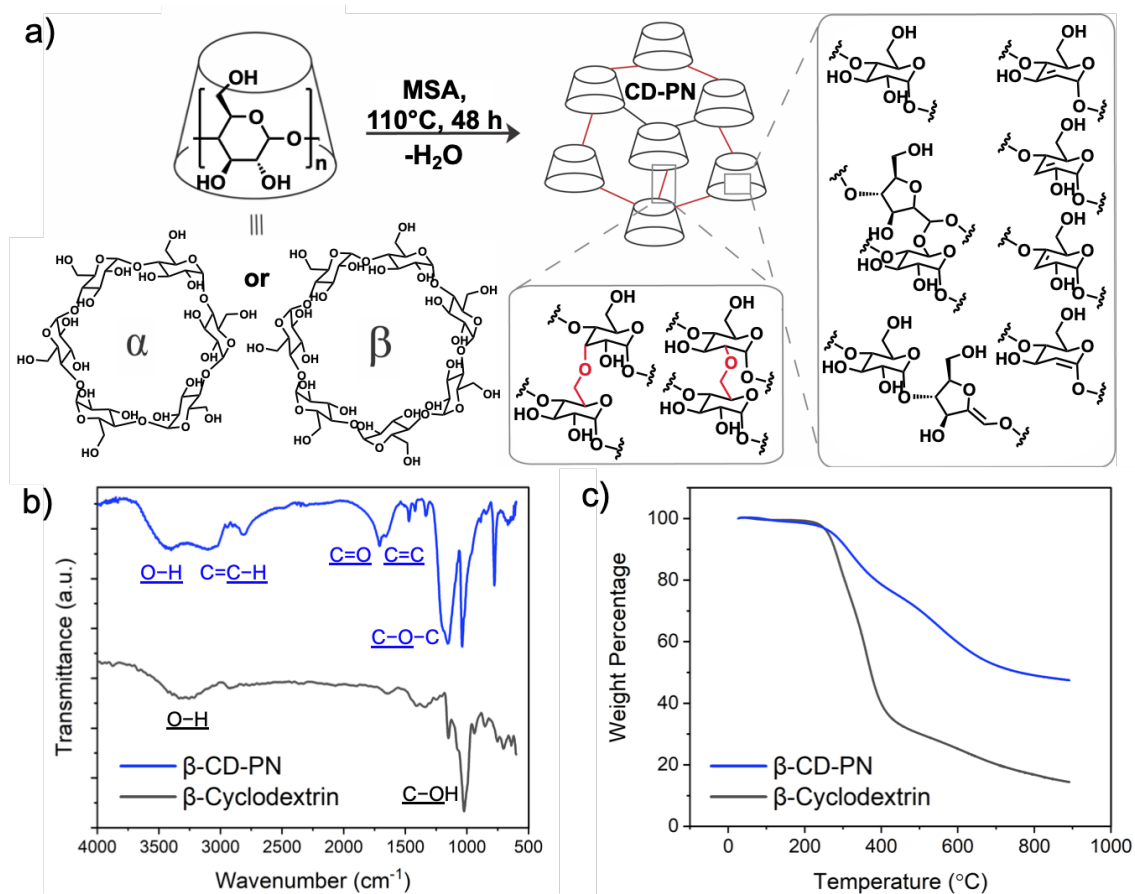


Figure 2.1. (a) Synthetic scheme and proposed reaction scheme of CD-PN; (b) FTIR spectra and (c) TGA plot comparison of β -CD-PN and β -cyclodextrin.

The formation of the ether linkages is supported by the emergence of a strong C—O—C stretching peak at 1157 cm^{-1} in the FTIR spectra of CD-PNs (**Figure 2.1b and Table 2.2**).¹⁰³ At the optimized temperature of 110°C , the water byproduct is driven out of the solution to push forward the ether condensation via thermodynamic control. The solid product is insoluble in almost all known solvents, indicating its fully crosslinked nature. Besides dehydrative ether condensation, dehydrative β -elimination also takes

place during the reaction, affording sp^2 -carbons in the product. However, excessive β -elimination is avoided at the optimized temperature of 110°C in order to prevent the formation of an overly hydrophobic material that would not be favorable for aqueous applications. The emergence of sp^2 carbon is evidenced by the C1s peak at 284 eV in XPS and the down field shifted resonance peaks in the solid-state NMR spectrum (**Figures 2.11 and 2.12**). The extent of dehydration, associated with both ether condensation and β -elimination, was estimated based on the isolated yields and elemental analysis data. Taking β -CD-PN as an example, the isolated yield is calculated to be 64% based on the mass of the monomer, corresponding to ~ 22.69 mol of water loss per mol of β -cyclodextrin. On the other hand, by comparing the elemental composition of β -CD-PN (Found: C, 66.50; H, 4.70; O, 28.00; S, <0.05%) with the starting material, β -cyclodextrin (Found: C, 44.45; H, 6.22; O, 49.30%), one can estimate ~ 19.46 mol of water loss per mol of β -cyclodextrin in the reaction. For α -CD-PN, the molar water loss per α -cyclodextrin molecule was estimated to be 17.43 mol by yield (68%). These values agree well with each other despite the small error in the measurement of yield and elemental analysis. The dehydration also leads to enhanced carbonization yield of β -CD-PN (47%) compared with the β -cyclodextrin starting material (14%) (**Figure 2.1c**). It is worth noting that other strong acid-promoted side-reactions, such as isomerization of the glucopyranosidic building block into a glucofuranoside structure through ring opening and re-annulation, are also possible (**Figure 2.1a**).¹⁰⁴ However, the overall pristine nature of this reaction, involving only solvent and monomer, allows for versatile and amenable solution

processing of the material through *in situ* crosslinking¹⁰⁵ into a desired morphology, such as well-defined smooth thin films that maintain the structure and performance of the bulk material (Figures 2.13, 2.14, 2.16, and 2.18).

2.4. Solution Phase Adsorption

The cyclodextrin backbone of CD-PN endows it with inherent supramolecular binding sites. As mentioned above, the direct crosslinking of cyclodextrin potentially affords CD-PN with a higher density of binding sites compared with other cyclodextrin materials that possess additional crosslinkers. With this in mind, the adsorption properties of CD-PN were investigated. The N₂ adsorption isotherm of β -CD-PN was measured to examine the surface area of the material, however β -CD-PN showed very low measurable surface area (<10 m²/g). Despite this lack of apparent porosity, the presence of macrocyclic binding sites with defined sizes promises CD-PNs to be good selective adsorbent materials for small molecules dissolved in water, as has been noted for other cyclodextrin-based polymers. The adsorption selectivity and capacitance were investigated using model aqueous solutions of small molecular dyes. The sizes of the dye molecules were estimated to better understand the adsorption potential of both α - and β -CD-PN (**Figure 2.2**). The internal cavity sizes of α - and β -cyclodextrin range from 4.7-5.3 Å and 6.0-6.5 Å, respectively.¹⁰⁶ With these dimensions in mind, along with previous reports, it is expected that bisphenol A and methylene blue should be adsorbed by β -CD-PN, while the other molecules are rejected.

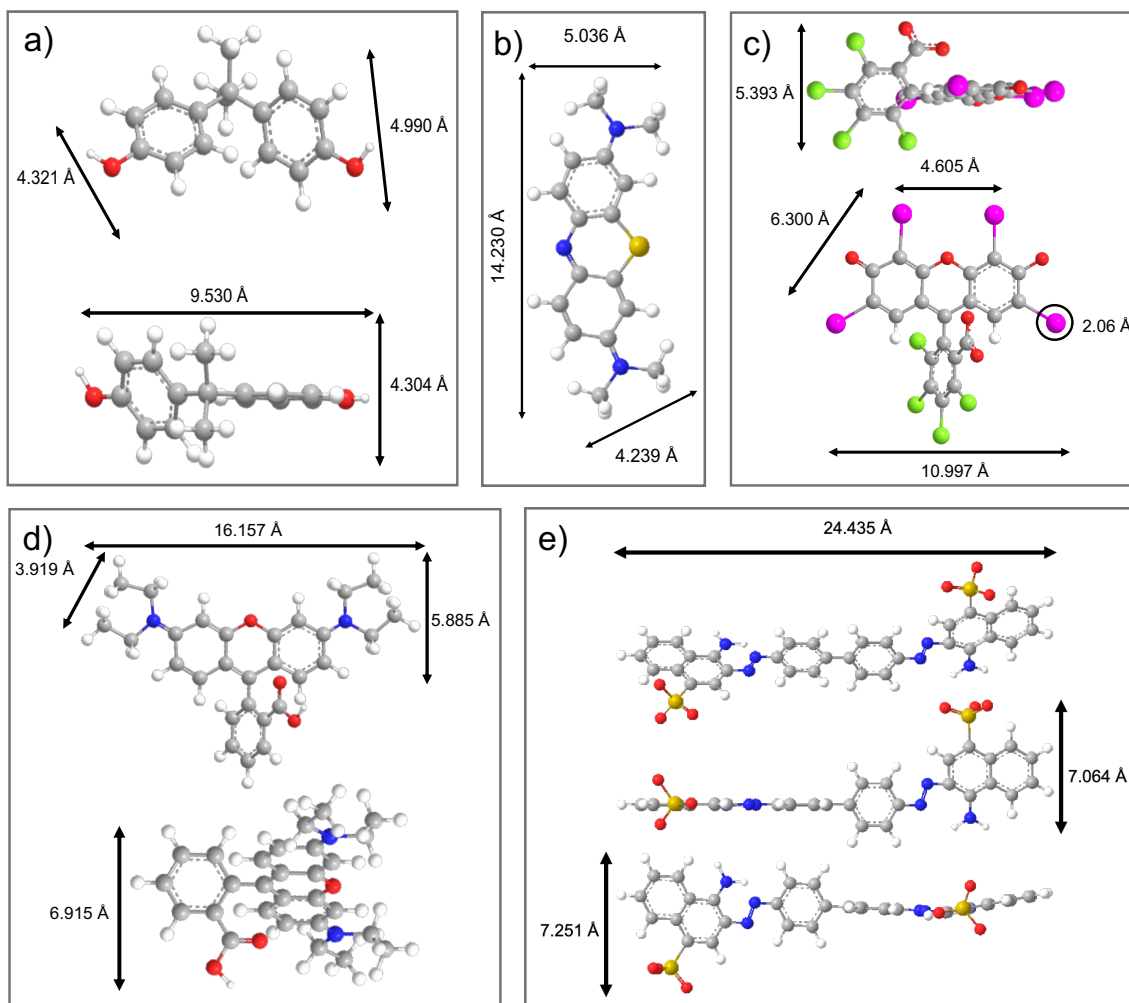


Figure 2.2. Molecular structures and dimensions of the dyes tested as model analytes. (a) bisphenol A; (b) methylene blue; (c) rose bengal; (d) rhodamine B; (e) congo red.

2.4.1. Adsorption Efficiency and Selectivity

To investigate the predicted adsorption properties, the β -CD-PN materials were first ground into powders and subsequently added to the tested dye solution while stirring with UV-vis absorbance spectroscopy being recorded to determine the adsorption

efficiency. As expected, organic molecules that are smaller than the β -cyclodextrin cavity, such as bisphenol A (BPA) and methylene blue, are efficiently adsorbed by β -CD-PN with fast adsorption kinetics (**Figure 2.3**), while larger dye molecules, such as rose Bengal, rhodamine B, and Congo red, are not adsorbed. These expected results confirm the presence of the cyclodextrin internal cavity, further indicating that it is not destroyed despite the harsh synthetic conditions. In contrast, no significant adsorption of the dye molecules was observed for α -CD-PN owing to its smaller cavity size. Although β -CD-PN displayed fast adsorption properties, it is important to note that the kinetics are limited by diffusion, morphology, and particle size, so these measurements may not be completely representative of an intrinsic chemical property of the material. However, the confirmed selectivity of β -CD-PN inspired further investigation into its properties.

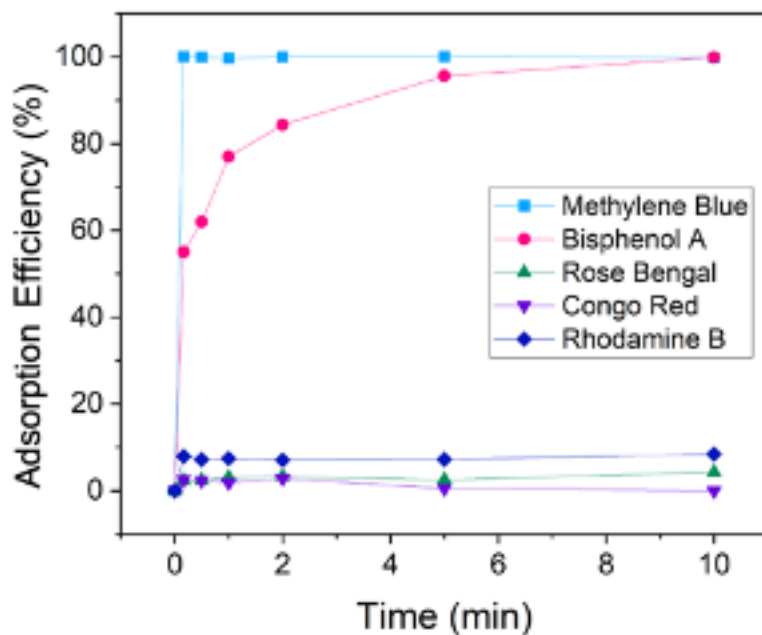


Figure 2.3. Adsorption efficiency of model dye molecules by β -CD-PN as a function of time.

2.4.2. Adsorption Capacity

The adsorption capacity of β -CD-PN was examined to gain a better understanding of its potential applications. Langmuir-Freundlich adsorption isotherms of β -CD-PN exhibited remarkably high adsorption capacities for methylene blue and BPA at 177.8 and 387.9 mg/g, respectively, (**Figure 2.4**). The BPA adsorption capacity surpasses those reported on most other cyclodextrin-derived polymer networks (**Table 2.3**), supporting the hypothesis that the linker-less β -CD-PN has the potential to reach a maximized density of binding sites compared to those requiring a crosslinker during synthesis.

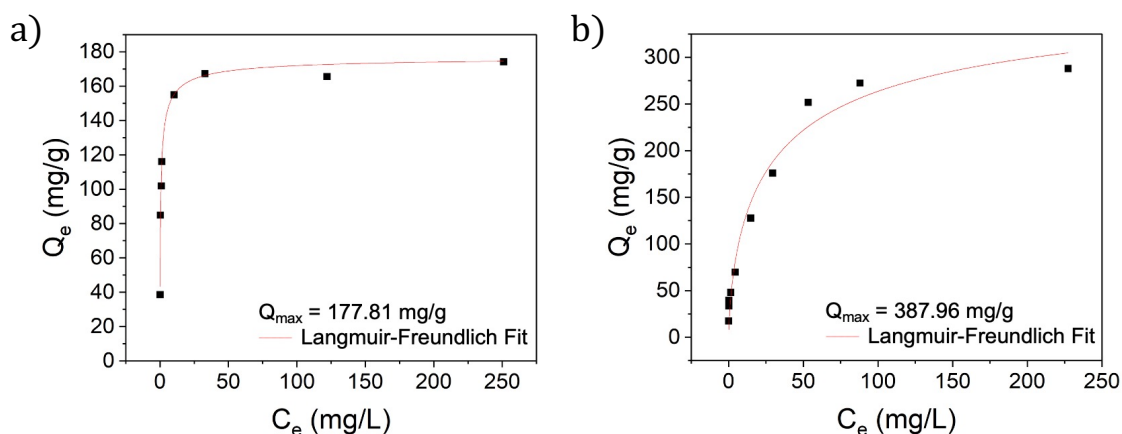


Figure 2.4. Langmuir-Freundlich adsorption isotherms of β -CD-PN towards (a) methylene blue ($R=0.9907$) and (b) bisphenol A ($R=0.9609$) (Q_{max} = maximum adsorption capacity; Q_e = equilibrium adsorption; C_e = equilibrium concentration).

2.4.3. Robustness and Recyclability

The crosslinked nature of β -CD-PN endows the polymer network with significantly enhanced robustness that is not inherent in the cyclodextrin monomers. β -CD-PN showed remarkable chemical resistance with little to no loss in methylene blue adsorption performance after exposure to strong aqueous acid or base, or strong organic solvents (**Figure 2.5a**). It also exhibited exemplary recyclability after regeneration by simply washing with methanol from a saturated adsorbed state. In fact, the adsorption performance was not only maintained but also slightly improved after being regenerated from washing (**Figure 2.5b**), presumably due to a decreased particle size after washing and wearing that rendered the binding sites more accessible to the adsorbate. The simple washing regeneration procedure for β -CD-PN is a low energy process furthering its

industrial practicality, especially compared with activated carbons, which typically require very high energy regeneration processes.^{107,108}

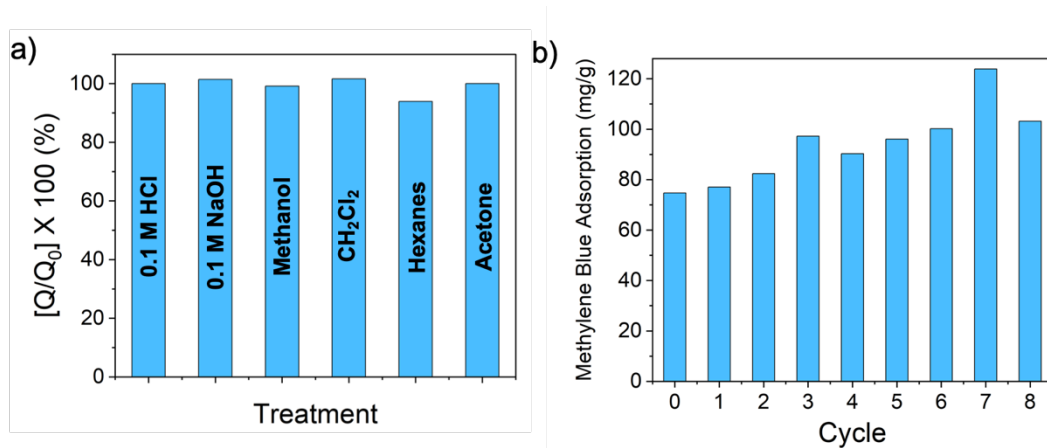


Figure 2.5. (a) Adsorption performance of β -CD-PN to methylene blue after variable chemical treatments (Q = adsorption after treatment, Q_0 = baseline adsorption). (b) Recyclability of β -CD-PN methylene blue adsorption where cycle 0 is the first use.

2.5. Model Column Adsorption

The selective adsorption demonstrated by β -CD-PN, in conjunction with the scalability of the synthesis, suggest that it can be employed as a filler adsorbent for energy-efficient separation of organic molecules in aqueous solution. Furthermore, the crosslinked nature of β -CD-PN mitigates potential concerns related to sloughing and dissolution in column adsorption applications due to its inherent robustness.

Model flow-through separation experiments were conducted in a miniature column using a 1 mL syringe (**Figure 2.6a**). The model column contained approximately 100 mg of adsorbent. An aqueous feed solution containing a molecular dye was continuously fed through the column with a flow rate of ~ 0.4 mL/s, while the eluent was collected in fractions for analysis. As expected, β -CD-PN exhibits highly efficient adsorption with exemplary selectivity towards BPA and methylene blue (**Figure 2.6c**). For BPA, 99% adsorption efficiency was maintained for the full duration of the 60 mL feed solution (0.2 mM). While for methylene blue 99% adsorption efficiency was maintained for the first 32 mL of feed solution with over 90% adsorption efficiency continuing up to 53 mL of feed solution (0.2 mM). α -CD-PN, on the other hand, had minimal adsorption for molecules of all sizes due to its smaller cavity size (**Figure 2.6d**). Only BPA and rose Bengal exhibit marginal adsorption. The BPA adsorption can be attributed to hydrogen bonding interactions with BPA by the residual hydroxyl groups on α -CD-PN. The small amount of adsorption of the larger rose Bengal molecule is likely due to the partial inclusion of the iodide group into the α -cyclodextrin cavity.^{109,110} This result indicates that careful selection of the macrocycle based on cavity size is critical for achieving different levels of selectivity, which can be extended to various adsorbates.

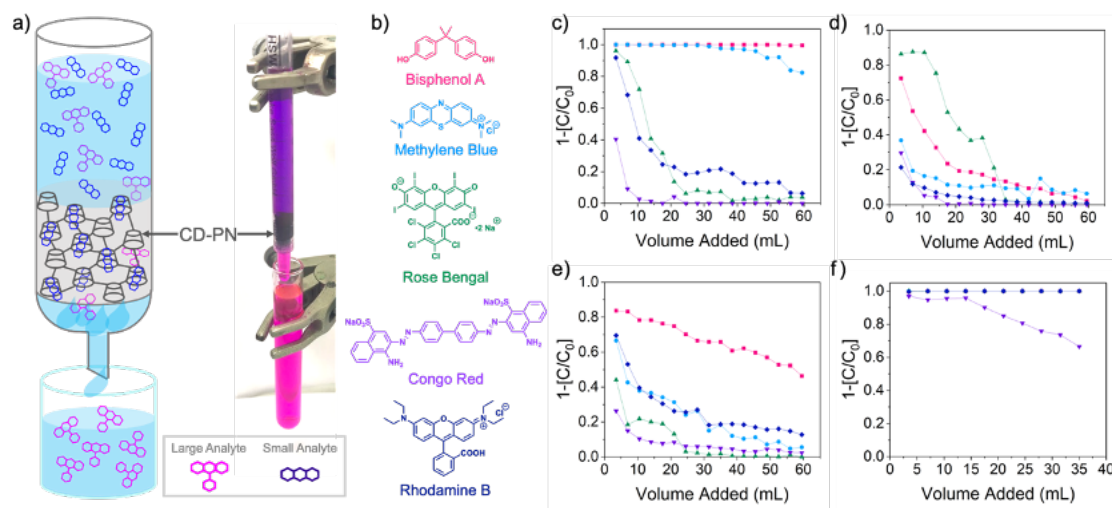


Figure 2.6. (a) Schematic representation and digital photograph of column separation using β -CD-PN as the adsorbent (flow rate ~ 0.4 mL/s); (b) structures of tested small molecular dyes; column dye adsorption data of (c) β -CD-PN (d) α -CD-PN (e) Glu-PN and (f) activated carbon ($C =$ eluent concentration, $C_0 =$ feed concentration). In Figure 6f, all dye adsorption data are overlapping except for Congo red.

To further confirm the important role of macrocyclic binding sites in engineering selective adsorption, the performance of two control materials, namely, commercial activated carbon and a crosslinked network of glucose (Glu-PN) without the presence of cyclodextrin-like macrocycles, were investigated and compared. Glu-PN was synthesized under the same MSA-mediated conditions using D-(+)-glucose as the starting material rendering a crosslinked network chemically similar to CD-PN but devoid of macrocyclic binding sites. Flow-through adsorption tests on Glu-PN showed almost no uptake of all tested molecules. Only a small uptake of BPA (**Figure 2.6e**) was observed likely due to hydrogen bonding, agreeing with that observed on α -CD-PN. In contrast, commercial

activated carbon exhibited vast adsorption uptake of all tested organic molecules without any selectivity (**Figure 2.6f**) as a result of the rich presence of pores with a broad size distribution. These adsorption data demonstrate that the macrocyclic backbone in β -CD-PN is essential for the observed adsorption selectivity and further confirm that the macrocyclic cavity is retained from the cyclodextrin monomers throughout the synthesis.

2.6. Molecular Separation

The extent of selectivity in column adsorption of β -CD-PN was further explored and confirmed by investigating the adsorption of small organic molecules in the presence of a high concentration of interfering non-adsorbing organic molecules. In this study, the adsorption of methylene blue (0.005 mM) was tested in the presence of an excess amount of rhodamine B (0.1 mM) (methylene blue: rhodamine B = 1:20), and the model column was run as described in **Section 2.5**. β -CD-PN exhibited complete adsorption of methylene blue while adsorbing little to no rhodamine B (**Figure 2.7a**). In comparison, α -CD-PN adsorbed a small amount of methylene blue and very little rhodamine B (**Figure 2.7b**). Glu-PN adsorbed a minimal amount of rhodamine B and no methylene blue (**Figure 2.7c**). Activated carbon, in contrast, displayed no selectivity by completely adsorbing both dyes (**Figure 2.7d**). These data further demonstrate the excellent size selectivity of β -CD-PN while also showing its strong affinity for molecules with size and shape complementarity even amongst a substantial amount of interference. It is important, however, to note that while selectivity is retained, the adsorption capacity is somewhat impacted potentially due

to intermolecular interactions between the dye molecules.¹¹¹ Additionally, it is expected that the adsorption properties can be enhanced with careful morphological control, which can be achieved through *in situ* crosslinking enabled by the pristine nature of the MSA mediated reaction.

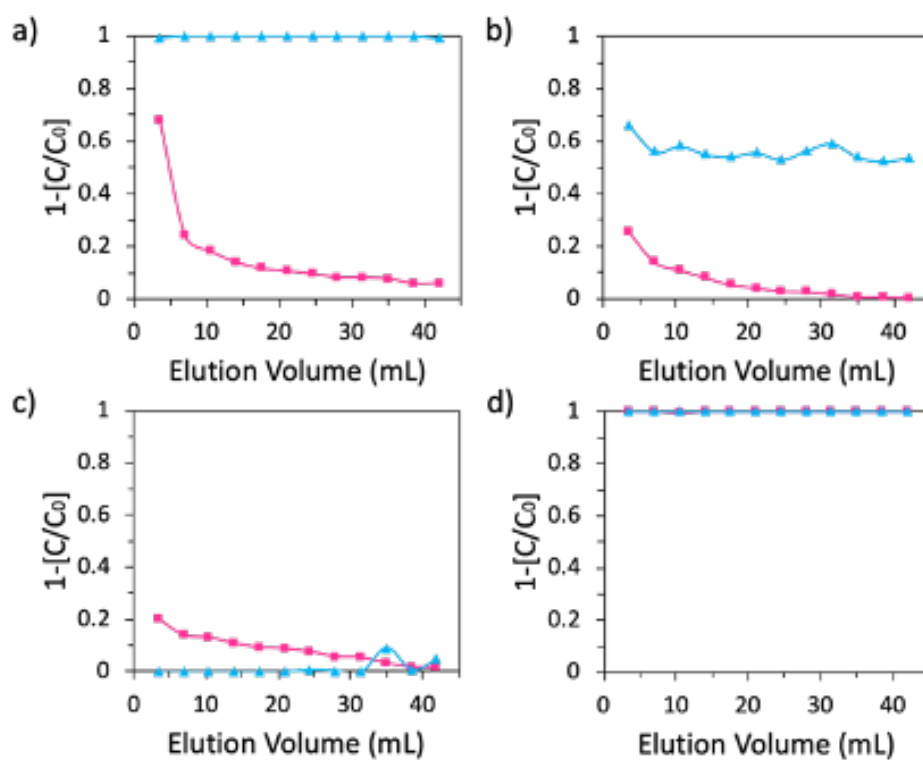


Figure 2.7. Adsorption performance of a mixture of 0.005 mM methylene blue (blue data points) + 0.1 mM rhodamine B (pink data points) by (a) β -CD-PN (b) α -CD-PN (c) Glu-PN and (d) activated carbon. In Figure 3d, the data points for methylene blue and rhodamine B are overlapping.

2.7. Conclusion

In conclusion, the sustainable and scalable synthesis of dehydrated cyclodextrin-derived polymer networks was achieved via a facile MSA-mediated condensation reaction. The retained macrocyclic cavities in β -CD-PN enable its exceptional selective adsorption of organic small molecules with complementary size and shape with the cyclodextrin cavity size, such as BPA and methylene blue, even in the presence of a highly concentrated interfering compound. To put this result in context, β -CD-PN was compared with other cyclodextrin-derived polymers in terms of BPA adsorption capacities and synthetic conditions (**Table 2.3**), demonstrating its high adsorption performance as a result of the linker-less synthetic strategy along with enhanced synthetic sustainability and scalability. Moreover, the crosslinked network imparts a high level of robustness into the materials with both thermal and chemical stability, as well as cyclability through a low energy-consuming regeneration process. The combined advantages of this class of CD-PNs promise their future application in fine chemicals/ pharmaceutical separation, sensing, and environmental remediation. Furthermore, it is expected that with careful morphological control, which is enabled by the simplistic synthesis, the CD-PNs present a powerful platform for advancing both fundamental knowledge and applications of cyclodextrin-based materials.

2.8. Experimental Details

2.8.1. General Methods

All starting materials and solvents were obtained from commercial suppliers and used without further purification. Activated charcoal was purchased from Sigma-Aldrich with a 100-mesh particle size for adsorption tests. X-ray photoelectron spectroscopy (XPS) data were obtained using an Omicron XPS/UPS system with Argus detector. Solid-state NMR spectra were obtained on a Bruker Avance 400 MHz spectrometer at magic angle spinning (MAS) rates of 10 kHz with 4 mm CP/MAS probes at room temperature. Fourier transform infrared (FTIR) Spectroscopy was recorded using a Shimadzu IRAffinity-1S spectrometer. UV-visible absorption spectra were recorded on a Shimadzu UV-2600 UV-Vis Spectrophotometer. Field-emission scanning electron microscopic (SEM) images were collected using a JEOL JSM-7500F FE-SEM at 5 kV. Samples were sputter coated in platinum/palladium prior to imaging. Thermogravimetric analysis (TGA) was carried out with a TA Q500 thermogravimetric analyzer at a heating rate of 20°C min⁻¹ from 30°C to 900°C under N₂ atmosphere. Elemental analysis was performed by Robertson Microlit Laboratories for elemental CHN analysis.

2.8.2. Synthetic Procedures

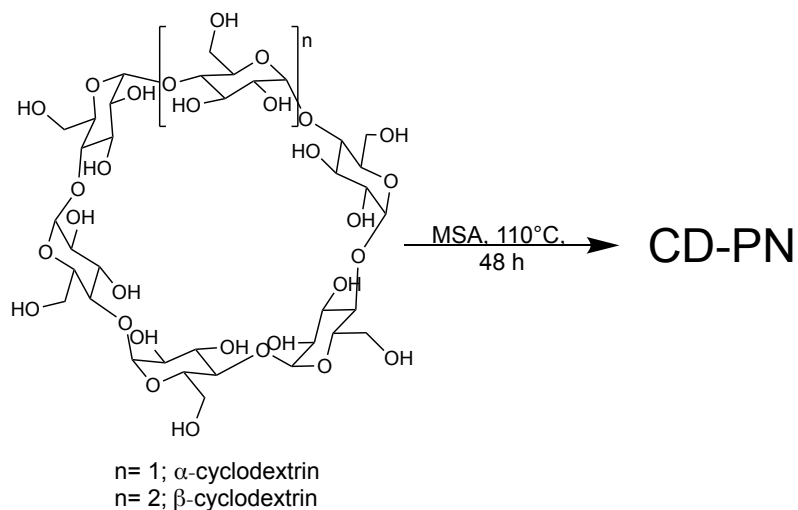


Figure 2.8. Synthesis of α - and β -CD-PN via MSA-mediated condensation.

α -CD-PN and β -CD-PN: Cyclodextrin, either α or β , (5.0 g, 5.1 mmol if α -CD or 15.0 g, 13.2 mmol if β -CD) was dissolved in MSA (150 mL) and pre-reacted for 45 minutes with bath sonication to form a dark red solution. The solution was then heated and maintained at 110°C for 48 h. Afterwards, the solution was cooled in an ice bath and quenched with water. The solid was collected and washed with copious amounts of water. Soxhlet extraction by water was then conducted for 24 h to remove uncross-linked low molecular weight material. Subsequently, the solid was dried in a vacuum oven at 80°C for 24 h. The dried solid, **α -CD-PN (3.4 g, 68 % yield)** and **β -CD-PN (9.6 g, 64 % yield)**

was then ground into a fine powder with a coffee grinder for further characterization and performance tests.

Percent yield based on cyclodextrin monomer mass is defined by *Equation 2.1*. The number of moles of water lost during the reaction can be estimated from the percent yield based on the assumption that all weight loss is due to water loss. Using this method, it is estimated that 22.69 mol of H₂O are lost per mole of β-cyclodextrin monomer and 17.43 mol of H₂O are lost per mole of α-cyclodextrin monomer.

$$\% \text{ yield} = \left(\frac{\text{mass of isolated CD-PN}}{\text{mass of CD monomer}} \times 100 \right) \quad (\text{Equation 2.1})$$

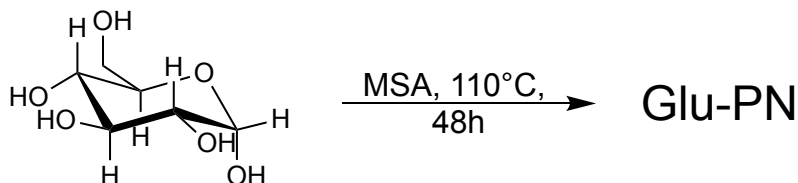


Figure 2.9. Synthesis of Glu-PN via MSA-mediated condensation.

Glucose-Derived Polymer Network (Glu-PN): d-(+)-Glucose (5.0 g, 27.7 mmol) was dissolved in MSA (50 mL) and pre-reacted for 45 minutes under bath sonication. The solution was then heated and maintained at 110°C for 48 h. Afterwards, the solution was cooled in an ice bath and quenched with water. The solid was collected and washed with copious amounts of water. Soxhlet extraction by water was then conducted for 24 h to remove uncross-linked low molecular weight material. Subsequently, the solid was dried

in a vacuum oven at 80°C for 24 h. The dried solid, **Glu-PN (4.3 g, 86 % yield)** was then ground into a fine powder with a coffee grinder for further characterization and performance tests.

2.8.3. X-Ray Photoelectron Spectroscopy

To monitor how the reaction temperature impacts the level of dehydration in the product, three batches of β -CD-PN were synthesized with the reaction temperature varied at 50°C, 80°C, and 110°C. XPS was used to analyze the nature of carbon in the material. The shift of the C1s C—C peak towards 284 eV corresponding to sp^2 carbon indicated that dehydration via acid-mediated elimination occurred along with cross-linking during the reaction. The content of sp^2 carbon increased as the temperature was elevated as evidenced by a consistent shift of the C1s C—C peak towards 284 eV (**Figure 2.11 and Table 2.1**).

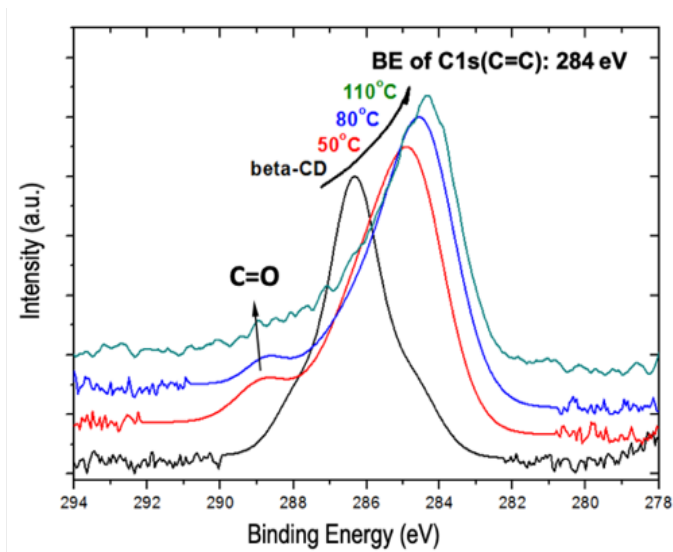


Figure 2.10. Correlation between the reaction temperature and C1s XPS peak of β -cyclodextrin (beta-CD) and β -CD-PN prepared under varying temperatures (50-110°C).

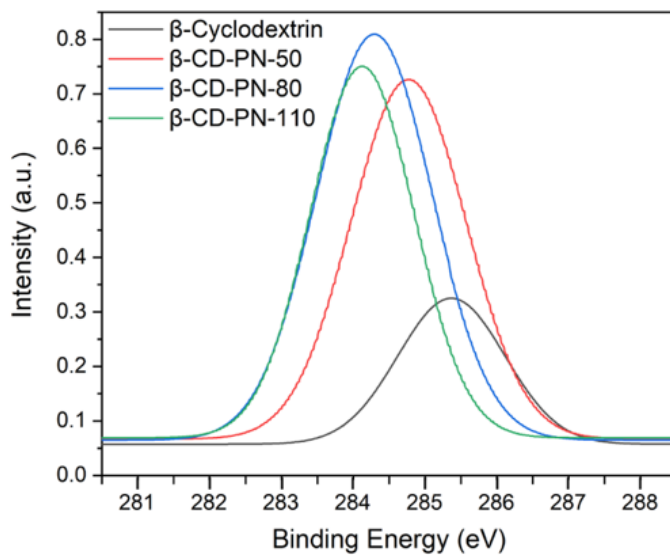


Figure 2.11. XPS C1s C—C deconvoluted peaks of β -cyclodextrin and β -CD-PN prepared under varying temperatures.

Table 2.1. Table of XPS C1s peak positions and areas for β -CD and β -CD-PN prepared under varying temperatures.

	β -Cyclodextrin		β -CD-PN 50°C		β -CD-PN 80°C		β -CD-PN 110°C	
Peak	Position	Peak Area	Position	Peak Area	Position	Peak Area	Position	Peak Area
C—C	284.7	17.92	284.6	48.00	284.4	58.30	284.1	49.30
C—O	286.3	68.89	285.9	44.18	285.7	38.10	285.5	39.50
C=O	287.9	12.19	288.9	7.83	288.8	3.60	288.1	11.20

2.8.4. Solid-State NMR

Solid-state ^{13}C CP/MAS NMR of β -CD-PN and β -cyclodextrin were measured at room temperature in the powder form. In the β -CD-PN spectrum, the emergence of peaks ranging from $\sim 180 - 215$ ppm indicate the presence of carbonyls within the polymer, which is not observed in β -cyclodextrin (**Figure 2.12**). Additionally, a peak around 155 ppm indicates the presence of alkene sp^2 carbons in β -CD-PN as observed in XPS (**Figure 2.11**).

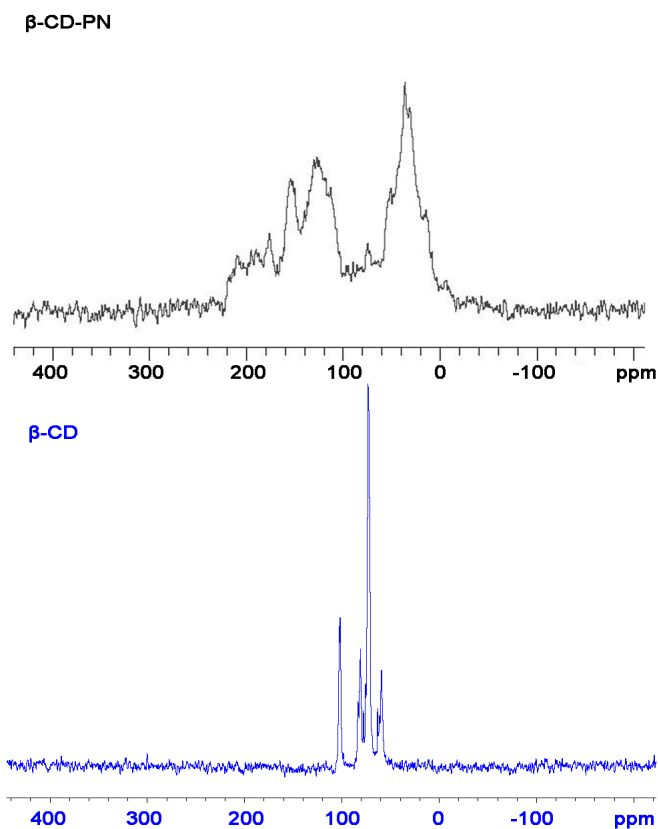


Figure 2.12. Solid-state CP/MAS ^{13}C NMR spectra of β -CD-PN and β -cyclodextrin (β -CD).

2.8.5. Fourier Transform Infrared Spectroscopy

A table of FTIR peak assignments is shown below for β -CD-PN and β -cyclodextrin. The emergence of peaks indicative of sp^2 carbons are consistent with the dehydration observed from NMR and XPS (**Figures 2.11 and 2.12**). Additionally, the FTIR spectra of β -CD-PN and β -CD-PN-Film are compared in **Figure 2.13** demonstrating that the structure and functional groups of the bulk powder material and the thin film are the same.

Table 2.2. FTIR peak assignments of β -CD-PN and β -cyclodextrin.

	β -CD-PN	β -Cyclodextrin
Functional Group	Absorption (cm^{-1})	Absorption (cm^{-1})
<u>C-O-H</u>	1039	1024
<u>C-O-C</u>	1157	1151
<u>C=C</u>	1658	—
<u>C=O</u>	1710	—
<u>C=C-H</u>	3101	—
<u>O-H</u>	3400	3336

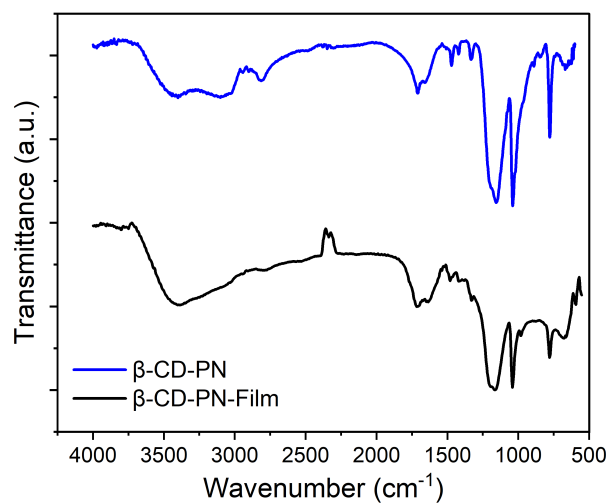


Figure 2.13. FTIR spectra comparison of β -CD-PN and β -CD-PN-Film.

2.8.6. Elemental Analysis Calculation

The extent of dehydration was estimated based on elemental analysis data from β -CD-PN and β -cyclodextrin. The empirical formula of β -CD-PN was determined based on the elemental analysis results, while the degree of dehydration was estimated based on the assumption of no carbon loss during the reaction. Using the respective empirical formulas, the amount of hydrogen and oxygen lost was determined and listed in **Equation 2.2**.



The extent of hydrogen and oxygen lost was averaged to give an estimation of ~ 2.78 moles of water lost per glucopyranosidic unit, *i.e.*, ~ 19.46 moles of water lost per mole of β -cyclodextrin.

2.8.7. CD-PN Film Fabrication

α -/ β -CD-PN-film: Cyclodextrin, either α - or β -, (2.1 mmol if α -CD or 0.2 g, 1.8 mmol if β -CD) was dissolved in MSA (2 mL) and pre-reacted for 30 min with bath sonication, forming a dark red solution. The solution was then heated for 3 h at 110°C. (Note: the reaction time should be tailored according to the volume of the reaction solution, in order to obtain a viscous yet fluid solution for casting.) After the appropriate reaction time, the solution is cooled and cast onto a glass substrate using a glass pipet. Bubbles should be removed if possible. Two pieces of micro cover glass divider with a thickness between 0.12-0.17mm are placed on either side of the substrate (**Figure 2.14**). Then another piece of glass is slowly placed on top. The sandwiched system was further heated at 110°C for

48 h. Afterwards, the glass on top was carefully removed leaving the film on the bottom glass substrate. The film was subsequently washed with copious amounts of water.

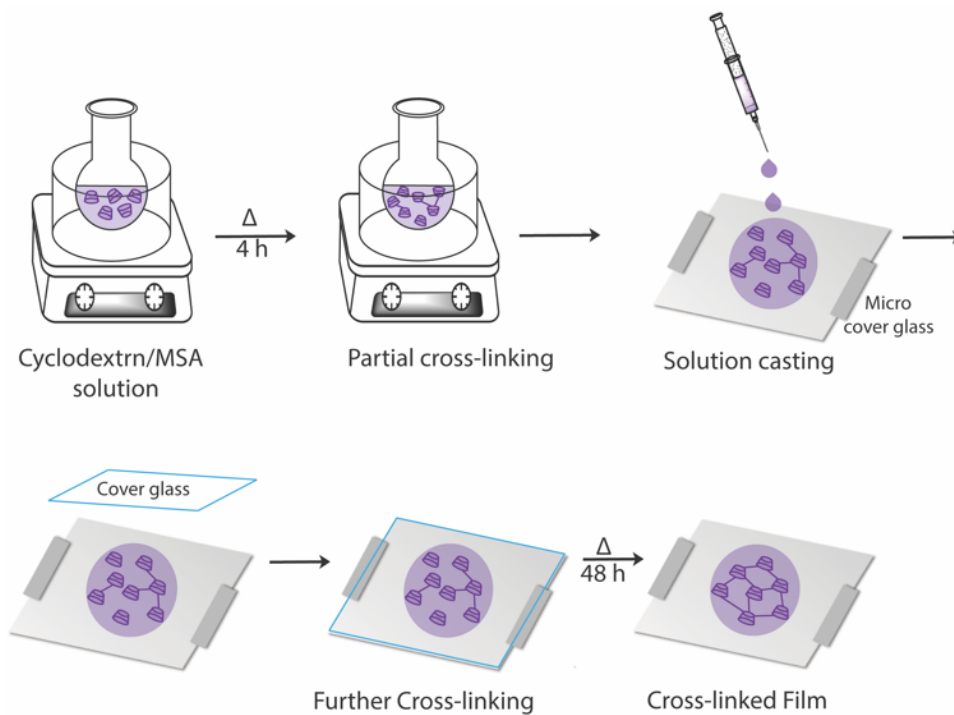


Figure 2.14. CD-PN film fabrication method.

2.8.8. Scanning Electron Microscopy

SEM samples were coated with 3 nm of platinum/palladium, 80% and 20%, respectively, using a Cressington Sputter Coater 208 HR for high resolution FE-SEM coating to make the samples conductive. SEM images of the β -CD-PN sample powderized by a commercial coffee grinder and the thin films as described in **Section 2.8.7.** were recorded.

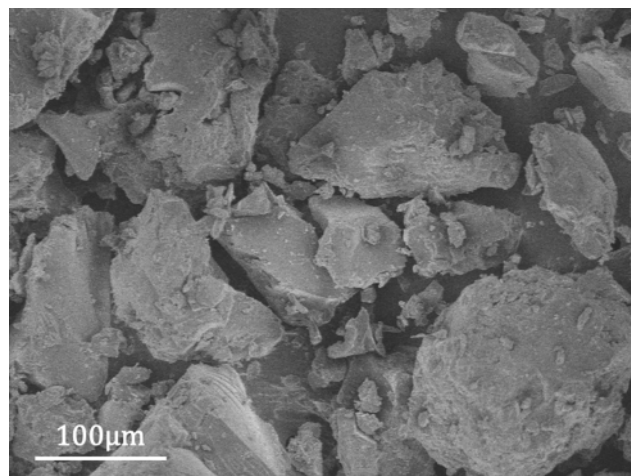


Figure 2.15. SEM image of β -CD-PN sample powderized by a commercial coffee grinder.

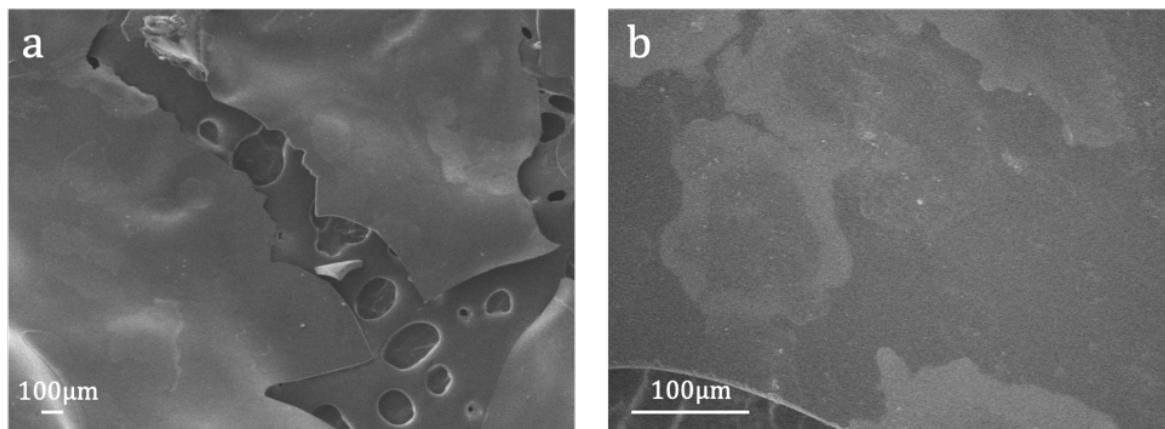


Figure 2.16. The top view SEM images of β -CD-PN film.

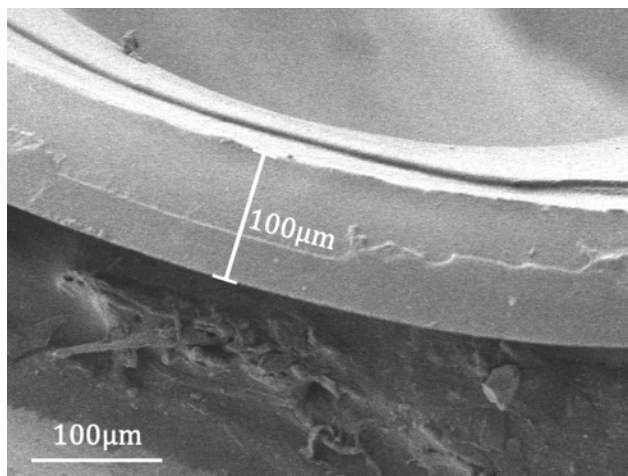


Figure 2.17. The cross-section view SEM image of β -CD-PN film.

2.8.9. Structure Size Modeling

The molecular structures of the dyes were modeled using ChemDraw3D. The molecule sizes were measured on ChemDraw3D between particular atoms within the molecule to give a general idea of the molecular dimensions. These measurements were validated by comparing some of these data with single crystal structures from Cambridge Crystallographic Data Centre analyzed with Mercury crystallography analysis software, which showed percent difference between 0.4~8.5%.

2.8.10. Adsorption Performance

2.8.10.1. Adsorption Rate

Powder of β -CD-PN (12 mg) was added into an aqueous solution of organic compounds (12 mL, 0.1 mM). As the solution was stirred, 2 mL aliquots were removed at the time intervals of 10 seconds, 30 seconds, 1 minute, 2 minutes, 5 minutes, and 10

minutes, respectively. The aliquots were passed through a syringe filter to remove the solid CD-PN. The adsorption efficiency was determined by comparing the UV-vis absorbance of these sample with that of the initial solution (**Equation 2.3**), where C = sample concentration and C_0 = initial concentration. The organic compounds tested were methylene blue, bisphenol A, rose Bengal, rhodamine B, and Congo red. The β -CD-PN demonstrated fast and selective adsorption of smaller organic molecules, *i.e.*, methylene blue and bisphenol A, within 10 minutes. Adsorption efficiencies of all the other larger organic molecules were lower than 10% after 10 minutes.

$$\text{Adsorption Efficiency (\%)} = \left(1 - \frac{C}{C_0}\right) \times 100 \quad (\text{Equation 2.3})$$

2.8.10.2. β -CD-PN Film Solution Adsorption

β -CD-PN film pieces (15 mg) were added into an aqueous solution of organic compounds (15 mL, 0.1 mM). The solution was stirred for 30 minutes, and then a sample was passed through a syringe filter to remove any small pieces of film that broke off during the stirring. The removal efficiency of the β -CD-PN film was determined as described in **Section 2.8.10.1**. The organic compounds tested were methylene blue, bisphenol A, rose Bengal, rhodamine B, and Congo red. The selectivity is maintained in the film with bisphenol A and methylene blue being adsorbed, while larger molecules are adsorbed to a much lesser extent. Although the selectivity is still observed, the larger dye molecules were adsorbed more so to the film than was observed for the bulk powder (**Figure 2.18**). It is believed that this is a result of physical adsorption to the film surface rather than into the pores derived from β -cyclodextrin.

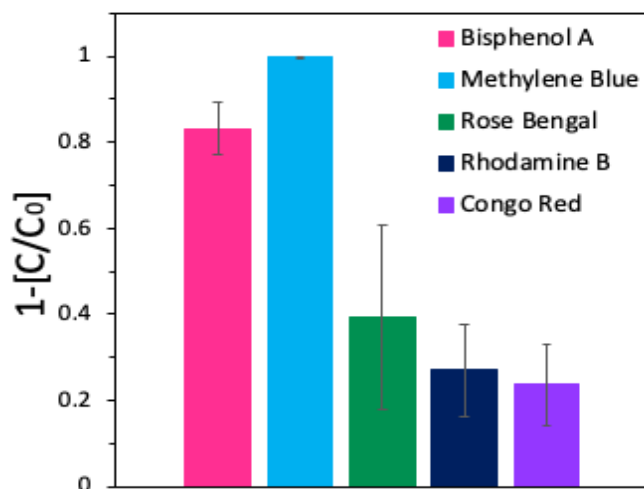


Figure 2.18. Adsorption efficiency of different organic molecules by β -CD-PN. The adsorption efficiency is an average of 4 trials.

2.8.10.3. Adsorption Isotherm

The adsorption isotherms were obtained by adding β -CD-PN (15 mg) to either a methylene blue or bisphenol A solution in water (20 mL) and stirring for 24 h. UV-visible absorption spectra of the solution were recorded to monitor concentration before and after adsorption. The initial concentrations of the solutions were varied from 0.05 to 2.0 mM. The adsorption isotherms were fitted using the Langmuir-Freundlich adsorption isotherm (*Equation 2.4*), where Q_e (mg/g) is the amount of dye adsorbed at equilibrium, C_e (mg/g) is the equilibrium solute concentration, Q_{max} (mg/g) is the maximum adsorption capacity, b is the Langmuir equilibrium constant, and n is the Freundlich heterogeneity index.¹¹² The Langmuir-Freundlich isotherm was chosen to characterize the isotherms because it is applicable to both homogeneous and heterogeneous materials, while also describing the

adsorption capacity. The CD-PN materials are expected to have a certain level of heterogeneity due to the myriad of reactions that can occur during synthesis (*e.g.*, ring-opening, β -elimination) leading the Langmuir-Freundlich isotherm to be a better fit than the Langmuir isotherm.

$$Q_e = \frac{Q_{max}bC_e^{1-n}}{1+bC_e^{1-n}} \quad (\text{Equation 2.4})$$

2.8.10.4. Column Adsorption

An adsorption column was prepared in a syringe (1 mL) by placing a small piece of cotton at the bottom, followed by adding ~ 100 mg of α - β -CD-PN, Glu-PN, or activated carbon as the stationary phase. An aqueous dye solution (0.2 mM) was then prepared. The solution was passed through the column driven by pressurized air with a flow rate of approximately ~ 0.4 mL/s and an empty bed contact time of approximately ~ 0.5 seconds. The eluent was collected as fractionated samples (3.5 mL each). The dye concentration in each eluent sample was determined using UV-visible absorption spectroscopy. The amount of dye adsorbed was then calculated based on the concentration difference between the stock solution and eluent. The samples for methylene blue, Congo red, and rose Bengal were diluted before the absorbance measurement in order to fulfill the Beer-Lambert law.

2.8.10.5. Column Adsorption with Interference

A column was prepared as described above using β -CD-PN. A mixed rhodamine B and methylene blue solution in water was prepared (0.1 mM rhodamine B + 0.005 mM methylene blue). The mixed solution was passed through the columns as described in

Section 2.8.10.4. The eluent was collected and measured with UV-visible absorption spectroscopy.

2.8.10.6. Recyclability

β -CD-PN (20 mg), either virgin or recycled, was stirred in a solution of methylene blue (20 mL, 0.1 mM) for 1 h. The amount of adsorbed methylene blue was determined by comparing the UV-Visible absorbance spectra of the solution before and after β -CD-PN treatment. After each test, the β -CD-PN was stirred in 30 mL of methanol at 35°C for 2 h to cleanse the adsorbed methylene blue, and subsequently collected via centrifugation, followed by washing and drying. The recycled sample was then dried under vacuum before use in the next cycle.

2.8.10.7. Solvent Resistance

β -CD-PN (100 mg) was suspended and stirred in each of the following solvents/solutions for 1 week: 0.1 M HCl, 0.1 M NaOH, Methanol, dichloromethane, hexanes, or acetone. Afterwards, the suspended solid was collected by centrifugation, washed, and dried under vacuum. Materials soaked in HCl or NaOH solutions were washed thoroughly with water before drying. After drying, the treated β -CD-PN (12 mg) was added into a methylene blue solution (12 mL, 0.1 mM) and stirred for 24 h. The methylene blue adsorption amount was then measured by UV-visible absorbance before and after the treatment.

2.8.11. Cyclodextrin-Based Polymer Comparison

The structure, synthetic conditions, and BPA adsorption capacity are compared for a series of cyclodextrin-based polymers. The prime difference between the β -CD-PN polymer reported in this work and other cyclodextrin-based polymers is that it is linker-less, meaning the cyclodextrin is directly crosslinked with no additional crosslinker. Additionally, the synthetic conditions are considerably greener than many of the other cyclodextrin-based polymers. The BPA adsorption capacity of β -CD-PN is significantly higher than other cyclodextrin-based polymers. This comparison supports the theory that the linker-less CD-PN polymer has the potential for an enhanced binding site density, which enables it with a high adsorption capacity from cyclodextrin itself. Although this parameter gives a general idea of adsorption performance, it is prudent to mention that varying techniques and measurement methods could cause some discrepancy between the reported values.

Table 2.3. Comparison of crosslinked cyclodextrin-based polymers.

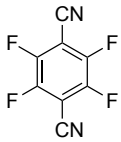
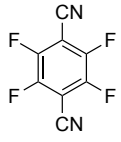
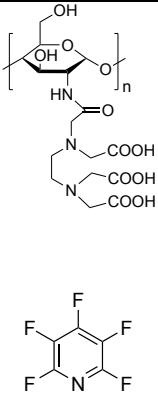
Polymer	Monomer	Crosslinker	Conditions	CD Functional-ization	BPA Q_{max} (mg/g)	Reference
CD-PN	β -CD	N/A	MSA, 110°C, 48 h	Dehydrated	388	This Work 102
P-CDP	β -CD		K_2CO_3 , THF, 80 °C, 48 h	N/A	88	12
TFN- CDP-2	β -CD		K_2CO_3 , DMSO, 80 °C, 18 h	Phenolated	250	50
P-CDEC	β -CD		8:1 MeTHF: H ₂ O, K_2CO_3 , 80 °C, 48 h	N/A	59-66*	113

Table 2.3. Continued.

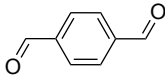
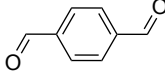
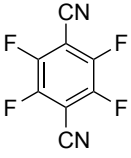
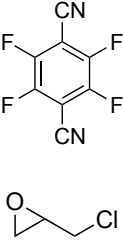
Polymer	Monomer	Crosslinker	Conditions	CD Functional-ization	BPA Q_{max} (mg/g)	Reference
β -CD COF	heptakis(6-amino-6-deoxy)- β -CD		50:50 EtOH:H ₂ O, AcOH, r.t., 48 h	Aminated	20	114
β -CD NCP	heptakis(6-amino-6-deoxy)- β -CD		50:50 EtOH:H ₂ O, Ammonia, r.t., 48 h	Aminated	10	114
P-CD-P5A-P	β -CD, Pillar[5]arene		K ₂ CO ₃ , THF, 80 °C, 72 h	N/A	258	54
T-E-CDP	β -CD		NaOH _(aq) , 90 °C, 3 h	N/A	128*	52

Table 2.3. Continued.

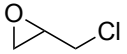
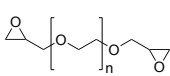
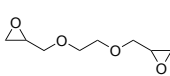
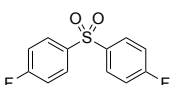
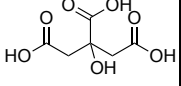
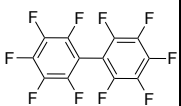
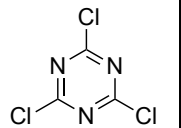
Polymer	Monomer	Crosslinker	Conditions	CD Functional-ization	BPA Q_{max} (mg/g)	Reference
ECP	β -CD		NaOH _(aq)	N/A	84	115
PEGCDP	β -CD		NaOH _(aq) , 60°C, 5 h	N/A	71	116
EGCDP	β -CD		NaOH _(aq) , 60°C, 5 h	N/A	78	116
β -CDP	β -CD		Toluene, DMAc, K ₂ CO ₃ , 150°C, 12 h	N/A	113	117

Table 2.3. Continued.

Polymer	Monomer	Crosslinker	Conditions	CD Functional-ization	BPA Q_{max} (mg/g)	Reference
CD-CA-g-PDMAEMA	β -CD, 2-dimethylamino ethyl methacrylate (DMAEMA)		1) KH_2PO_4 , 140°C, 3 h 2) $\text{K}_2\text{S}_2\text{O}_8$, 80°C, 30 min 3) 1 M HCl 4) DMAEMA, 80°C, 3 h	N/A	79	118
MP-CDP (DFP-CDP) ¹¹⁹	β -CD		K_2CO_3 , 1:3 THF:DMF, 85 °C, 72 h	N/A	79	120
CDW7-Triazine	β -CD		NaOH, BDMHAC, CH_3CN , H_2O	N/A	57	121

3. CYCLODEXTRIN-DERIVED POLYMER NANOPARTICLES*

3.1. Introduction

Although the bulk β -CD-PN solid displayed highly promising adsorption properties, the lack of processibility limits its further application into functional devices.¹⁰² This issue encountered with β -CD-PN is a common occurrence with crosslinked polymer materials as they are not soluble in most solvents and are not meltable. Two main strategies have been employed to process crosslinked materials into a practical material for applications. One is to attach the crosslinked polymer to a larger architecture that can either be processed itself or is already in the appropriate form for the desired application. This strategy has been utilized to process P-CDP for specific applications. In one example, P-CDP was functionalized onto cotton fabric which demonstrated improved adsorption of both organic micropollutants in solution and volatile organic compounds (VOC) in air.⁷³ Although not demonstrated, the functionalized fabric could feasibly be further processed into products with VOC capturing capabilities. P-CDP has also been polymerized onto microcrystalline cellulose for packing a column that can be applied in the continuous adsorption of micropollutants.¹²² The initial morphology of microcrystalline cellulose can be controlled, which is extended to the P-CDP coated microcrystalline cellulose, enabling column packing that was not possible with the bulk morphology of pure P-CDP. Using

*Protected under provisional patent “Fang, L.; Phillips, B.; Banerjee, S.; Al-Hashimi, M.; Handy, J.; Kalin, A. Cyclodextrin-derived Polymer Nanoparticles for Adsorption. Provisional Patent, April 9, 2021.”

this type of coating technique, a variety of morphologies can be obtained for crosslinked materials as long as an appropriate support is selected.

The other strategy to process crosslinked materials for practical applications is *in situ* crosslinking. Various potential morphologies can be obtained through this method. These include but are not limited to fibers, thin films, membranes, and nanoparticles. However, conditions required to achieve these morphologies can vary greatly between polymers. To obtain crosslinked fibers, electrospinning featuring *in situ* crosslinking can be utilized, although only a limited selection of crosslinking mechanisms are feasible for the electrospinning process.^{123,124} Solution processing followed by *in situ* crosslinking can be carried out in a confined space to obtain crosslinked polymer membranes, as demonstrated by Guo et al.⁹⁶ Finally, polymer nanoparticles can be developed by applying emulsion polymerization/crosslinking techniques, although considerable formulation is required to achieve nanoparticles with controlled morphologies.^{125,126}

Solution processing followed by *in situ* crosslinking was favored for processing β -CD-PN to avoid adding a potentially interfering support and enhance the favorable adsorption properties. Initially, thin film formation followed by *in situ* crosslinking was investigated.¹⁰² As described in **Section 2.8.7.**, β -CD-PN thin films could be successfully fabricated using a methodology developed by the Fang group.⁹⁶ The size selective adsorption observed in the bulk β -CD-PN was maintained in the thin films.¹⁰² Despite this promising attribute, the thin films are not exceptionally practical for real-world

incorporation into devices due to their brittleness, the harsh conditions required to form the thin films via *in situ* crosslinking, and the macroscopically dense nature of the film that hampers accessibility of the molecular adsorption sites. Expanding on the idea of implementing morphological control to improve processibility and binding site accessibility without the addition of outside supports, nanoparticle synthesis via emulsion polymerization was considered to be ideal.

3.1.1. Polymer Nanoparticles

The study and development of nanomaterials has been a continuously hot topic due to the drastic influence that size has on the physiochemical properties of a material.¹²⁷ Nanomaterials are known to possess enhanced surface areas compared to their bulk counterparts along with large surface to volume ratios.¹²⁸ These properties endow nanomaterials with unique performance potential in an array of applications. Specifically, polymer nanoparticles have been well explored and applied in a variety of fields, such as electronics, sensors, medicine, and environmental technology.¹²⁹ One major advantage of polymer nanoparticles is that their structures are highly versatile to afford high tunability of their properties towards specific applications.¹²⁷ Additionally, polymer nanoparticles are readily dispersed in appropriate solvents and therefore solution processible. Finally, as with other nanomaterials, polymer nanoparticles tend to demonstrate enhanced properties compared with their bulk polymer counterparts due to their higher surface areas and better accessibility of the functional sites within the material.¹³⁰ With the potential for solution

processibility, enhanced surface area, and improved surface-to-volume ratios, the synthesis of β -CD-PN-based nanoparticles was explored.

Polymer nanoparticle synthesis can be broken into two subcategories. The first category uses preformed polymers and shapes them into nanoparticles using methods such as salting out, solvent evaporation, or super critical fluid technology.¹²⁹ The second category relies on *in situ* polymerization as the nanoparticle is formed in a confined area. A variety of techniques, such as classic emulsion, mini-emulsion, micro-emulsion, and interfacial polymerization, can be used to directly polymerize monomers into polymer nanoparticles. The properties of the polymer nanoparticles can be strictly controlled with careful selection of the monomers and emulsion/polymerization conditions.¹²⁶ Building in properties, such as porosity or specific binding sites, enables the application of polymer nanoparticles in pollutant adsorption, gas sensing, chemical sensing, drug delivery, and other adsorption-based fields.¹²⁷

Molecular imprinting is often utilized to build selective binding sites into polymer nanoparticles. In this technique, a monomer or prepolymer is polymerized in the presence of a template molecule that is removed after polymerization enabling highly selective and sensitive binding at the imprinted sites.¹³¹ Molecularly imprinted polymer nanoparticles (MIPNP) extend this technique by employing morphological control to further improve the binding properties and incorporate selective binding into polymer nanoparticles.¹³⁰ The small size, large surface area, and high surface-to-volume ratio of polymer

nanoparticles enable more efficient analyte binding due to the greater accessibility of binding sites in MIPNPs compared with bulk materials. It was envisioned that a nanoparticle morphology could also enable greater accessibility of the binding sites in β -CD-PN. With this in mind, the nanoparticle morphology is expected to enhance the adsorption capacity, selectivity, and overall processibility of β -CD-PN.

3.1.2. Nanoparticle Emulsion Polymerization

Nanoparticle synthesis via emulsion polymerization relies on the formation of nanoscale micelles where polymerization can take place. Micelle formation is driven by hydrophobic effects and stabilized by surfactants, which decrease the interfacial tension between the oil and water phases.² Although micelle assembly is thermodynamically driven, most emulsion systems are kinetically stable rather than thermodynamically stable.¹³² This thermodynamic instability holds true for both classic emulsions and mini-emulsions, corresponding to particle diameters of < 1000 nm and < 100 nm, respectively.^{133,134} Microemulsions, which have particle diameters < 10 nm, are the exception to this rule and are thermodynamically stable dispersions. These distinctions in particle size are used to classify emulsions, however, they can be further classified based on the continuous and dispersed phases. Oil-in-water (o/w) emulsions are the most common and classic examples of emulsions in which a hydrophobic oil is dispersed in an aqueous solution. Water-in-oil (w/o) emulsions are known as inverse-emulsions because they are composed of an aqueous phase dispersed in an oil phase. Non-aqueous emulsions,

known as oil-in-oil (o/o), are also possible, where neither the continuous nor dispersed phases are aqueous based.

Controlling the interfacial tension between phases is critical to emulsification and the subsequent stability of the emulsion. Surfactants are used to mediate the interfacial tension of the system and surfactant selection greatly effects the properties of an emulsion. It is important to note, however, that the selection of the two phases is also important because the interfacial tension between the two needs to be within a range that can be reasonably modified by surfactants. Beyond reducing the interfacial tension of the system, surfactants also determine the type of the supramolecular assemblies formed within an emulsion. The relationship between surfactant molecular structure and micelle shape has been well defined by the molecular packing parameter (critical packing parameter, C_{PP}).¹³⁵ The value of the critical packing parameter is described by **Equation 3.1**, where V_0 is the volume occupied by the hydrophobic chains of the surfactant, A_{mic} is the surface area of the hydrophilic head group, and l_c is the critical chain length of the surfactant tail. C_{PP} values, their respective surfactant shapes, and the micellular shapes they form are shown in **Figure 3.1**.

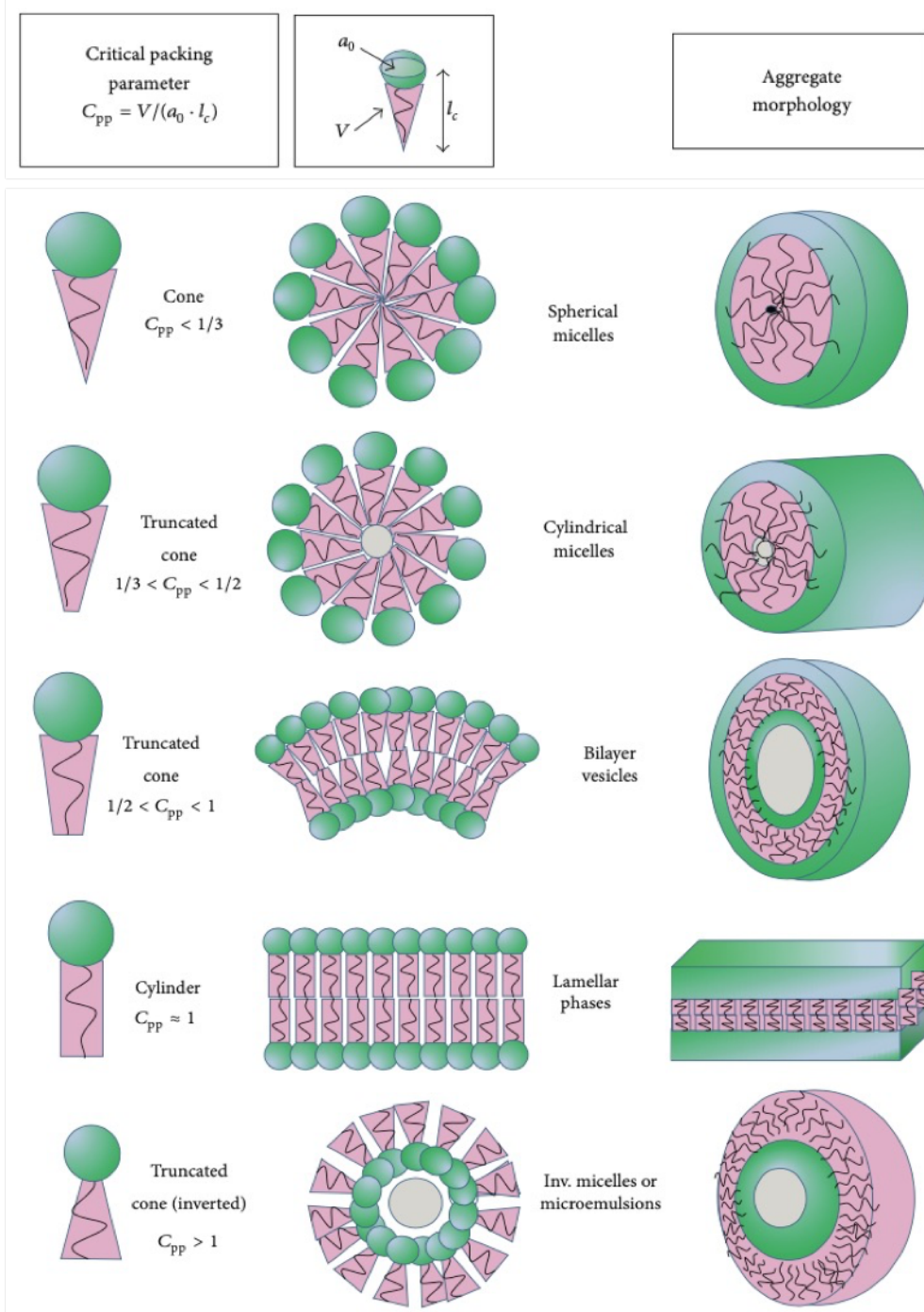


Figure 3.1. Amphiphile shape factors and summary of the aggregate structures that can be predicted from the critical packing parameter C_{pp} . Reprinted from [136].

The implementation of the critical packing parameter has enabled improved intuition based on surfactant structure towards predicting micellar shape. As shown in **Figure 3.1**, a cone shape or $C_{PP} < 1/3$ is required to form spherical micelles in a traditional oil-in-water (o/w) emulsion. However, an inverse truncated cone or $C_{PP} > 1$ is required to form inverted water-in-oil emulsion.¹³⁶ Strict control over polymer nanostructures formed during emulsion polymerization can be achieved with a thorough understanding of C_{PP} values and their subsequent micellar structures.

$$C_{PP} = \frac{V_0}{A_{mic}l_c} \quad (\text{Equation 3.1})$$

3.2. β -Cyclodextrin-Derived Polymer Nanoparticle Emulsion Polymerization

3.2.1. Emulsion Formulation

Non-aqueous inverse-emulsion polymerization was employed to prepare β -cyclodextrin-derived polymer nanoparticles (β -CD-PNP) (**Figure 3.2**). In designing the synthesis of β -CD-PNP, the simplest route was to directly emulsify the reaction solution used in the bulk β -CD-PN synthesis and employ *in situ* crosslinking to polymerize the cyclodextrin monomers into nanoparticles, as was demonstrated in the β -CD-PN thin film synthesis (**Section 2.8.7**). The synthetic conditions of β -CD-PN present two major challenges when it comes to its translation into emulsion polymerization. The first and main challenge lies in the use of MSA as the solvent. MSA is a strong, viscous organic

acid, which can be difficult to apply as a dispersed phase. The true challenge in emulsification of MSA, however, comes from its relatively high viscosity (11.26 mPas) compared with water (1.0 mPas).¹³⁷ The dispersion of viscous liquids in general is more difficult because the surface tension in viscous solutions is increased, which translates into increased interfacial tension that needs to be overcome to be emulsified. The second challenge stemming from the initial reaction conditions of β -CD-PN is the high reaction temperature required to induce efficient crosslinking. To accommodate this condition, higher boiling point solvents are needed for the continuous phase to maintain the integrity of the emulsion.

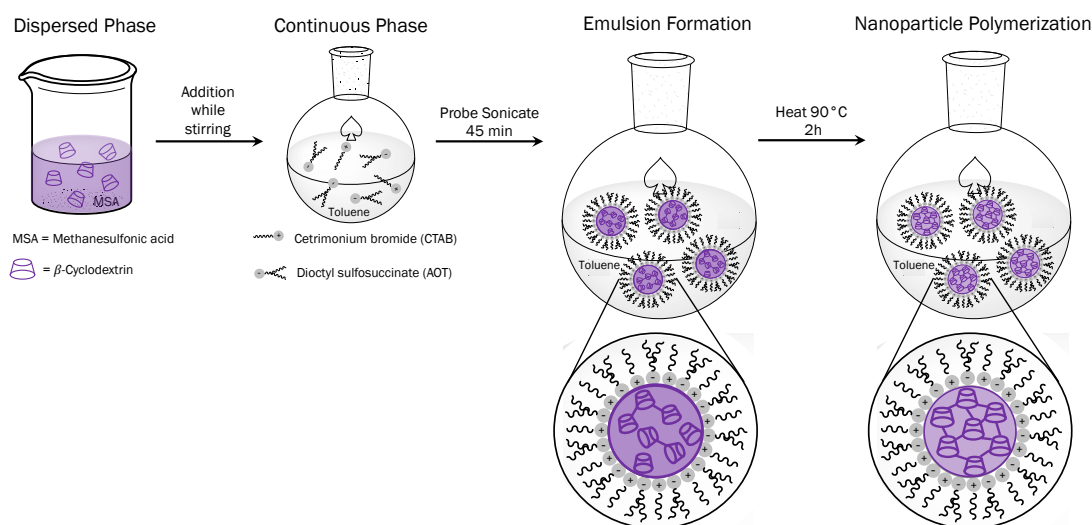


Figure 3.2. General formulation and reaction scheme towards the synthesis of β -CD-PNP.

The formulation design for the synthesis of β -CD-PNP mainly focused on tackling the interfacial tension challenge caused by the viscosity of the MSA solution, while keeping the required reaction temperature in mind. Two primary methods are commonly employed to reduce the high interfacial tension caused by a viscous dispersed phase: (i) reducing the viscosity and (ii) adding surfactants. The simplest method to reduce the viscosity of the reaction solution would be to dilute it, however, adding water into the reaction solution could hinder the efficiency of the crosslinking as water is a byproduct of the reaction. Because dilution was not feasible, the concentration of cyclodextrin in the reaction solution was reduced to lower the concentration of potential oligomer formed during the emulsification process; rather than a concentration of 0.1 mg/mL that was used in the bulk synthesis, the concentration of cyclodextrin was reduced to 0.05 mg/mL for nanoparticle synthesis. Further modification of the reaction solution itself was avoided in order to maintain the integrity of the crosslinked polymer nanoparticles.

To avoid further dispersed phase modification, careful design and selection of the continuous phase and surfactants was key to the successful synthesis of β -CD-PNP. High boiling point solvents were screened to accommodate the necessary β -CD-PN reaction temperature. The polarity of the solvent is also a critical characteristic of the continuous phase because of the effect it has on the interfacial tension of the emulsion. Establishing a balance between minimizing the interfacial tension while maintaining two separate phases was critical to formulating a stable emulsion. Despite their desired high boiling points, the

interfacial tension between long-chain alkane solvents, such as dodecane, and MSA was found to be too high to overcome with surfactants and form a stable emulsion. Toluene was investigated as the continuous phase to mediate the interfacial tension between the two phases. Although toluene is overall a non-polar solvent, its aromatic quadrupole nature causes it to be slightly more polar than long-chain alkanes whilst maintaining the necessary high boiling point. This enhanced polarity, along with surfactants, reduced the interfacial tension enough to allow for the emulsification of MSA.

Owing to the polar nature of MSA, an inverse-emulsion was required for the emulsion polymerization. Furthermore, a surfactant with a truncated cone shape was necessary to form the spherical micelles desired for nanoparticle synthesis (**Figure 3.1**). With this knowledge in mind, dioctyl sulfosuccinate sodium salt, AOT, was selected as the initial surfactant because its branched alkyl chain structure gives rise to the desired inverted truncated cone structure (**Figure 3.3a**).¹²⁹ Additionally, AOT is commercially available and inexpensive, which could be important for future scalability. Although an inverse emulsion could initially form, the emulsification of MSA in toluene with AOT alone was not stable, even over a short period of time, owing to the exceptionally high interfacial tension. To enhance the stability and further reduce the interfacial tension of the system, a cosurfactant was selected. Because of the anionic nature of AOT, a cationic cosurfactant was selected, which can enhance the emulsion stability through synergistic electrostatic interactions between the charged surfactant heads, as shown in **Figure**

3.3b.¹³⁸ The favorable electrostatic interactions stabilize micelle formation by decreasing the free energy of micelle formation.¹³⁹ Cetrimonium bromide, CTAB, was selected as the cationic cosurfactant due to its commercial availability (**Figure 3.3a**). Using the mixed surfactant system of AOT and CTAB, a stable emulsion of MSA in toluene was formulated for β -CD-PNP synthesis.

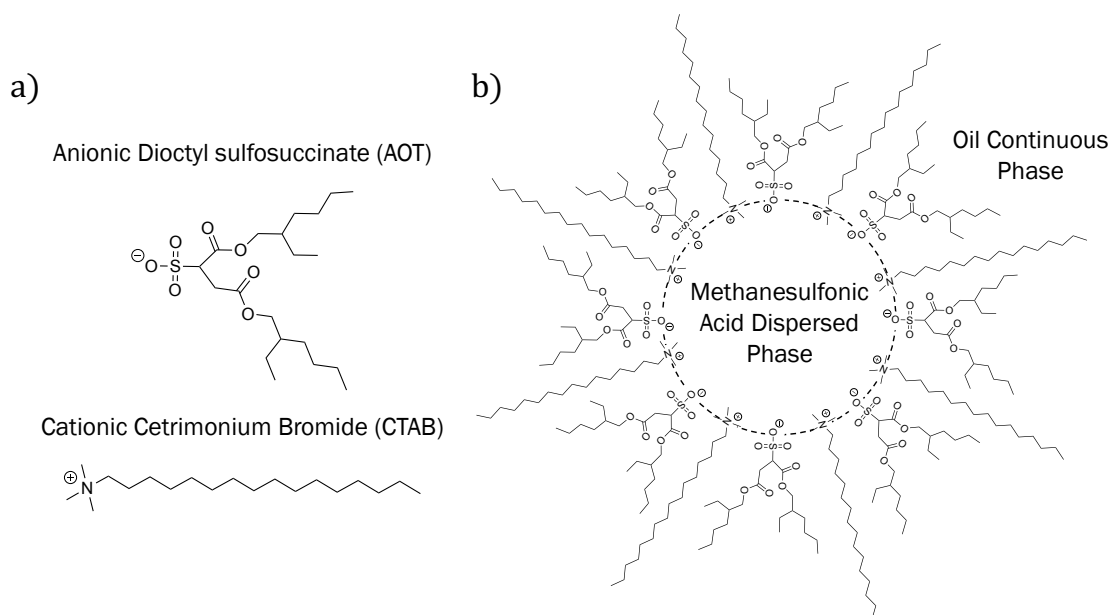


Figure 3.3. (a) Structures of AOT and CTAB surfactants; (b) General illustration of the synergistic interactions between the cationic and anionic cosurfactant system.

3.2.2. Polymerization Reaction Condition Screening

Screening of the reaction conditions was conducted to optimize micelle formation, yield, and nanoparticle size. During the initial component screening, a 40:1 ratio of the continuous phase to the dispersed phase by volume was used. Higher loading ratios of 20:1 and 10:1 (Toluene: MSA) were also investigated to minimize waste and maximize yield per volume. The emulsion itself was characterized using an optical microscope and the nanoparticles were imaged using SEM. No significant difference was detected for each of the ratios via optical microscope or SEM, so a ratio of 10:1 was employed moving forward (**Figure 3.4**).

The reaction time was also screened to optimize product yield while maintaining the nanoparticle morphology. Because reactions happen more efficiently at the nanoscale, the reaction time was significantly reduced compared to that of the bulk synthesis described in **Chapter 2**. It was observed that nanoparticles could form within 1 hour but after 3 hours reaction time, bulkier materials formed presumably due to coalescence.¹⁴⁰ The optimal reaction time was determined to be 2 hours based on both nanoparticle morphology and yield (**Table 3.1**).

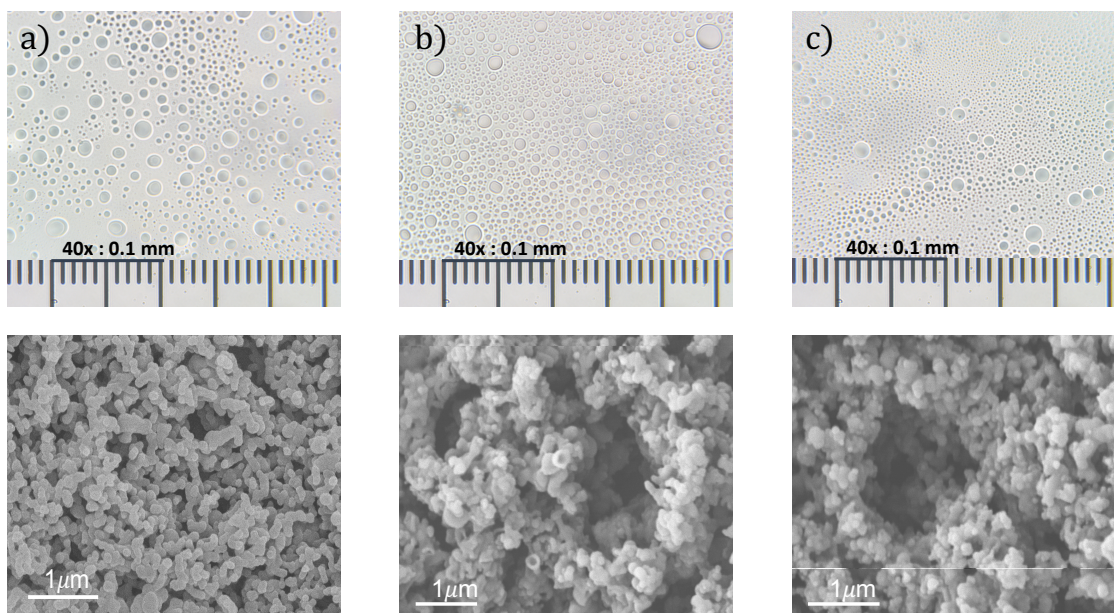
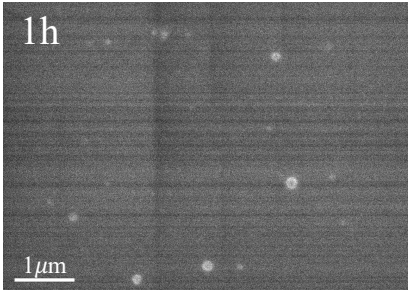
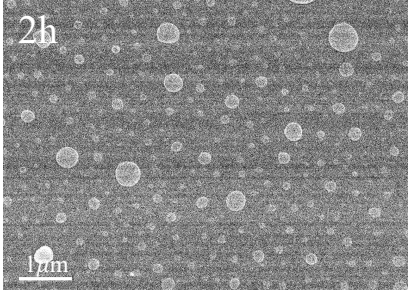
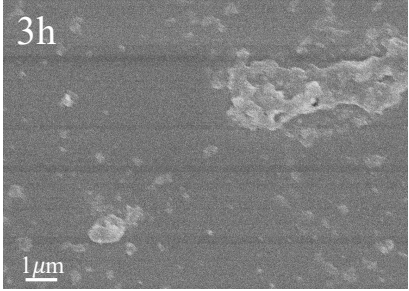


Figure 3.4. Optical microscope images of β -CD-PNP synthesis emulsion (top) and scanning electron microscope images of β -CD-PNP (bottom) synthesized with varying emulsion phase ratios (continuous phase: dispersed phase) (a) 10:1; (b) 20:1; (c) 40:1 (continuous phase = toluene, dispersed phase = MSA).

Table 3.1. β -CD-PNP emulsion polymerization reaction time screening (*Nanoparticle product not fully dried giving excess yield).

Trial	Reaction Time	Results	SEM Image
1	1 h	32 mg (43%)	
2	2 h	43 mg (57%)	
3	3 h	185 mg (100+%)*	

Finally, with the general emulsion formulation and reaction conditions set, the focus was shifted to optimize nanoparticle size. The degree of agitation introduced into

the emulsion has a large impact on nanoparticle size. Initially using vortex mixing agitation, an emulsion system yielding a broad size distribution of nanoparticles, ranging from ~100 – 600 nm, was obtained. To narrow the size distribution, probe sonication was employed as an additional and higher energy agitation source. The higher energy agitation improves the overall dispersion within the emulsion in two ways. First, the higher energy introduces more heat into the system, which further reduces the viscosity of both the dispersed and continuous phases and subsequently reduces the interfacial tension leading to improved dispersion stability. Second, the reduced interfacial tension allows for the formation of smaller micelles, which are more thermodynamically stable, as is observed for microemulsions. With probe sonication, an average nanoparticle size of 93 nm by SEM and 127 nm by DLS could be obtained (**Figure 3.5**). Good agreement between SEM and DLS demonstrates the size consistency and narrow size distribution that can be obtained with rigorous yet controlled agitation.

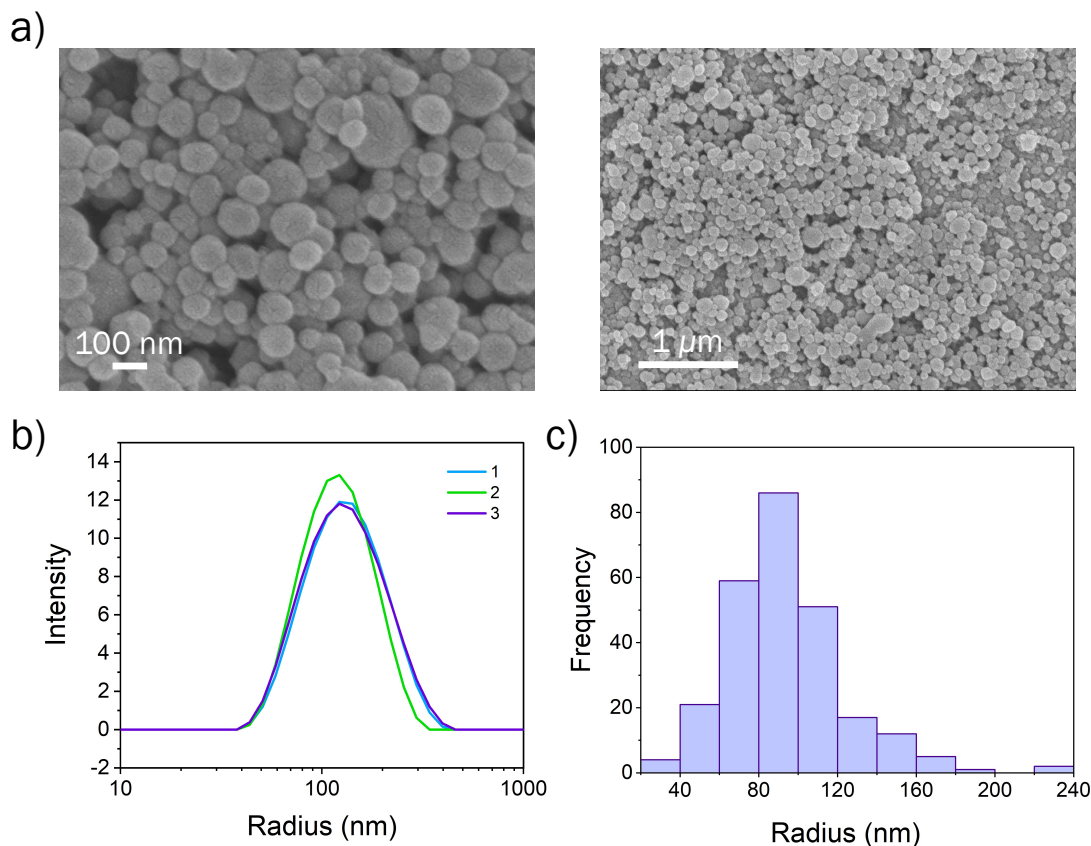


Figure 3.5. (a) Scanning electron microscope images of β -CD-PNP; (b) Dynamic light scattering size distribution curve of β -CD-PNP (1, 2, and 3 are individual measurements that are averaged to determine average particle size); (c) Size distribution curve from SEM image analysis of β -CD-PNP.

3.2.3. β -CD-PNP Characterization

Although the nanoparticulated morphology was clearly evidenced with microscopy techniques, investigation into the chemical constitution of β -CD-PNP is equally important for confirming their potential as functional macrocycle-derived polymer

nanoparticles. Extensive characterization of the nanoparticles is not possible due to the crosslinked nature of the material; however, a few key characterizations were investigated to confirm the similarity of β -CD-PNP and β -CD-PN. As observed for bulk β -CD-PN and evidenced by FTIR spectra, the primary crosslinking in β -CD-PNP occurs through the formation of ether linkages between cyclodextrin monomers (**Figure 3.6a and Table 3.2**). Along with ether formation, additional dehydration occurs via β -elimination during the MSA-catalyzed reaction. The degree of dehydration within the nanoparticles was calculated based on elemental analysis with the assumption of no carbon loss. Based on the elemental composition of β -CD-PNP (found: C, 77.58; H, 5.60; O, 16.82; S, 0.61%), it was estimated that 22.54 moles of water were lost per mole of β -cyclodextrin, slightly higher than the degree of dehydration with the bulk β -CD-PN material, which lost 19.46 moles of water per mole of β -cyclodextrin. Thermogravimetric analysis (TGA) of β -CD-PNP shows a similar decomposition profile and carbonization yield with β -CD-PN, further indicating the similar nature of the materials (**Figure 3.6b**). β -CD-PNP's modest increase in dehydration is corroborated by the slight increase in carbonization yield at 900 °C (50%) observed by TGA compared to that of β -CD-PN (47%). These data confirm the similar chemical natures of β -CD-PNP and β -CD-PN. With the successful synthesis of β -CD-PNP, the emulsion polymerization conditions were extended to be applied in the synthesis of α -cyclodextrin-based polymer nanoparticles (α -CD-PNP) and glucose-based polymer nanoparticles (Glu-PNP).

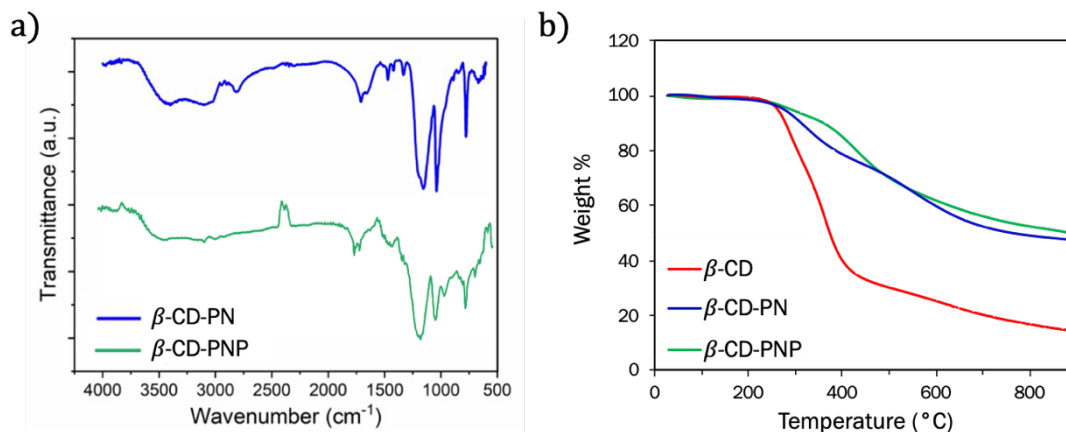


Figure 3.6. (a) FT-IR Spectra of β -CD-PN (blue) and β -CD-PNP (green); (b) Thermogravimetric analysis comparison of β -cyclodextrin (red), β -CD-PN (blue), and β -CD-PNP (green).

3.3. Conclusion

In summary, polymer nanoparticles based on β -CD-PN were synthesized because of the advantages inherent in the nanoparticulate morphology. Through meticulous formulation, emulsion polymerization was employed to successfully synthesize β -CD-PNP. Key characterizations indicate the chemical structures of β -CD-PN and β -CD-PNP are the same, with β -CD-PNP being moderately more dehydrated. An average nanoparticle size around ~ 100 nm was obtained with the appropriate amount of agitation. The formulation has been extended to other MSA-based syntheses for the preparation of α -CD-PNP and Glu-PNP.

The successful synthesis of cyclodextrin-derived polymer nanoparticles allows for the potential solution processing of a previously non-processible crosslinked polymer material. The improved processibility will be key for the practical application of these macrocycle-based functional materials. Because the chemical structure of the nanoparticles is similar to the bulk material, the promising adsorption characteristics observed for the bulk polymer are expected to be not only retained but improved in the nanoparticle morphology.

3.4. Experimental Details

3.4.1. General Methods

All starting materials and solvents were obtained from commercial suppliers and used without further purification. Sonication was performed using a Branson 2400 bath sonicator and a Hielscher UP100H ultrasonic processor for probe sonication. A VWR analog vortex mixer was used for initial emulsion agitation. Dynamic light scattering (DLS) measurements were obtained on a Malvern Zetasizer Nano ZS. Field-emission scanning electron microscopic (SEM) images were collected using a JEOL JSM-7500F FE-SEM at 5 kV. Samples were sputter coated in platinum/palladium prior to imaging. SEM images were analyzed using Image J processing and analysis software. Optical microscopy images were obtained using an Amscope microscope. Fourier transform infrared (FTIR) Spectroscopy was recorded using a Shimadzu IRAffinity-1S

spectrometer. Thermogravimetric analysis (TGA) was carried out with a TA Q500 thermogravimetric analyzer at a heating rate of $20^{\circ}\text{C min}^{-1}$ from 30°C to 900°C under N_2 atmosphere. Elemental analysis was performed by Robertson Microlit Laboratories for elemental CHN analysis. The extent of dehydration based on elemental analysis was calculated using the same method as reported in **Section 2.8.6**.

3.4.2. Synthetic Procedures

α -CD-PNP and β -CD-PNP: Cyclodextrin, either α or β , (0.50 g, 0.51 mmol if α -CD or 0.50 g, 0.44 mmol if β -CD) was dissolved in MSA (10 mL) via bath sonication. Cetrimonium bromide (CTAB) (0.73 g, 2.0 mmol) and dioctyl sulfosuccinate (AOT) (1.78 g, 4.0 mmol) were added into toluene (100 mL) and stirred. Once cyclodextrin fully dissolved, the MSA solution (dispersed phase) was added into the toluene solution (continuous phase) while stirring at 900 rpm. After the addition, the solution was mixed further with a vortex mixer for 2 min. Finally, the solution was probe sonicated at 40% amplitude for 45 min with continued stirring. Great care was taken to keep the reaction solution constantly stirring even when transferring between agitation methods. Once the probe sonication was complete, the reaction was heated at 90°C for 2 h with continuous stirring at 900 rpm. After 2 h, the toluene was removed with a rotary evaporator. The remaining contents of the reaction were washed with methanol: water (8:1, 4×45 mL) using centrifugation (4400 rpm, 20 min) to collect the nanoparticles between wash cycles. The collected nanoparticles were then dispersed in 500 mL of acetone and filtered through

a polyamide membrane (0.45 μm pore size, 47 mm diameter) to remove any non-nanoparticle material. The filtrate was collected and dried to give (**α -CD-PNP: 0.36 g, 72% yield**) and (**β -CD-PNP: 0.31 g, 62% yield**).

Glu-PNP: d-(+)-Glucose (0.50 g, 2.8 mmol) was dissolved in MSA (10 mL) via bath sonication. Cetrimonium bromide (CTAB) (0.73 g, 2.0 mmol) and dioctyl sulfosuccinate (AOT) (1.78 g, 4.0 mmol) were added into toluene (100 mL) and stirred. Once fully dissolved, the MSA solution (dispersed phase) was added into the toluene solution (continuous phase) while stirring at 900 rpm. After the addition, the solution was mixed further with a vortex mixer for 2 min. Finally, the solution was probe sonicated at 40% amplitude for 45 min with continued stirring. Great care was taken to keep the reaction solution constantly stirring even when transferring between agitation methods. Once the probe sonication was complete, the reaction was heated at 90°C for 2 h with continuous stirring at 900 rpm. After 2 h, the toluene was removed with a rotary evaporator. The remaining contents of the reaction were washed with methanol: water (8:1, 4 \times 45 mL) using centrifugation (4400 rpm, 20 min) to collect the nanoparticles between wash cycles. The collected nanoparticles were then dispersed in 500 mL of acetone and filtered through a polyamide membrane (0.45 μm pore size, 47 mm diameter) to remove any non-nanoparticle material. The filtrate was collected and dried (**Glu-PNP: 0.28 g, 56% yield**).

3.4.3. *Dynamic Light Scattering*

DLS data of nanoparticle dispersions was obtained on a Malvern Zetasizer Nano ZS. Nanoparticles were dispersed in acetone at approximately 0.05 mg/mL. The data from 3 measurement runs for the β -CD-PNP sample were averaged together by the Malvern software package.

3.4.4. *Scanning Electron Microscope Size Distribution*

SEM images were analyzed using Image J to obtain a size distribution. Nanoparticles were measured from 3 separate images for a total of 258 nanoparticles measured. Measurements were done by setting the scale in Image J based on the SEM scale bar and using the *measure* tool to measure the diameters of nanoparticles.

3.4.5. *Fourier Transform Infrared Spectroscopy*

A table of FTIR peak assignments is shown below for comparison of β -CD-PN and β -CD-PNP. The similarity between FTIR peaks for both materials confirms the consistent chemical structure between the bulk and nanoparticle materials.

Table 3.2. FTIR peak assignments of β -CD-PN and β -CD-PNP.

	β -CD-PN	β -CD-PNP
Functional Group	Absorption (cm⁻¹)	Absorption (cm⁻¹)
<u>C-O-H</u>	1039	1041
<u>C-O-C</u>	1157	1165
<u>C=C</u>	1658	1693
<u>C=O</u>	1710	1739
C= <u>C-H</u>	3101	3070
<u>O-H</u>	3400	3391

4. BTEX ADSORPTION AND SENSING BY CROSSLINKED CYCLODEXTRIN POLYMER NANOPARTICLES

4.1. Introduction

4.1.1. Environmental Context

Benzene, toluene, ethylbenzene, and xylenes (BTEX) represent a class of particularly concerning volatile organic compounds (VOC), because they are widespread throughout the environment and hazardous to human health.¹⁴¹ They are found ubiquitously in the environment, including indoor and outdoor air, surface water, groundwater, and soil. The omnipresence of BTEX is caused by both natural and anthropogenic sources. Some natural BTEX sources include volcanic eruptions and the combustion of organic matter, such as during forest fires. Anthropogenic sources are more concerning, in general, due to the multitude of different sources and the widespread nature of these sources. Among the most common anthropogenic sources are industrial processes, transportation exhaust, and leaching from household materials. Addressing the abundance of BTEX in the environment is of high priority due to the adverse health effects, both short-term and long-term, caused by BTEX exposure. Short-term effects of benzene exposure can include dizziness, memory dysfunction, and irritation of the eyes and throat.¹⁴² Of more concern are the long-term effects, which can include issues with the

nervous, respiratory, circulatory, and immune systems. Additionally, benzene is a known carcinogen with ethylbenzene being a suspected carcinogen.¹⁴³

The detection and removal of BTEX are both important research topics. Of the removal techniques being explored, adsorption is favorable because it often requires a low energy input, employment of inexpensive materials, and it typically allows for the efficient removal of BTEX.^{141,144} Additionally, the adsorption mechanism can also be applied in sensing.

4.1.2. BTEX Adsorption

Owing to the widespread presence and hazardous nature of BTEX, continuous exploration into better adsorption materials is underway. Activated carbons are the leading adsorbent applied in industrial and everyday practices. As such, activated carbons are often used as a comparable industry standard. The high surface areas, broad pore size distributions, high stabilities, and recyclability of activated carbons make them advantageous adsorbent materials.¹⁴⁵ Additionally, they can be produced from a wide variety of natural sources and further modified to tune their properties. Activated carbons tend to exhibit high adsorption capacities and efficient removal of an extensive range of pollutants including BTEX. An immense amount of research has focused on the solution phase adsorption of BTEX. Herein, this work focuses on the more challenging yet practically relevant vapor phase adsorption.

Beyond activated carbons, many other adsorbents, such as zeolites, Biochars, metal-organic frameworks (MOFs), specialized carbons, and organic polymers, have been explored for BTEX vapor adsorption.¹⁴⁴ In terms of BTEX adsorption materials, benzene and toluene are more commonly investigated. **Tables 4.1 and 4.2** summarize a representative survey of the literature of porous materials explored for benzene and toluene vapor adsorption from the past decade. These tables illustrate the general capacities that have been achieved with various benchmark porous materials, which typically range from 100-300 mg/g for both benzene and toluene, although a few exceptional materials have been reported. Numerous reviews are available for further reading on both vapor and solution phase VOC adsorption.^{141,144-147}

Table 4.1. Summary of benzene adsorption capacities of a variety of porous materials.

Adsorbent	Specific Surface Area (m²•g⁻¹)	Adsorption Capacity (mg•g⁻¹)	Reference
Benzene			
AC – Coconut Shell	868.0	336.0	148
AC – Walnut Shell ZnCl ₂	2643.0	510.0	149
Biochar – Date Palm Pits	1,100.0	93.7	150
Biochar – biowaste	1,397.0	144.0	151
Reduced Graphene Oxide	292.6	276.4	152
Graphene Oxide	236.4	216.2	152
Clay – Montmorillonite	69.5	141.2	153
Composite – Diatomite/Silicalite	348.7	246.0	154
Composite – Diatomite/MFI-Zeolite	286.9	62.5	155
MOF – MIL(Cr)-101	2,086.0	261.7	156
MOF – MIL-125-NH ₂	1,280.0	317.0	157
Hypercrosslinked Polymer	1,244.2	483.9	158
Hypercrosslinked Polymer	1,345.0	1,394.3	159
Hypercrosslinked Polymer	3,281.0	1,216.2	160

Table 4.2. Summary of toluene adsorption capacities of a variety of porous materials.

Adsorbent	Specific Surface Area (m²•g⁻¹)	Adsorption Capacity (mg•g⁻¹)	Reference
Toluene			
AC – Coal	838.0	137.3	161
AC – Wood (1)	1,284.3	184.0	161
AC – Coconut Shell (5)	570.7	62.5	161
AC – Commercial	932.0	260.0	162
AC – Commercial	905.2	227.3	163
AC – Walnut Shell ZnCl ₂	2643.0	680.0	149
Biochar – Cotton Stalks	1,256.0	319.0	164
Biochar – Barley Husk	600.2	161.3	163
Graphene Oxide	236.4	240.6	152
Reduced Graphene Oxide	292.6	304.3	152
Graphite Powder	292.6	304.4	165
Clay – Palygorskite	329.0	90.4	166
Composite – Zeolite/GO	1,112.0	116.0	167
Zeolites – MCM-41	1,081.0	184.0	168
Silica Gel	765.6	437.4	169
MOF – ZIF-67	1,401.0	224.0	170
MOF – UiO-66	1,414.0	166.0	170
MOF – MOF-199	1,237.0	159.0	170
MOF – MIL-101(Fe)	377.0	98.3	170
MOF – MIL-125-NH ₂	1,280.0	293.0	157
Hypercrosslinked Polymer	3,281.0	1,255.0	160

Although great strides have been made in the adsorption of BTEX, there are still some challenges that need to be addressed. For activated carbons and biochars, the regeneration process is energy intensive leading to higher overall operation costs and shorter material lifetimes.¹⁴⁴ Additionally, the production of these materials can release additional harmful VOCs into the atmosphere, which is counterproductive to remediation as a whole. For more specialized carbon materials, such as graphene and carbon nanotubes, the production is typically costly and time-consuming, which is not yet ideal for large scale applications. Similarly, the synthesis of zeolites and their composites can be complex and time-consuming. The starting materials can also be relatively expensive. MOFs are commonly regarded as highly promising adsorption materials, and VOC adsorption is no exception. However, the long-term robustness of MOF can be an issue for VOC adsorption, and the lack of available coordination or binding sites can limit their capacities despite very high surface areas. Additionally, the production cost of MOFs is high and further limits their practical application. Although Hypercrosslinked polymers boast extremely high adsorption capacities, the complex synthesis required for these materials hinders their potential scalability for practical application. Consequently, the development of simple syntheses towards robust, inexpensive materials with high adsorption capacities and efficient regeneration processes is of high priority. With the appropriate synthetic design, a material with built-in BTEX supramolecular binding sites could boast high adsorption capacities and low-energy regeneration processes.

Macrocycles are promising candidates for the development of such materials. However, the selective nature of macrocycles typically lends them to be employed in BTEX sensing rather than pure adsorption.

4.1.3. BTEX Electrical Vapor Sensing

Because of the hazardous nature of BTEX compounds, extensive work has been conducted towards developing highly sensitive sensors for their environmental monitoring. The development of real-time BTEX sensors is needed for both general environmental monitoring and personal exposure monitoring. Electrical vapor sensors are being continuously explored for real-time monitoring owing to their fast response times and low-cost production. For personal exposure monitoring, sensitivity and selectivity are the key features required for distinct, quantitative analysis of VOCs. Although various device architectures can be applied in electrical vapor sensing, chemiresistors are among the most popular architectures in recent years owing to their simple fabrication, sensitivity, and ease of modification. For BTEX sensing, the chemiresistors being investigated are primarily metal oxide-based sensors or carbon nanotube (CNT) based sensors.

Metal oxide-based chemiresistors have been widely explored for BTEX sensing. Metal oxides can be favorable for developing sensors due to their stability, simple preparation methodologies, cost-effectiveness, and relative non-toxicity.^{171,172} Although there are many promising aspects of metal oxide sensors, their high operation temperatures, high power consumption, and lack of sensitivity are common issues that

need to be overcome. Additionally, many metal oxide sensors are plagued by long response and recovery times. Various devices have been developed to overcome some of these issues, however a clear strategy for addressing all of them has not yet emerged. The sensing properties of metal oxide chemiresistors can be modified by mixing metal oxides, adding metal nanoparticles, adding organic functionalization, or a combination of multiple strategies. In one example, a mixed oxide film of ZnO and CdO was developed for selective benzene detection at room temperature, thus avoiding high operation temperatures.¹⁷³ The mixed oxide sensor demonstrated selectivity towards benzene, which was attributed to the standard enthalpy of benzene along with the interactions between benzene's π orbitals with the subshells of Zinc and Cadmium. To further elucidate selectivity in metal oxide-based sensors, a series of rhodium-functionalized TiO₂ nanoparticles were incorporated into a SnO₂ film at varying ratios.¹⁷⁴ The various sensors demonstrated slightly modified responses to BTX analytes. By employing principal component analysis, an array of the sensors was able to discriminate benzene, toluene, and p-xylene among other VOCs. Organic molecules, such as porphyrins, can be incorporated into metal oxide sensors to provide selectivity. Cobalt-porphyrin (Co-PP)-functionalized TiO₂ nanoparticles have been fabricated into chemiresistor devices that displayed enhanced BTX sensitivity owing to the favorable π -interactions with Co-PP.¹⁷² Overall, the chemiresistor could selectively detect toluene and p-xylene over other potential interfering analytes, such as NO₂, CO, and NH₃, but struggled to differentiate BTX

components. Despite these promising developments in metal oxide sensors, additional refinement of the sensing parameters and selectivity is needed for practical application in BTEX sensing.

Carbon nanotube chemiresistors have also been extensively explored for BTEX sensing owing to their high sensitivity, low operation temperatures, ease of fabrication, and potential miniaturization. Despite their favorable sensitivity, CNT devices tend to lack the selectivity required for BTEX analysis. Modifying the selectivity of carbon nanotubes while maintaining the sensitivity and low-cost is a major challenge in BTEX sensing. To address this challenge, macrocycles are often incorporated into CNT-based chemiresistors because they can add selectivity and enhance sensitivity without severely hindering the electrical properties of the device.

The Swager group has continually investigated the development of selective, sensitive CNT-based chemiresistor devices towards BTEX differentiation. Their strategy generally involves incorporating functionalized polymers into the CNT chemiresistors to modify the sensing properties and achieve selectivity.^{69,175,176} During their early work, single-walled carbon nanotubes wrapped in polythiophenes functionalised with calixarene macrocycles were fabricated into a chemiresistor for selective *p*-xylene detection.⁶⁹ When exposed to the vapors of different xylene isomers, the change in conductance for the calixarene-functionalized device was approximately two times stronger for the linear *p*-xylene compared with bulkier *o*-xylene and *m*-xylene indicating a stronger binding of *p*-

xylene. The control CNT device demonstrated no difference in response for the xylene isomers highlighting the importance of the macrocycle for the observed selectivity. Their more recent work focused on the interaction between CNTs and pentiptycene-poly(phenylene ethynylene).¹⁷⁶ Assembly of the pentiptycene units within the polymer both favorably disperses and aligns CNTs while creating well-defined, macrocycle-like cavities within the film that act as BTX binding sites. The pores also closely interact with CNTs in the film resulting in devices that demonstrated scaled responses to BTX following the trend of benzene < toluene < *o*-xylene for response intensity.

Similarly in 2018, Sarkar et al. fabricated chemiresistive devices based on C[4]RA-functionalised SWCNTs.^{21,177,178} The chemiresistor showed an increase in resistance when exposed to benzene, toluene, ethylbenzene, and xylenes (BTEX) with the greatest response to xylenes.²¹ The limit of detection for each of the BTEX analytes was determined to be 25, 7.5, 6.5 and 4 ppm, respectively, demonstrating the sensitivity and scaled response possible with macrocyclic receptors. Phthalocyanine and porphyrin macrocycles have also been utilized in BTEX sensing with CNT-based chemiresistors.^{179,180} In this work, significantly enhanced response intensities to xylenes were observed compared with benzene. This selectivity arises from the lesser interaction of benzene with the phthalocyanine and porphyrin binding sites, although the binding is not related to the macrocyclic cavities. Because of the flat nature of these macrocycles, xylenes can have both favorable π - π interactions and alkyl- π interactions, while benzene

lacks alkyl groups for additional interactions, indicating the important influence of even weak Van der Waals interactions.

Deep cavitands can be incorporated into CNT-based chemiresistors to enable exceptional selectivity by taking advantage of the thermodynamic favorability of binding in the deep, preorganized cavity. Utilizing this strategy, a sensor specially designed for benzene vapor detection was fabricated using a cavitand-gold nanoparticle-carbon nanotube hybrid material.¹⁸¹ Upon exposure to benzene vapor, a change in resistance was observed on the cavitand-functionalised sensor with the response intensity correlating with the benzene concentration. The sensor displayed a significantly larger change in resistance towards benzene compared with other VOCs tested, including similar yet bulkier toluene and o-xylene, demonstrating the enhanced benzene selectivity and sensitivity that is achieved with the deeper binding pocket. This selectivity could be attributed to a better fit of benzene within the deep-cavitand pocket in such a way that allows for a more favourable quadrupole alignment between the aromatic walls and benzene.

While promising selectivity and sensitivities have been achieved with varying chemiresistive systems, optimal real-time devices have not yet been achieved. Many of the metal oxide-based systems still suffer from high operational temperatures and power consumptions. Additionally, they tend to boast unpredictable selectivities, which hinders the strategic design of sensors for practical application. Carbon nanotube chemiresistors, on the other hand, have achieved highly promising, predictable selectivities by employing

macrocyclic materials. Unfortunately, the extensive synthesis required for many of the organic functional materials, which are responsible for the selectivity of the chemiresistors, limits their scalability and further practical application. New materials that are scalable, highly selective, and sensitive are still needed for improved real-time monitoring with electrical vapor sensing.

4.2. β -CD-PNP BTEX Vapor Adsorption

4.2.1. Benzene Sorption Isotherms

To initially probe the potential BTEX adsorption properties of β -CD-PNP, benzene sorption isotherms for as-synthesized and annealed nanoparticles were obtained. The benzene adsorption capacity can be determined from the sorption isotherms (**Figure 4.1**), giving an adsorption capacity of 378.1 mg/g at 0.078 atm, 294.15 K. The large hysteresis loop observed for β -CD-PNP indicates that capillary condensation is occurring within the material due to the small pore size, which was not measurable via N_2 isotherm.¹⁸² The broad nature of the hysteresis suggests a disordered structure of interconnected pores that have narrower necks.¹⁸³ These data are consistent with the amorphous nature of β -CD-PN materials and the general cyclodextrin structure. It was hypothesized that annealing could enhance the benzene adsorption capacity and enable BET surface area measurement by clearing out the pore space and further dehydrating the polymer backbone. However, as with β -CD-PN, a measurable BET surface area could not

be observed with N₂ isotherms for annealed or as-synthesized β -CD-PNP. The benzene adsorption capacities for β -CD-PNP after annealing at 400°C and 800°C for 1 hour decreased from 378.1 mg/g to 256.2 mg/g, and 206.2 mg/g (at 0.078 atm, 294.15 K), respectively (**Figures 4.2 and 4.3, Table 4.4**). These observations indicate that upon annealing, there is potentially some collapsing of the cyclodextrin cavities within β -CD-PNP leading to the observed decrease in benzene adsorption capacity.

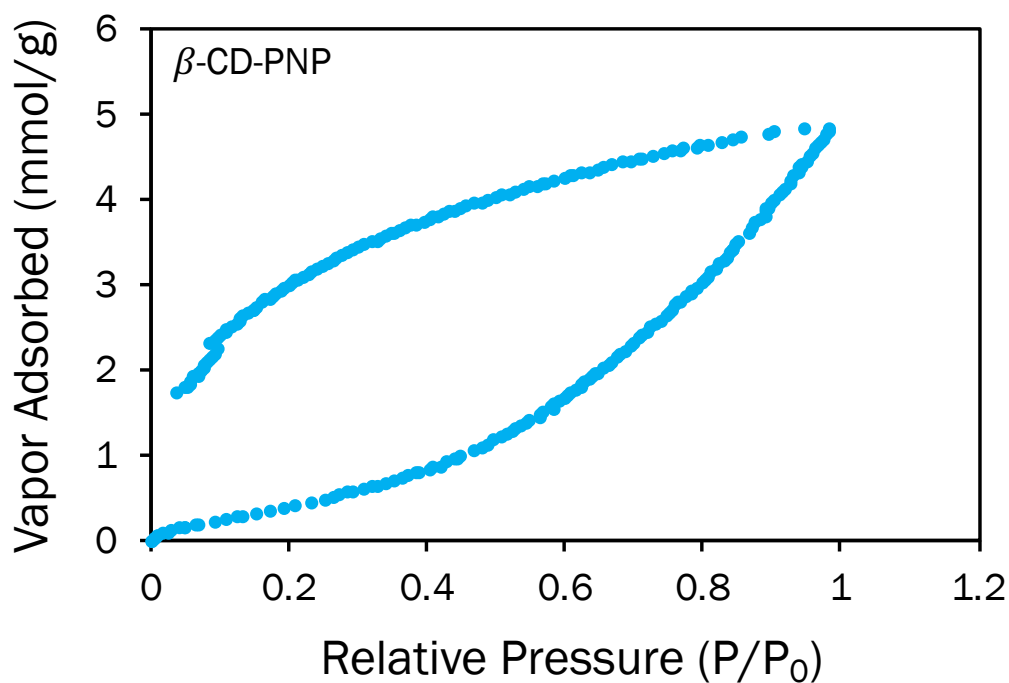


Figure 4.1. Benzene sorption isotherm for β -CD-PNP. Maximum adsorption at 4.84 mmol/g (378.1 mg/g) at 0.078 atm, 294.15 K (P = absolute pressure; P₀ = saturation pressure, ~ 0.079 atm).

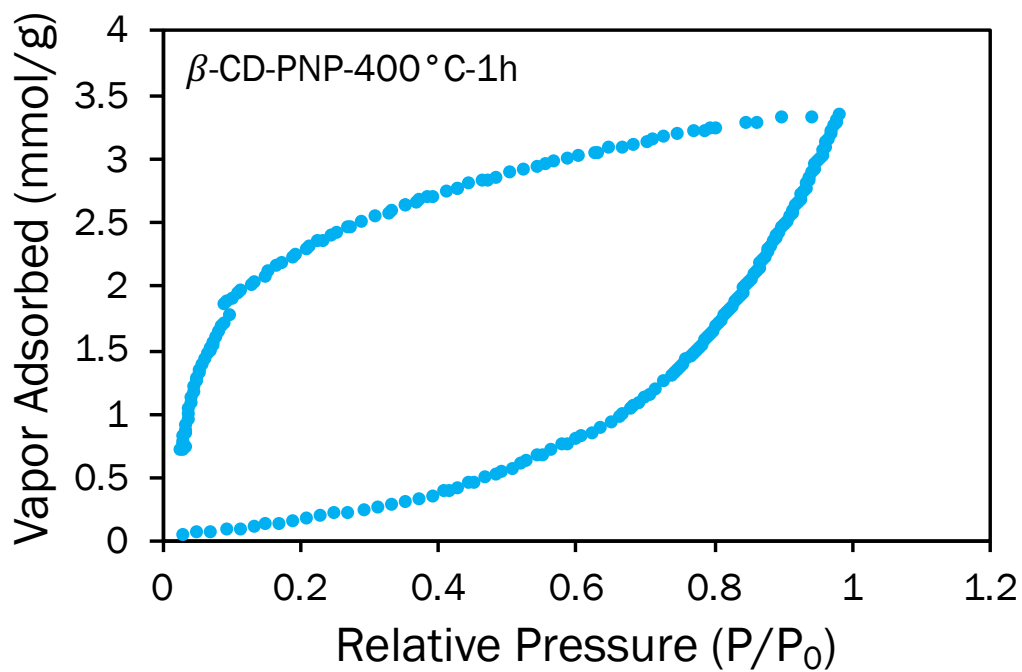


Figure 4.2. Benzene sorption isotherm for annealed β -CD-PNP-400°C-1h (400°C = annealing temperature; 1 hour = annealing time). Maximum adsorption at 3.31 mmol/g (258.5 mg/g) at 0.078 atm, 294.15 K (P = absolute pressure; P₀ = saturation pressure, ~ 0.079 atm).

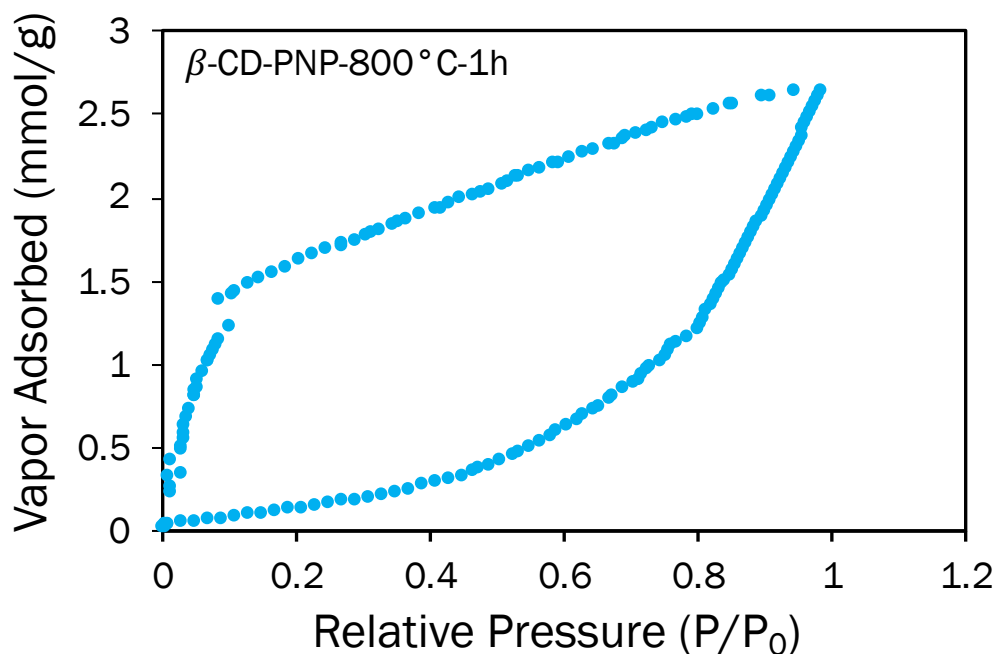


Figure 4.3. Benzene sorption isotherm for annealed β -CD-PNP-800°C-1h (800°C = annealing temperature; 1 hour = annealing time). Maximum adsorption at 2.64 mmol/g (206.2 mg/g) at 0.078 atm, 294.15 K (P = absolute pressure; P_0 = saturation pressure, ~ 0.079 atm).

To probe the importance of the macrocyclic cavity, the benzene sorption isotherms of α -CD-PNP and Glu-PNP were investigated. The overall adsorption capacity of α -CD-PNP was much less than β -CD-PNP with α -CD-PNP adsorbing 114.0 mg/g of benzene (at 0.078 atm, 294.15 K), while Glu-PNP adsorbed a minimal amount of benzene at 12.5 mg/g (at 0.078 atm, 294.15 K) (**Figures 4.4 and 4.5, Table 4.4**). Although these isotherms give some insight into the benzene adsorption properties of α -CD-PNP and Glu-PNP, it is

important to note that these measurements could contain some error due to the small amount of nanoparticle material that was available for analysis. Overall, these materials demonstrate the great importance of the macrocyclic binding site along with the influence the size of the binding site can have on the general binding properties.

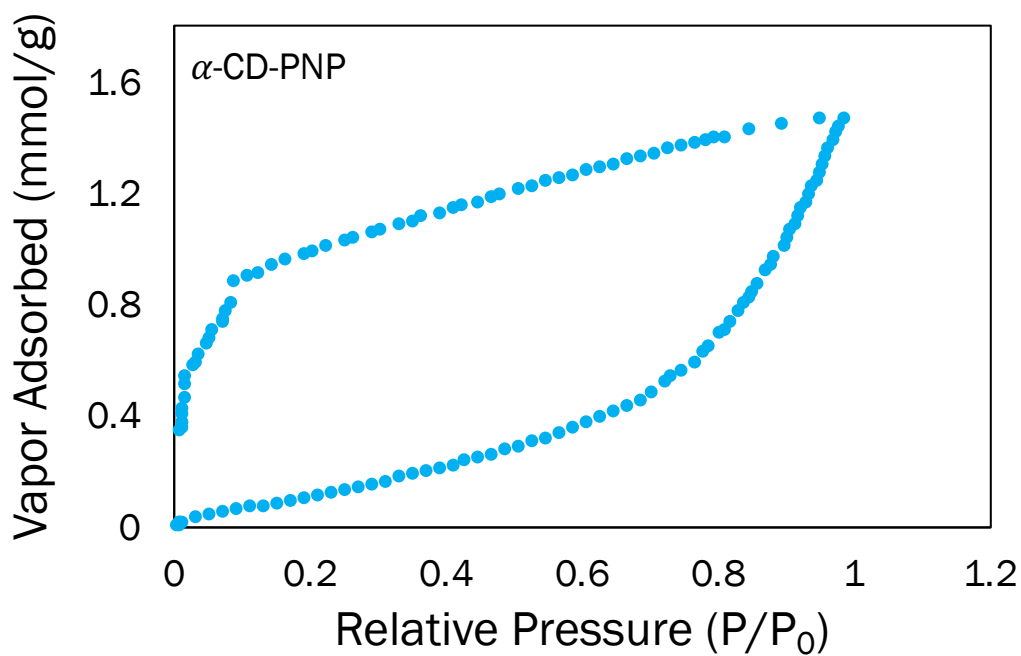


Figure 4.4. Benzene sorption isotherm for α -CD-PNP. Maximum adsorption at 1.46 mmol/g (114.0 mg/g) at 0.078 atm, 294.15 K (P = absolute pressure; P₀ = saturation pressure, ~ 0.079 atm).

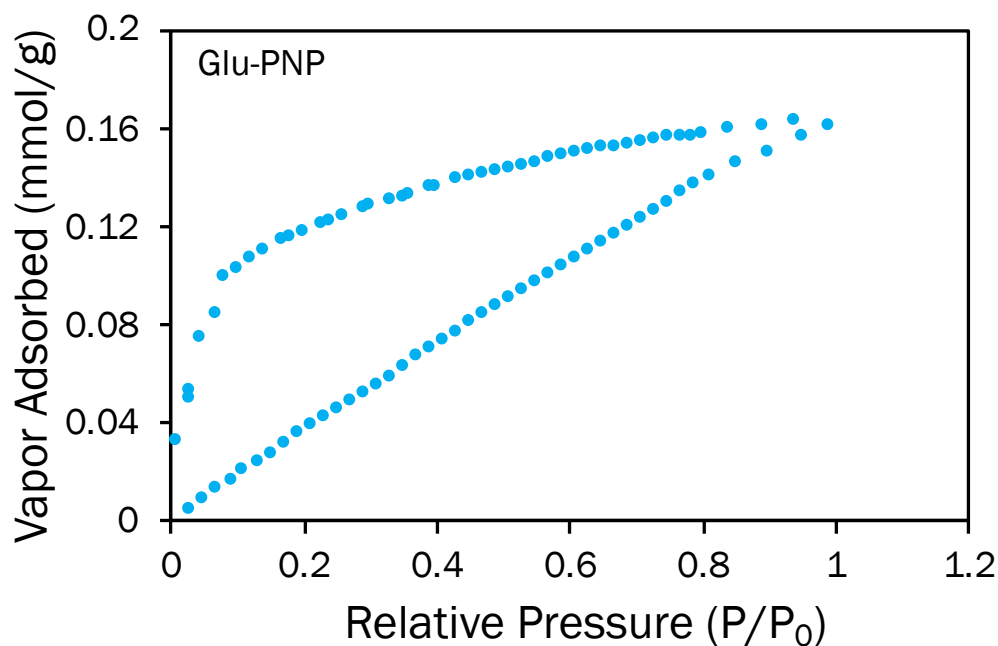


Figure 4.5. Benzene sorption isotherm for Glu-PNP. Maximum adsorption at 0.16 mmol/g (12.5 mg/g) at 0.078 atm, 294.15 K (P = absolute pressure; P_0 = saturation pressure, ~ 0.079 atm).

The benzene sorption isotherm for bulk β -CD-PN was also investigated to confirm the importance of the nanoparticulate morphology on the adsorption capacity. It is evident that strict morphological control is key to unlocking the adsorption potential for these cyclodextrin-derived polymer materials with the benzene adsorption capacity being increased seven-fold in β -CD-PNP compared with β -CD-PN (57.8 mg/g at 0.078 atm, 294.15 K) (**Figure 4.6, Table 4.4**). The benzene sorption isotherm of activated carbon was also measured as an industry standard, due to its common application in BTEX adsorption.¹⁴⁹ The benzene adsorption capacity of β -CD-PNP is slightly lower than that

of activated carbon (489.7 mg/g at 0.078 atm, 294.15 K) but is still within a comparable range (**Figure 4.7, Table 4.4**). However, β -CD-PNP is expected to have a strong advantage in terms of selectivity for sensing applications due to the persistent supramolecular binding site inherent in β -cyclodextrin, as was observed during the solution adsorption investigation.

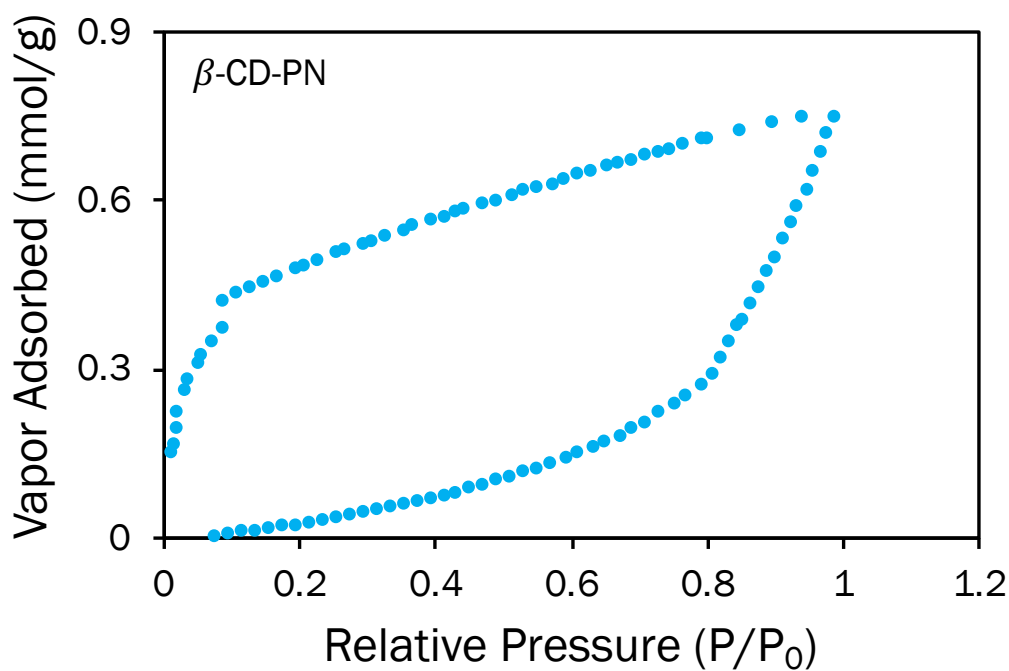


Figure 4.6. Benzene sorption isotherm for β -CD-PN. Maximum adsorption at 0.74 mmol/g (57.8 mg/g) at 0.078 atm, 294.15 K (P = absolute pressure; P_0 = saturation pressure, ~ 0.079 atm).

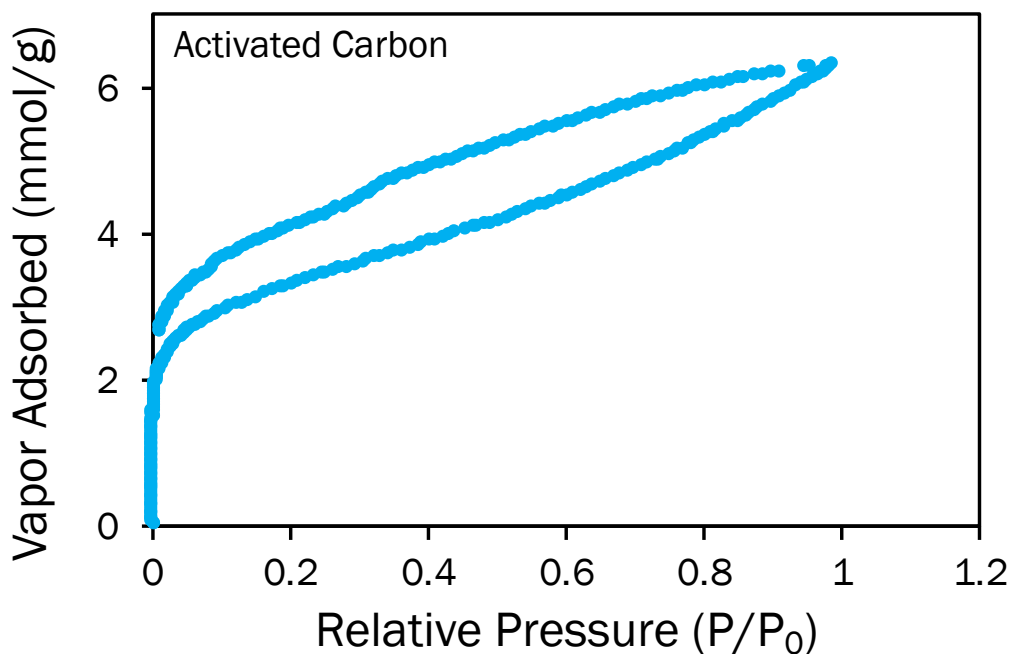


Figure 4.7. Benzene sorption isotherm for activated carbon. Maximum adsorption at 6.27 mmol/g (489.7 mg/g) at 0.078 atm, 294.15 K (P = absolute pressure; P_0 = saturation pressure, ~ 0.079 atm).

To investigate the potential selectivity, toluene sorption isotherms were also evaluated (**Figures 4.15 - 4.21**). The toluene isotherms mostly echoed the observations extracted from the benzene isotherms, while also demonstrating the superior selectivity of β -CD-PNP compared with the other materials. Because of the exceptional benzene adsorption capacity and potential selectivity demonstrated, subsequent investigation was primarily focused on as-synthesized β -CD-PNP.

4.2.2. BTEX Saturated Vapor Adsorption

The BTEX vapor adsorption selectivity was further investigated using a saturated vapor exposure technique, which is feasible to be measured on all BTEX components of interest. For these measurements, a pre-weighed sample was placed in a sealed container with an open vial of BTEX liquid for 24 hours and weighed after vapor exposure to calculate the adsorption capacity; a detailed experimental description can be found in **Section 4.4.3**. The BTEX saturated vapor adsorption of as-synthesized and annealed β -CD-PNP, bulk β -CD-PN, β -cyclodextrin powder, and activated carbon was initially investigated (**Figure 4.8**). In follow up experiments, the BTEX adsorption of α -CD-PNP and Glu-PNP was also investigated in comparison to β -CD-PNP (**Figure 4.9**).

The BTEX saturated vapor adsorption of β -CD-PNP follows the expected selectivity pattern based on analyte size and shape complementarity with the β -cyclodextrin cavity (benzene > toluene > ethylbenzene > *o*-xylene > *m*-xylene). Annealing β -CD-PNP modifies the adsorption selectivity in a less predictable pattern. The selectivity transformation is a complex phenomenon with dehydration and cavity collapse simultaneously occurring. At lower temperature annealing, dehydration most likely predominates the transformation leading to enhanced toluene adsorption and selectivity more dramatically favoring both benzene and toluene. However, higher temperature annealing lends itself more towards potential cavity collapse yielding significantly decreased adsorption capacity (**Figure 4.8 and Table 4.4**). β -CD-PN maintains the

benzene-toluene selectivity observed in its nanoparticle counterpart, however, the adsorption pattern towards bulkier BTEX molecules is less predictable. The bulk powder morphology of β -CD-PN significantly hinders the accessibility of the binding sites for the analyte vapors causing this shift towards less predictable selectivity and lower adsorption capacities. Additionally, β -CD-PN is more hygroscopic than β -CD-PNP, which causes humidity to more significantly affect the adsorption measurements of β -CD-PN. Furthermore, the enhanced adsorption capacities and predictable nature of the adsorption for β -CD-PNP compared with β -CD-PN indicate the importance of the nanoparticle morphology.

To demonstrate the influence of the polymer network on the adsorption properties of β -cyclodextrin, BTEX saturated vapor adsorption of as-purchased, crystalline β -cyclodextrin was collected. β -cyclodextrin in its natural state adsorbs a negligible amount of all BTEX components (**Figure 4.8**). The lack of adsorption is potentially due to the tight crystal packing of β -cyclodextrin caused by favorable hydrogen bonding interactions, which hinders the accessibility of the binding site cavity.¹⁸⁴ The minimal BTEX adsorption for crystalline β -cyclodextrin highlights the critical importance of material design. Although the inclusion properties of cyclodextrins are inherent due to the internal cavity, subsequent incorporation into functional materials, such as polymer networks, is crucial for practical application of the binding properties.

The saturated vapor adsorption of activated carbon demonstrated a lack of selectivity towards any specific BTEX component (**Figure 4.8**). The overall adsorption capacities of activated carbon were somewhat comparable, albeit lower for benzene, compared with β -CD-PNP, however, the clear trend in selectivity observed for β -CD-PNP was not present. The general strong BTEX adsorption performance of activated carbon is desirable for simple removal-based applications. β -CD-PNP, on the other hand, is favorable for more sophisticated applications requiring specific selectivity, such as sensing.

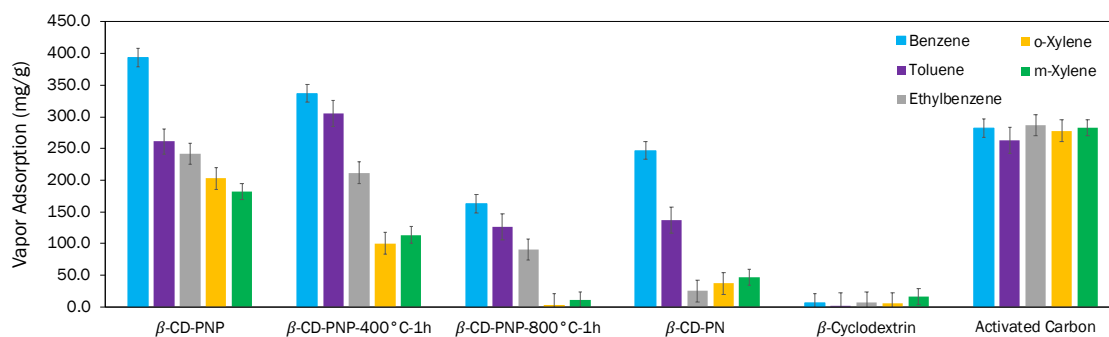


Figure 4.8. BTEX saturated vapor adsorption data for β -cyclodextrin-derived materials and activated carbon. β -CD-PNP-400°C-1h and β -CD-PNP-800°C-1h are annealed nanoparticles.

Based on the superior BTEX adsorption performance of non-annealed, nanoparticulated β -CD-PNP, the BTEX adsorption properties of nanoparticles of α -cyclodextrin (α -CD-PNP) and glucose (Glu-PNP) were investigated (**Figure 4.9**). As observed with the sorption isotherms, α -CD-PNP and Glu-PNP had lower BTEX adsorption capacities than β -CD-PNP indicating the more favorable binding of the β -cyclodextrin cavity towards BTEX. However, β -CD-PNP, α -CD-PNP and Glu-PNP demonstrate varied selectivities towards BTEX molecules, which could be valuable in a sensor array. As mentioned previously, β -CD-PNP demonstrated scaled adsorption capacities following analyte size with benzene adsorption being significantly higher than other BTEX analytes. α -CD-PNP, on the other hand, demonstrated a more significant difference between toluene and ethylbenzene owing to the smaller cavity size of α -cyclodextrin, which can differentiate the subtle structural difference. However, α -CD-PNP exhibited weaker selectivity towards xylene isomers and would not be expected to differentiate them. Despite its lack of macrocyclic binding site, Glu-PNP demonstrated potential adsorption selectivity between benzene and toluene, while the adsorption of ethylbenzene, *m*-xylene, and *o*-xylene were all similar. These polymer nanoparticles all demonstrate selectivity that is not observed in activated carbon. The inherent selectivity of these materials could enable their future application in BTEX sensing. Although higher capacity of β -CD-PNP should enhance the device sensitivity when incorporated into a

sensor, the varied selectivity of α -CD-PNP and Glu-PNP are valuable to be employed in an array of sensors for “finger-print” response to complex BTEX-containing samples.

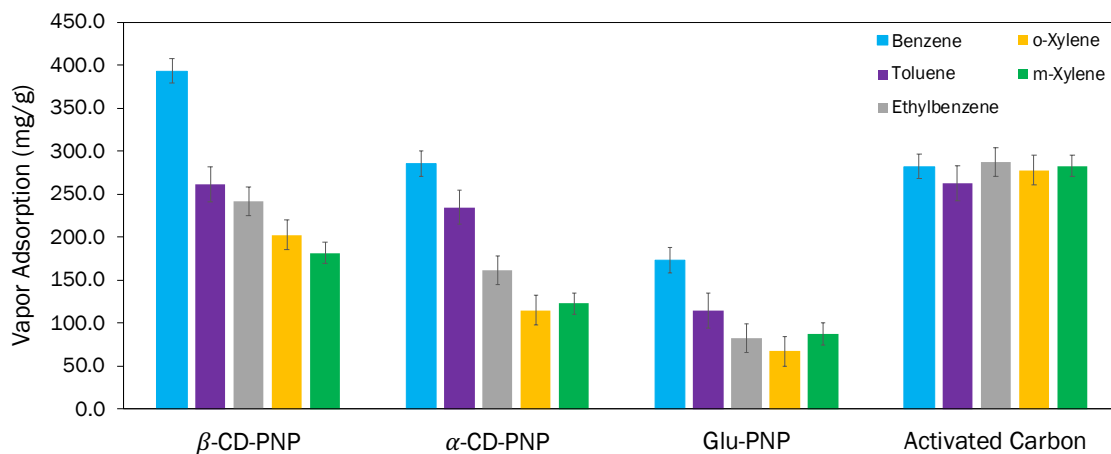


Figure 4.9. Comparison of BTEX saturated vapor adsorption data for β -/ α -cyclodextrin- and glucose-based nanoparticles and activated carbon.

Overall, β -CD-PNP demonstrated the highest adsorption capacities in this work along with predictable size-based selectivity. In literature, benzene and toluene adsorption capacities tend to range between 100 – 300 mg/g, although some exceptional capacities have been reported (Tables 4.1 and 4.2). β -CD-PNP boasts similar capacities with added selectivity that is not typical of many adsorbents. Although the overall adsorption capacity of α -CD-PNP is lower than β -CD-PNP, the capacity is within the range of benchmark

materials while also possessing the added benefit of selectivity. These promising adsorption properties endow α -CD-PNP and β -CD-PNP with potential in multiple applications.

4.3. BTEX Vapor Sensing

4.3.1. Vapor Sensor Fabrication

Based on the selectivity observed in the vapor adsorption experiments, it was envisioned that the cyclodextrin-based nanoparticles could be ideal candidates as receptors within a vapor sensor. Beyond selectivity, β -CD-PNP is expected to greatly enhance the sensitivity of the device response owing to the crosslinked nature of the polymer, which theoretically endows β -CD-PNP with a higher density of binding sites. Additionally, the solution processibility of the nanoparticles enables their incorporation into a functional composite device using simple methods.

To investigate the sensing potential of β -CD-PNP, a simple chemiresistive device architecture was chosen to avoid extensive fabrication (**Figure 4.10a**). Carbon nanotubes (CNT) were explored as the base conductive material for the chemiresistor. They are known to be highly sensitive to changes in their local chemical environment owing their large surface area, which also enables extensive interactions with molecular receptors, making them great candidates for highly sensitive devices.^{185,186} Like nanoparticles,

carbon nanotubes can be solution processed into functional devices with spin coating, drop casting, and spray coating being extensively explored as simple and cheap fabrication techniques.

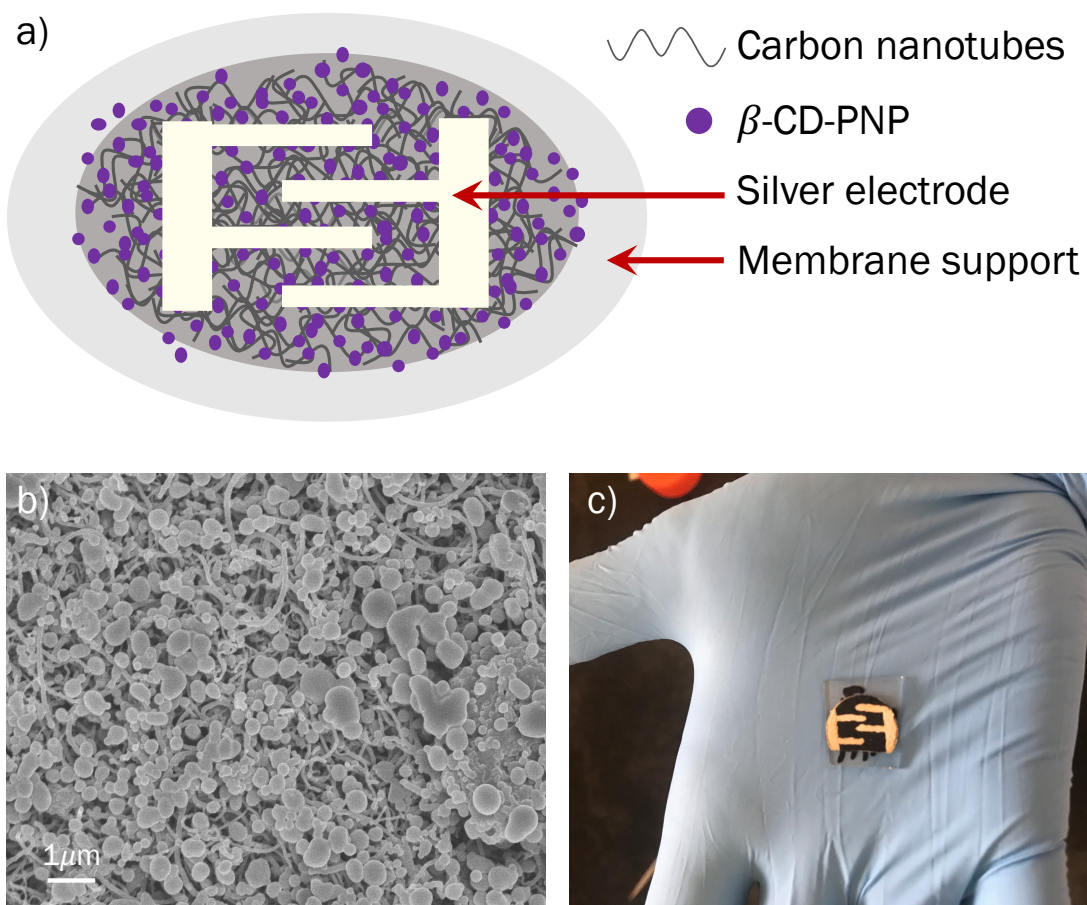


Figure 4.10. (a) General schematic of β -CD-PNP/CNT composite chemiresistor device architecture; (b) SEM image of β -CD-PNP/CNT composite film; (c) digital photograph of β -CD-PNP/CNT composite chemiresistor device.

To begin the fabrication of a β -CD-PNP/CNT functional composite, the consistent fabrication of CNT films is a critical first step. Carbon nanotubes were dispersed in N-methyl-2-pyrrolidone (NMP) via probe sonication. Spray coated and drop casted films were found to yield inconsistent CNT films. To avoid extensive optimization, filtration-based casting of the carbon nanotubes was employed. Using this technique, a well-dispersed CNT solution was filtered onto a membrane to form a CNT film. This process allowed for the quick fabrication of consistent CNT films because it enables facile, straightforward control over the critical parameters, such as CNT concentration and solution volume (**Figure 4.23**).

With consistent CNT films in hand, the next step was the integration of β -CD-PNP with the CNT films to form a composite film. A few simple techniques were envisioned to achieve a high interaction level between β -CD-PNP and the CNTs to optimize the device sensitivity. The first method investigated was the simultaneous casting of the CNTs and β -CD-PNP via vacuum filtration because they both disperse well in NMP. Unfortunately, with this process, the nanoparticles were not retained within the film due to the larger pore size of the membrane substrate. Sequential filtration was examined next, however, issues with nanoparticle retention remained. Following these attempts, a more vigorous fabrication method was explored. The entire CNT film and membrane were soaked in a nanoparticle solution followed by subsequent drying and cycles. This procedure yielded much better nanoparticle integration with the CNT film and was used

for further investigation. (**Figures 4.10b and 4.22**). Finally, with the successful fabrication of a β -CD-PNP/CNT composite, interdigitated electrodes were deposited to the films with silver paste (**Figure 4.10c**).

4.3.2. Sensing Chamber Design

With the successful fabrication of a β -CD-PNP/CNT composite device, a sensing chamber was designed and constructed to test the sensing performance.¹⁸⁷ The goal of the set up was to obtain qualitative, proof-of-concept data that could be improved and expanded upon if promising results were observed. The general design concept is shown in **Figure 4.11a**. The two main features to be considered were the gas flow and resistance measurement of the device. For the gas flow a simple vapor bubbling followed by gas mixing set up was developed. In this method, the initial air inlet was split with a Y-valve so that half could go directly to the chamber and half could go into a sealed flask to bubble BTEX liquids. With the bubbling, the vapors could go to a second Y-valve to allow for the remixing of the air and BTEX vapors to enter the chamber with the device. Additionally, a constant vacuum was applied to the chamber to encourage the air flow, prevent pressure build up, and purge the chamber in between BTEX exposures. The valves allow for strict control over when the BTEX is being bubbled and when it enters the sensing the chamber. In the set-up of the chamber itself, proper sealing of the chamber to prevent any leakage was key for both safety and proper data collection.

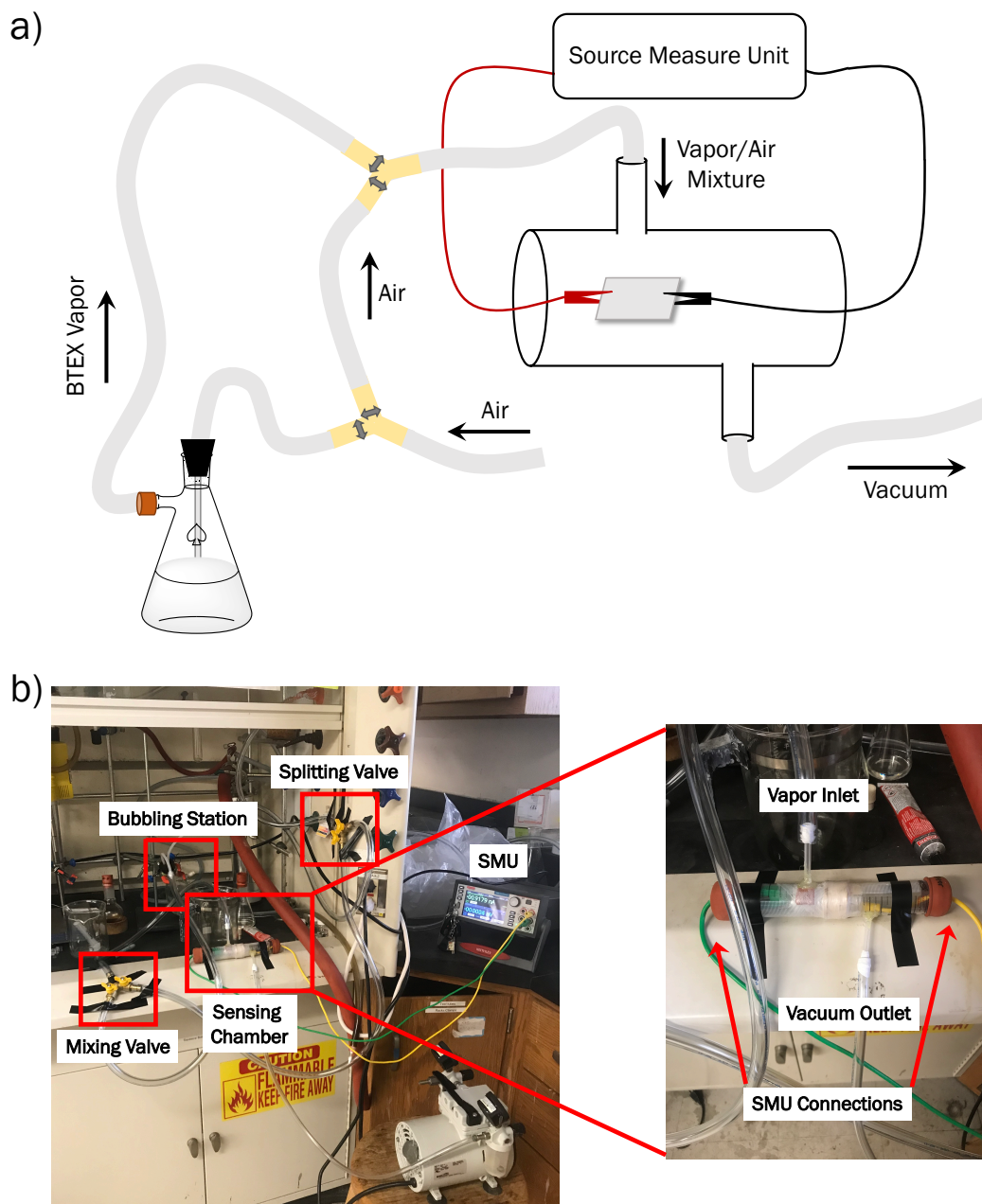


Figure 4.11. (a) General schematic of the sensing chamber design demonstrating air flow and connectivity (Note: dimensions are not to scale); (b) Digital photograph of the whole sensing chamber set up (left) with a zoomed in look at the sensing chamber itself (right).

The resistance of the β -CD-PNP/CNT composite device was measured using a simple source measure unit (SMU) that was connected to the electrodes via alligator clips. With this SMU, I-V curves along with time vs resistance data could be obtained to characterize the device and sensor response. The chamber was constructed from objects readily available in the lab (**Figure 4.11b**), which is described in further detail in **Section 4.4.6**. Using this simple sensing chamber design, the device responses to BTEX vapors could be tested in a qualitative manner to determine if the selectivity observed in adsorption is maintained in a functional device.

4.3.3. BTEX Sensing

Once the sensing chamber was constructed, the β -CD-PNP/CNT composite device performance could be qualitatively tested. During testing benzene, toluene, ethylbenzene, *o*-xylene, and *m*-xylene were bubbled individually and the change in resistance was calculated and normalized as the sensor response. The response of a control device without nanoparticles was investigated first. This CNT device displayed marginal responses to each of the vapors, which is expected of CNTs owing to their sensitivity to their chemical environment. However, no significant difference or size-based correlation of the responses could be distinguished (**Figure 4.12a**).

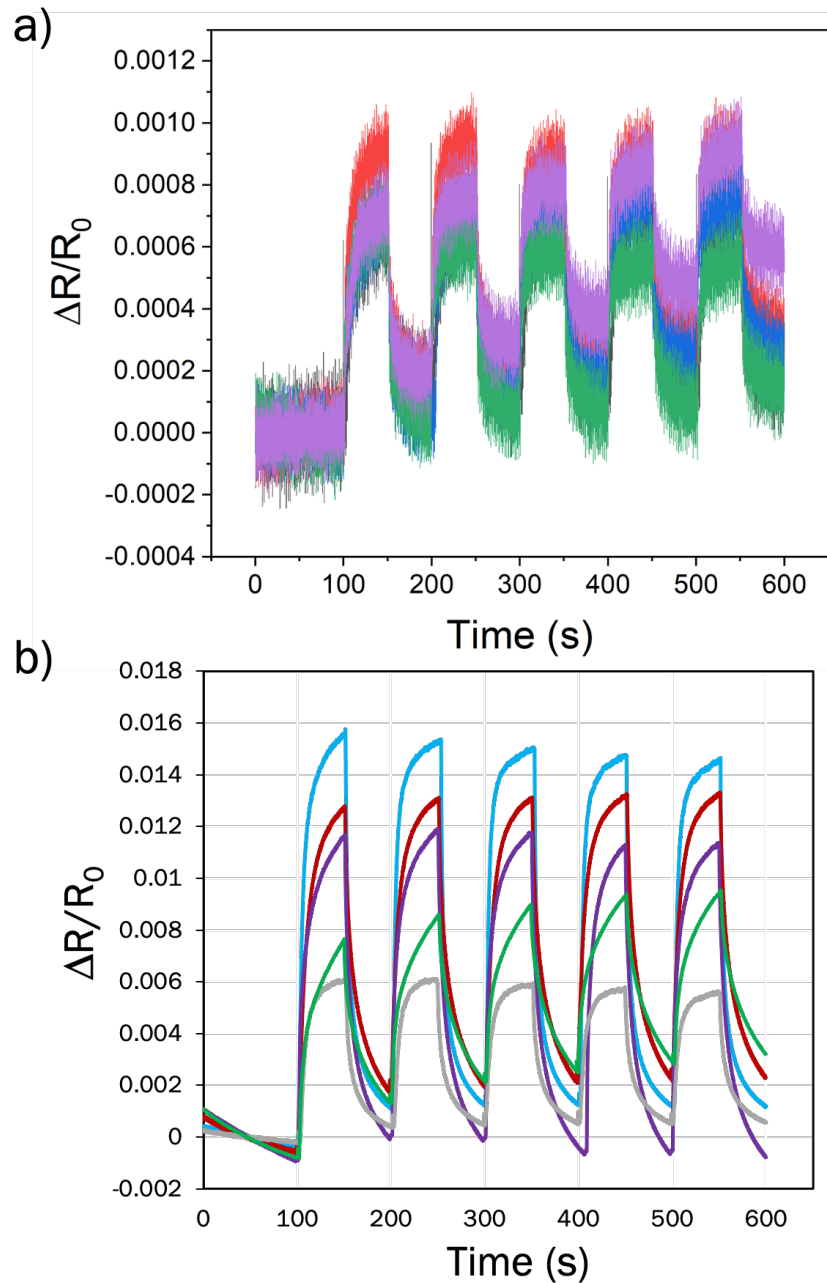


Figure 4.12. Real-time sensor response to BTEX vapors for (a) CNT control and (b) β -CD-PNP/CNT composite device. (benzene = blue, toluene = red, ethylbenzene = purple, *o*-xylene = green, *m*-xylene = grey; $\Delta R = (R_{\text{vapor}} - R_0)$, $R_0 = R_{\text{air}}$).

The β -CD-PNP/CNT composite device, on the other hand, demonstrated a scaled response intensity for each of the BTEX vapors. With the composite device, a clear trend between response intensity and analyte size was observed indicating the selective nature of the composite is derived from the macrocyclic binding sites within β -CD-PNP (**Figure 4.12b**). Additionally, these data correlate well with the data obtained from BTEX saturated adsorption experiments for β -CD-PNP following the same size-based adsorption trend (**Figure 4.8**). Beyond endowing the composite with selectivity, β -CD-PNP significantly enhances the sensitivity of the response to BTEX vapors. For benzene, the response intensity of the β -CD-PNP/CNT composite is 19 times higher than that of the CNT control, while being 6 times higher for *m*-xylene, the lowest overall response for the β -CD-PNP/CNT composite device (**Figure 4.13**). This response sensitivity enhancement is among the best when compared with the current literature (**Table 4.3**). Although these data are primarily qualitative, they demonstrate the great potential of β -CD-PNP in BTEX sensing. The preorganized binding sites of cyclodextrin enable the selective binding of analytes, while the direct crosslinking endows β -CD-PNP with a high density of these binding sites, which together enable the overall enhanced device performance when β -CD-PNP is incorporated into a vapor sensor.

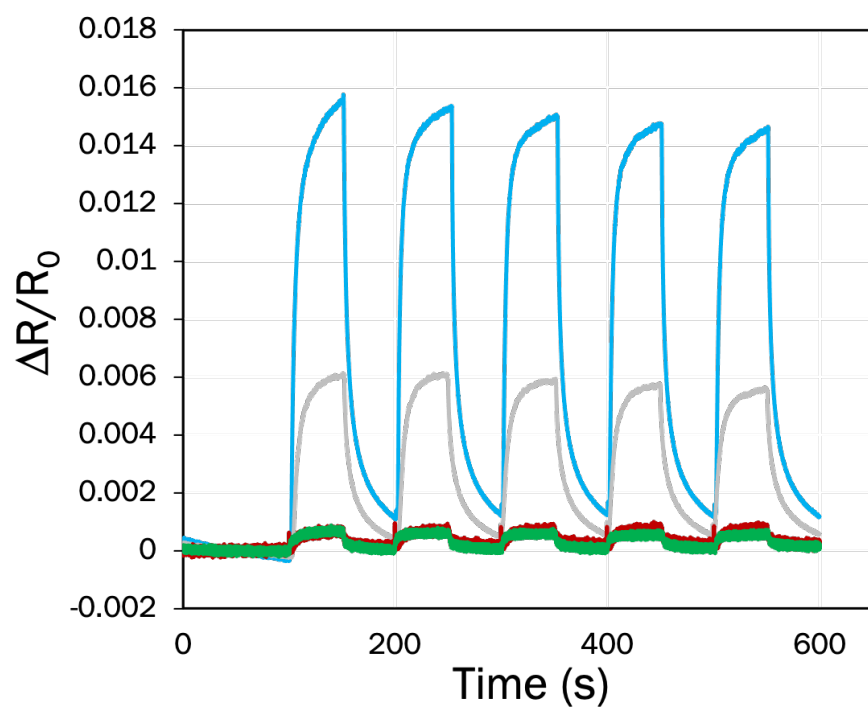


Figure 4.13. Real-time sensor response comparison for CNT control device (benzene = red, *m*-xylene = green) and β -CD-PNP/CNT composite device (benzene = blue, *m*-xylene = grey).

Table 4.3. Comparison of BTEX sensors with the calculated response improvement of their device compared with their control device. (*Value estimated from figures provided in manuscript; $Response\ enhancement = \frac{Experimental\ Device\ Response}{Control\ Device\ Response}$).

Sensor-Type	Sensor Material	Response Measurement	Analyte	Response Enhancement	Ref.
CNT Chemiresistor	Cyclodextrin polymer (β -CD-PNP)/CNT	Resistance	Benzene Toluene Ethylbenzene o-Xylene m-Xylene	19.4 16.2 14.3 8.8 6.8	This Work
Metal Oxide Chemiresistor	Cobalt Porphyrin-TiO ₂ NP	Resistance	Toluene	2.5	172
CNT Chemiresistor	Pentiptycene polymer-CNT	Conductance	Benzene Toluene o-Xylene	26.0* 15.0* 9.0*	176
CNT Chemiresistor	Pentafluorophenylacetyl-functionalized cellulose acetate-CNT	Conductance	Benzene Toluene m-Xylene	2.0* 4.3* 2.8*	175
CNT Chemiresistor	Calix[4]resorcinarene-CNT	Resistance	Ethylbenzene	17.5*	21
Metal Oxide Chemiresistor	Rh-TiO ₂ /SnO ₂	Resistance	Benzene Toluene p-Xylene	4.5* 5.6* 4.5*	174
Metal Oxide Chemiresistor	Co-C ₃ N ₄ /ZnO	Resistance	Benzene Toluene Ethylbenzene o-Xylene m-Xylene p-Xylene	1.4* 8.5* 3.1* 8.4* 7.0* 11.0	171
CNT Chemiresistor	Calix[4]arene-polythiophene / CNT	Conductance	p-Xylene	2.4*	69

To obtain semi-quantitative sensing data, the sensing chamber was modified and sealed to allow for the injection of a controlled volume of benzene headspace while the chamber was under vacuum. This modification allowed for a known amount of benzene to be injected into the sensing chamber while measuring the device resistance. A series of benzene injections of the same concentration but varying volumes were injected into the chamber and the subsequent response was measured. The β -CD-PNP/CNT composite device demonstrated a scaled response with the amount of benzene injected into the chamber (**Figure 4.14**). From this data, an estimated limit of detection (LOD) could be calculated to be ~ 279 ppb. While this result is extremely promising, more strenuous quantitative data obtained with a more sophisticated set up is needed. Additionally, measuring data points closer to the LOD is necessary to further validate the calculation.

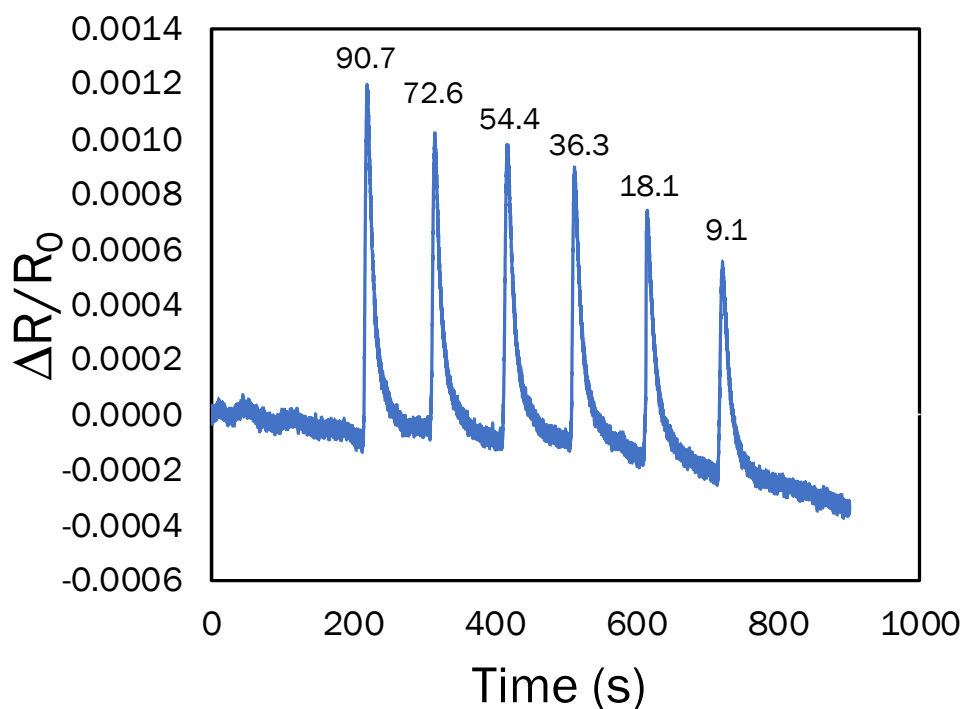


Figure 4.14. Real-time β -CD-PNP/CNT composite response vs time to varying concentrations of benzene. Concentrations in ppm are listed above each response.

4.4. Conclusion

The BTEX adsorption and sensing properties of β -CD-PNP were investigated through benzene sorption isotherms, saturated vapor adsorption experiments, and qualitative sensing experiments. The benzene sorption isotherms demonstrated the negative effects of annealing on the β -CD-PNP adsorption capacity. Additionally, the isotherms highlight the important role morphology plays in the adsorption properties. The nanoparticle morphology allows for greater accessibility of the β -cyclodextrin binding

sites allowing for higher adsorption capacities along with improved selectivity, which is demonstrated in both the sorption isotherms and saturated vapor adsorption measurements. Additionally, the adsorption capacity of β -CD-PNP was comparable to activated carbon among other benchmark materials. Saturated vapor adsorption measurements demonstrated the exemplary selectivity of β -CD-PNP and α -CD-PNP towards BTEX molecules that are more complementary with their respective cavity sizes. This favorable selectivity is critical for some sophisticated applications, such as sensing. Furthermore, the nanoparticle morphology allows for solution processing of a previously non-processible crosslinked polymer, enhancing its potential for real-world application into devices where selectivity is required.

Based on the promising selective adsorption demonstrated by β -CD-PNP, a composite chemiresistive device of CNT and β -CD-PNP was developed using simple fabrication methods. The sensing potential of the composite was investigated with a sensing chamber that was designed and constructed in-house with common lab materials. Qualitative sensing experiments were conducted for the β -CD-PNP/CNT composite device. The composite demonstrated excellent selectivity towards the smaller BTEX components aligning well with the adsorption data previously obtained. The β -CD-PNP/CNT composite device displayed selectivity that was not observed with a CNT control device, which showed a marginal response to each BTEX vapor with no distinguishable response pattern. In addition to enhanced selectivity, the β -CD-PNP/CNT

composite demonstrated significantly enhanced sensitivity when compared with the CNT control with the response being 19 times greater for benzene. Additionally, through a series of calculations a tentative limit of detection was determined to be ~279 ppb. While mostly qualitative data has been obtained thus far, these experiments demonstrate the proof of concept in the material design towards functional macrocyclic materials for BTEX sensing. The importance of the macrocyclic binding site is highlighted by the selectivity, while the sensitivity highlights the significance of the direct crosslinking utilized in β -CD-PNP synthesis.

4.5. Experimental Details

4.5.1. General Methods

All starting materials and solvents were obtained from commercial suppliers and used without further purification. All polymer materials were synthesized according to procedures described in **Chapters 2 and 3**. Annealing was conducted in a tube furnace under nitrogen protection for the described time and temperature. Activated charcoal (carbon) was purchased from Sigma-Aldrich with a 100-mesh particle size for adsorption tests. Field-emission scanning electron microscopic (SEM) images were collected using a JEOL JSM-7500F FE-SEM at 5 kV. Samples were sputter coated in platinum/palladium prior to imaging. Sonication was performed using a Branson 2400 bath sonicator and a

Hielscher UP100H ultrasonic processor for probe sonication. Benzene and toluene isotherms were obtained using a Micromeritics ASAP2020 instrument at 294.15K.

4.5.2. Toluene Sorption Isotherms

Benzene and toluene sorption isotherms were collected using a Micromeritics ASAP2020 instrument at 294.15K. The mg/g adsorbed was calculated from the mmol/g isotherm data for easier comparison with the saturated vapor adsorption data and other reported data.

The toluene adsorption capacity for as-synthesized β -CD-PNP was lower than benzene demonstrating the potential selectivity, while annealed β -CD-PNPs lost the selectivity boasting higher toluene adsorption capacities (**Table 4.4**). Surprisingly, the toluene adsorption for α -CD-PNP was higher than the benzene adsorption, however, as previously mentioned caution should be taken when drawing conclusions from this α -CD-PNP data due to the potential for error. The toluene adsorption capacity of activated carbon also increased when compared with benzene, further demonstrating activated carbon's lack of selectivity.

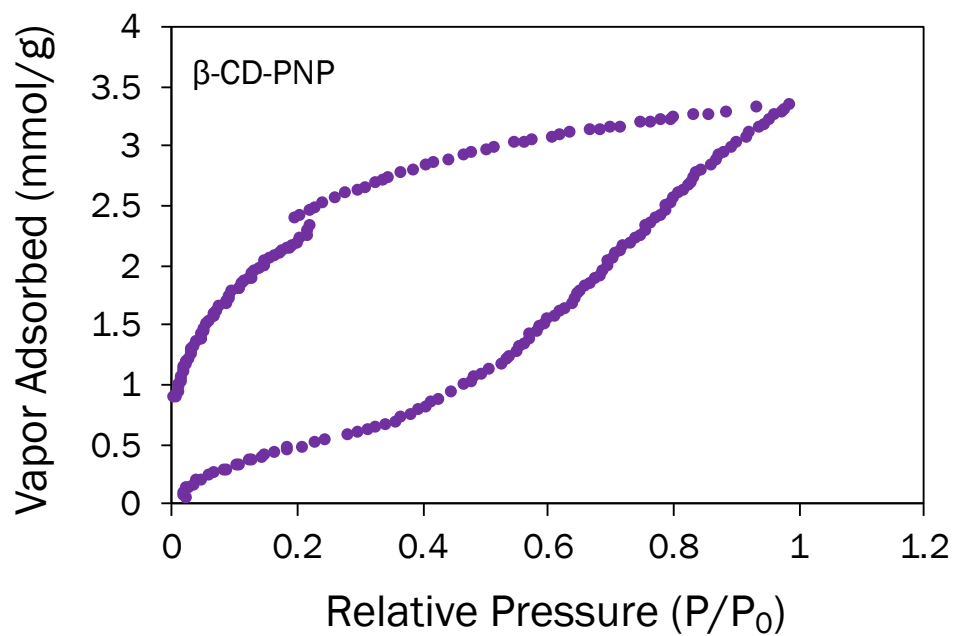


Figure 4.15. Toluene sorption isotherm for β -CD-PNP. Maximum adsorption at 3.31 mmol/g (305.0 mg/g) at 0.032 atm, 294.15 K (P = absolute pressure; P_0 = saturation pressure, \sim 0.032 atm).

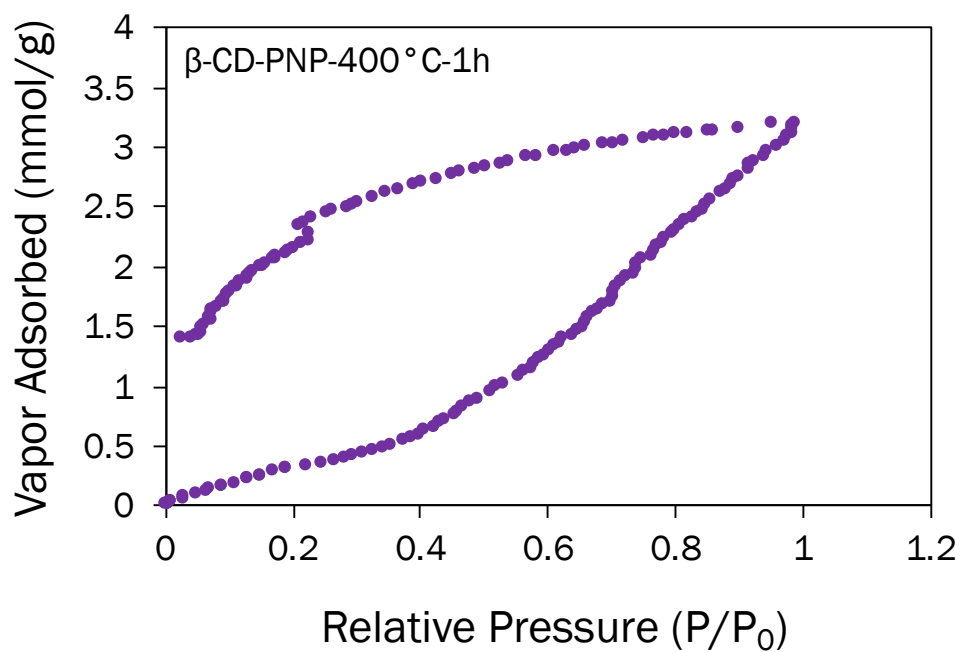


Figure 4.16. Toluene sorption isotherm for β -CD-PNP-400°C-1h (400°C = annealing temperature; 1 hour = annealing time). Maximum adsorption at 3.12 mmol/g (287.5 mg/g) at 0.032 atm, 294.15 K (P = absolute pressure; P₀ = saturation pressure, ~0.032 atm).

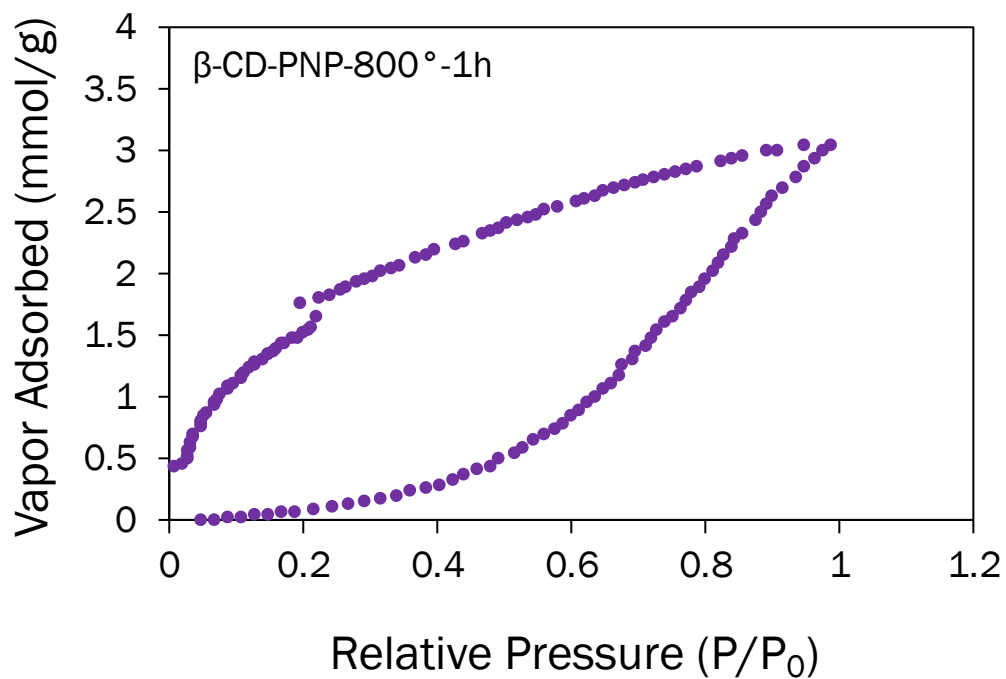


Figure 4.17. Toluene sorption isotherm for β -CD-PNP-800°C-1h (800°C = annealing temperature; 1 hour = annealing time). Maximum adsorption at 3.06 mmol/g (281.9 mg/g) at 0.032 atm, 294.15 K (P = absolute pressure; P_0 = saturation pressure, \sim 0.032 atm).

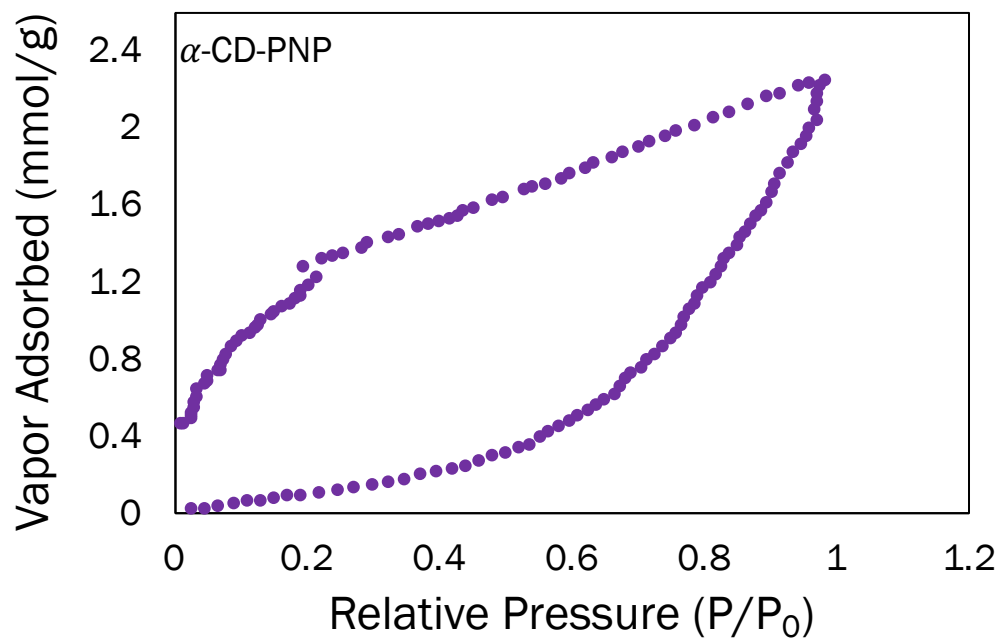


Figure 4.18. Toluene sorption isotherm for α -CD-PNP. Maximum adsorption at 2.24 mmol/g (206.4 mg/g) at 0.032 atm, 294.15 K (P = absolute pressure; P_0 = saturation pressure, ~ 0.032 atm).

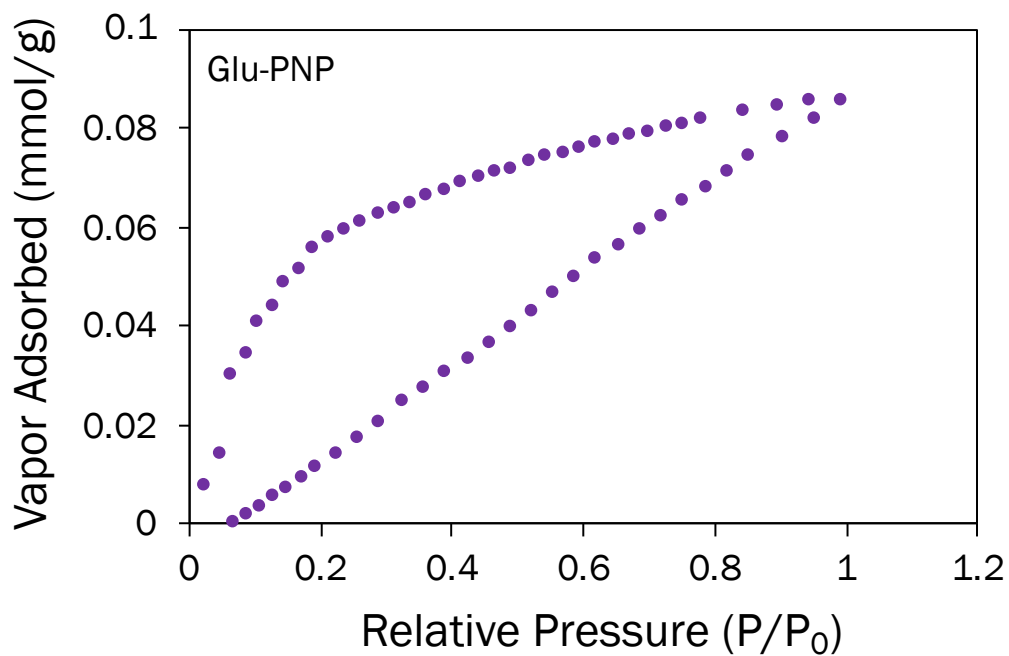


Figure 4.19. Toluene sorption isotherm for Glu-PNP. Maximum adsorption at 0.09 mmol/g (8.3 mg/g) at 0.032 atm, 294.15 K (P = absolute pressure; P₀ = saturation pressure, ~ 0.032 atm).

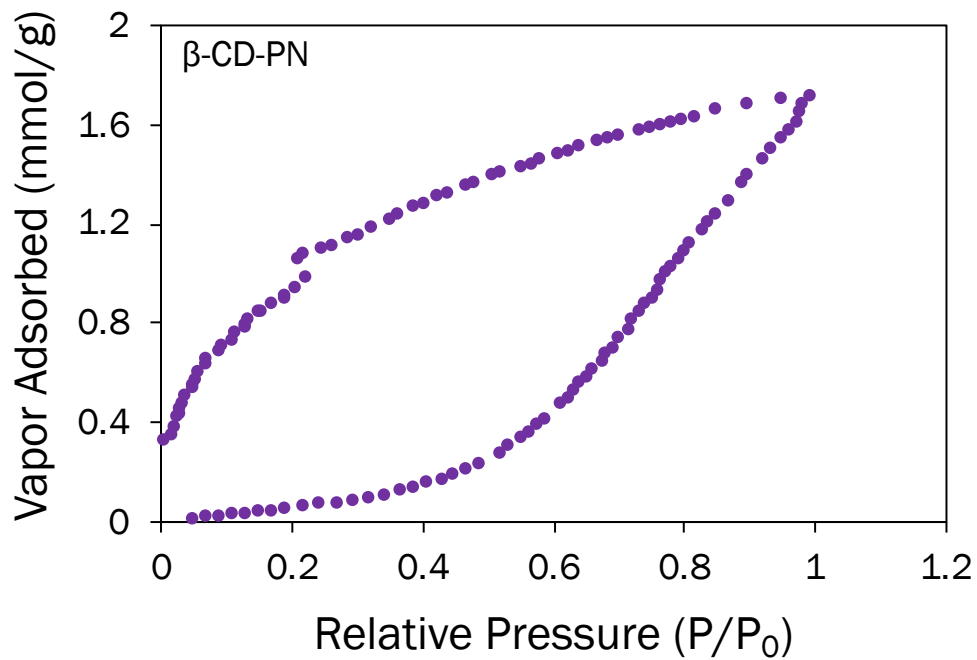


Figure 4.20. Toluene sorption isotherm for β -CD-PN. Maximum adsorption at 1.70 mmol/g (156.6 mg/g) at 0.032 atm, 294.15 K (P = absolute pressure; P_0 = saturation pressure, \sim 0.032 atm).

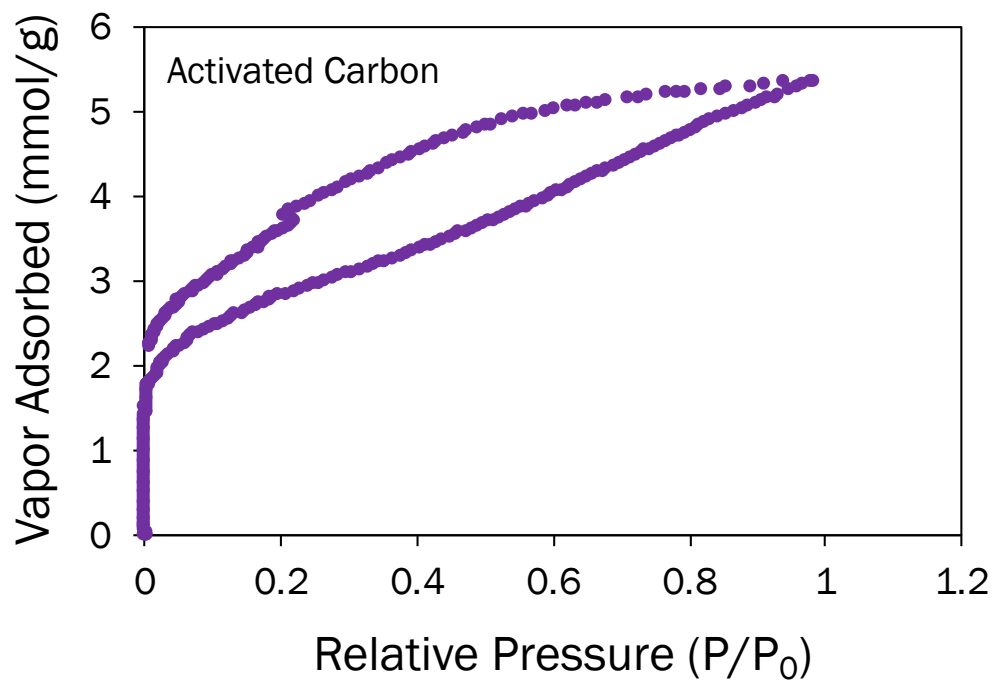


Figure 4.21 Toluene sorption isotherm for activated carbon. Maximum adsorption at 5.36 mmol/g (493.9 mg/g) at 0.032 atm, 294.15 K (P = absolute pressure; P₀ = saturation pressure, ~ 0.032 atm).

Table 4.4. Benzene and toluene adsorption capacities calculated from sorption isotherms.

Adsorbent	Benzene Capacity (mg/g)	Toluene Capacity (mg/g)
β -CD-PNP	378.1	305.0
β -CD-PNP-400°C	258.5	287.5
β -CD-PNP-800°C	200.2	281.9
β -CD-PN	57.8	156.6
α -CD-PNP	114.0	206.4
Glu-PNP	12.5	8.3
Activated Carbon	489.7	493.9

4.5.3. Saturated Vapor Adsorption

Saturated vapor adsorption measurements were collected at ambient temperature and pressure. In general, an open vial containing approximately 5 mL of the specified BTEX liquid was placed into a beaker. A pre-weighed vial containing ~ 10 mg of adsorbent was then added to the beaker as well and left open. The beaker was securely sealed with parafilm, and the system was allowed to equilibrate. After 24 h of adsorption, the adsorbent was weighed, and the gravimetric adsorption was calculated. At least, three trials were conducted and averaged together for each adsorbent with benzene, toluene, ethylbenzene, o-xylene, and m-xylene. Regeneration between trials was performed in a vacuum oven by heating at 100°C under vacuum for 12 h. Control measurements were

conducted by placing the pre-weighed vial of the adsorbent in a beaker without any BTEX and sealing in the same way. The vial was weighed after 24 h, and the weight change in mg/g was calculated. Three trials were averaged, and this value was subtracted from the BTEX adsorption measurements to control for any non-BTEX adsorption, such as humidity.

The control experiments primarily calculated the humidity adsorption contribution to the mass change. Although humidity was controlled for in each of the measurements, it is important to note the potential effects on the data. The humidity contribution for β -CD-PN was calculated to be 127.8 mg/g, while the humidity contribution for β -CD-PNP was 22.7 mg/g. With such a high humidity contribution for β -CD-PN, it is reasonable to assume there is some level of humidity interference with the BTEX adsorption. This is further highlighted when comparing the benzene adsorption capacities from the sorption isotherms and saturated adsorption data. The capacities for β -CD-PNP are well correlated at 378.1 mg/g and 393.3 mg/g for the isotherm and saturated adsorption, respectively. β -CD-PN, on the other hand, had a large disparity between the sorption isotherm (57.8 mg/g) and saturated vapor adsorption (246.8 mg/g) capacities demonstrating the potential interference of humidity on adsorption performance of the more hygroscopic β -CD-PN.

4.5.4. Sensor Fabrication

CNT Device Fabrication: Multi-walled carbon nanotubes (~6 mg) were added into N-methyl-pyrrolidone (20 mL) and bath sonicated for 40 minutes. Following bath sonication,

the solution was probe sonicated at 20% amplitude for 3 minutes. The solution was then centrifuged for 10 minutes at 3.0k rpm. 3 mL of the well-dispersed CNT solution was filtered onto a nylon membrane (13 mm diameter, 0.22 μm pore size). The film was then washed with 20 mL of ethanol and 20 mL of acetone and dried under vacuum. Silver paste electrodes were added by hand with a toothpick. The electrodes were dried at 130°C for 30 minutes.

β -CD-PNP/CNT Composite Fabrication: β -CD-PNP (14 mg) were added into acetone (20 mL) and bath sonicated for 40 minutes. The solution was then centrifuged for 10 minutes at 3.0k rpm. The 3 mL of the supernatant was added into a petri dish and a CNT film (prepared as described above) without electrodes was added into the petri dish to soak. After 15 minutes, the CNT film was removed and dried at 60°C for 10 minutes. 5 cycles of soaking and drying were completed followed by drying under vacuum. Silver electrodes were added as described above.

4.5.5. Scanning Electron Microscopy

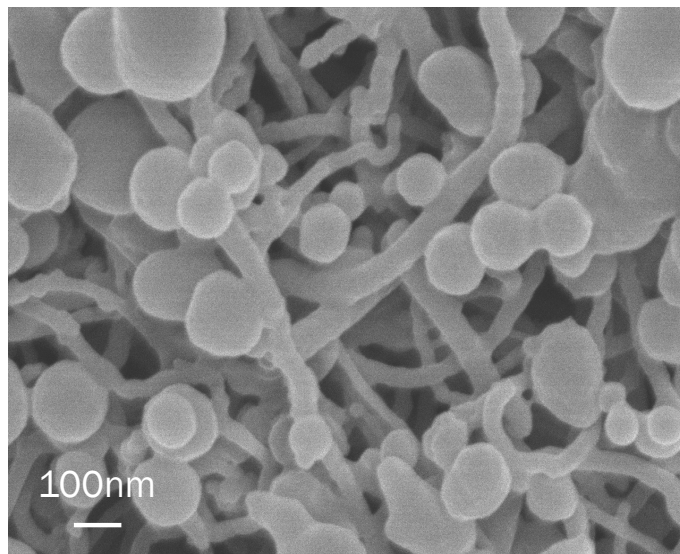


Figure 4.22. SEM image of β -CD-PNP/CNT composite demonstrating close interaction of nanoparticles and nanotubes.

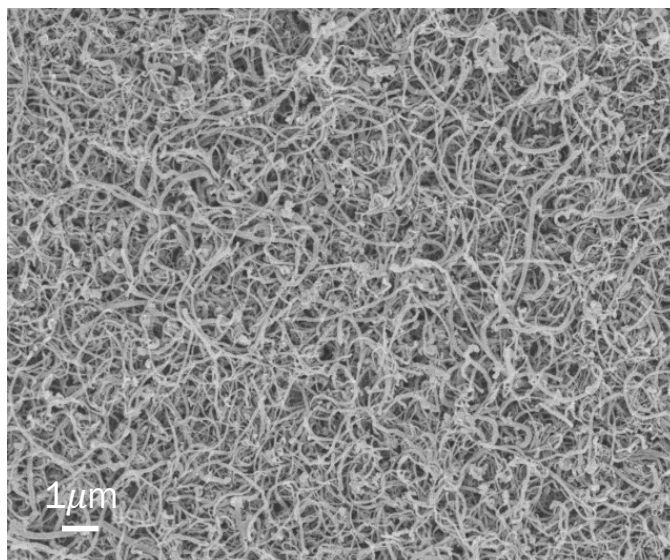


Figure 4.23. SEM images of CNT film formed via vacuum filtration.

4.5.6. Sensing Chamber Construction

The sensing setup was derived from Wei et al. (2019).¹⁸⁷ To begin building the sensing chamber as described in **Section 4.3.2** and **Figure 4.11**, tubing for gas flow was purchased from the Texas A&M University Chemistry Department stock room and Y-valves were purchased from amazon.com. A Keithley 2450 SourceMeter was used for monitoring resistance and alligator clips were used to connect the device. The wires were threaded through rubber septa and sealed to prevent gas leakage during measurements. To construct the chamber, the conical end of two 50 mL centrifuge tubes were sawed off. The sawed-off ends were connected with part of a rubber septum and epoxy followed by further sealing with PTFE tape and parafilm. Two holes were drilled into the chamber for

a gas inlet and outlet points and connections for tubing were epoxied in place. The tubing was then connected as depicted in **Figure 4.11a** to allow for control of gas flow through the valves. The vacuum was also connected to the gas outlet position. During measurements, the fume hood sash should be lowered to avoid any potential leak of toxic vapors. Additionally, the set up should be carefully examined for leaks with dry air prior to bubbling of BTEX vapors.

4.5.7. *I-V Curve Characterization*

I-V curves were measured as a two-point measurement with a Keithley 2450 Source Measure Unit under a constant flow of dry air in the sealed sensing chamber. An I-V sweep from 1 mA to 10 mA was used for all curves.

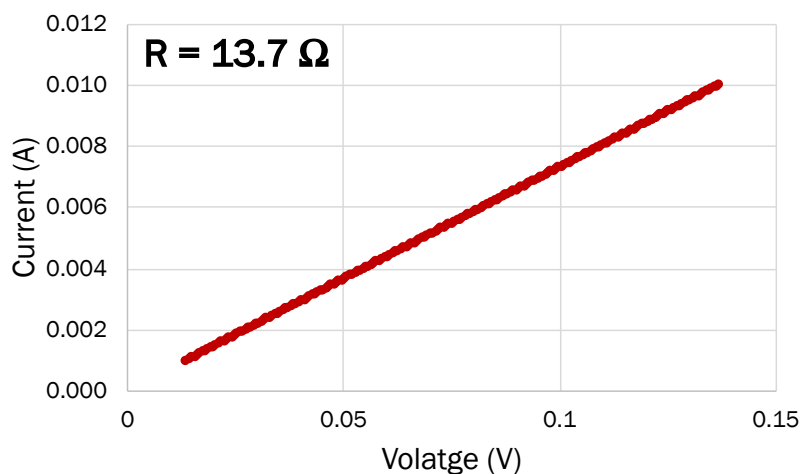


Figure 4.24. I-V curve and resistance calculation of CNT chemiresistive device.

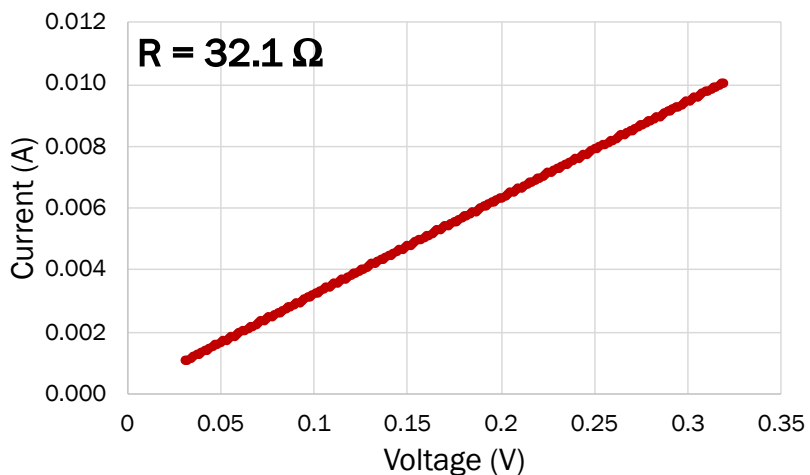


Figure 4.25. I-V curve and resistance calculation of β -CD-PNP/CNT composite device.

4.5.8. BTEX Vapor Sensing

4.5.8.1. Saturated BTEX Vapor Sensing

For the vapor sensing measurements, all BTEX vapors were measured individually. All measurements and bubbling were conducted using dry air as the carrier gas. For each measurement, a 100 s baseline measurement was taken under a constant flow of dry air prior to vapor exposure. Cyclic vapor exposure was then conducted with 50 s of vapor on and 50 s recovery time with dry air. Each measurement was run for a total of 600 s and 5 cycles. 3 trials were conducted for each vapor to ensure repeatability.

4.5.8.2. Controlled Benzene Headspace Injection Sensing

To control the amount of benzene vapor being added into the chamber, a gas-tight syringe was used to add headspace injections from a saturated benzene vial. 6 separate 10 mL vials containing 2 mL of benzene were equilibrated at 24°C for 3 h. The sensing chamber was placed under vacuum and a 200 s baseline was measured prior to benzene exposure. At 100 s, 100 μ L of air was injected as a control measurement, but no response was observed. At 200 s, 100 μ L of benzene headspace was injected into the chamber followed by 100 s recovery time. Following this injection, 80 μ L, 60 μ L, 40 μ L, 20 μ L, and 10 μ L of benzene headspace was injected with 100 s recovery times in between each injection. Each injection came from a separate vial of benzene headspace to ensure the integrity of the headspace concentration. The concentration of each injection point was calculated based on the headspace concentration, injection volume, and total chamber volume.

4.5.8.3. Limit of Detection (LOD) Calculation

The limit of detection was calculated according to literature procedures.^{175,176,188} The root-mean-squared noise (rms) deviation of the baseline was calculated prior to vapor exposure and after all vapor exposures were complete. A total of 907 and 867 data points were taken plotted for the baseline prior and after exposure, respectively. The plots were fitted with a fifth-order polynomial with Microsoft Excel. **Figure 4.26** shows an example baseline plot prior to vapor exposure. The variance ($V_{x,2}$) between the experimental data

and the fitted line was calculated according to **Equation 4.1** for both plots. In this equation, y_i is the measured response data point and y is the corresponding value from the fifth-order polynomial fit. The rms_{noise} was then calculated with **Equation 4.2**, where N is the number of data points that was used for the curve fitting. The rms_{noise} was averaged for the baseline before and after exposure to further validate the calculation. Next, the sensor response vs concentration data was plotted and fit with a power function in excel. The fit line was extrapolated towards zero. The slope of the linear portion of the fitted curve (**red line, Figure 4.27**) was used as the slope for the theoretical LOD calculation in **Equation 4.3**.

$$V_{x^2} = \sum (y_i - y)^2 \quad \text{Equation 4.1}$$

$$rms_{noise} = \sqrt{\frac{V_{x^2}}{N}} \quad \text{Equation 4.2}$$

$$LOD = \frac{3(rms_{noise})}{slope} \quad \text{Equation 4.3}$$

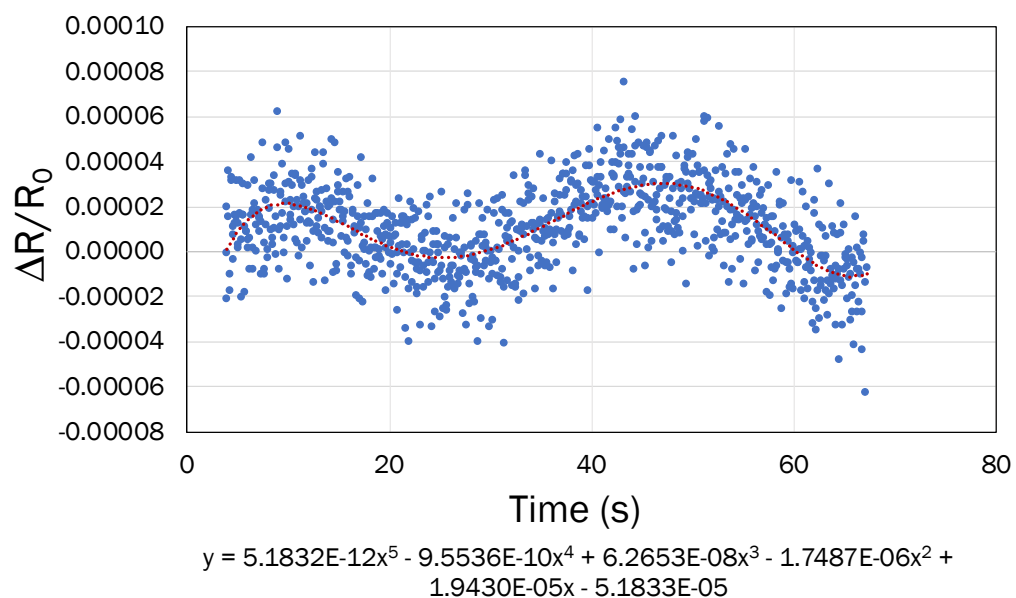


Figure 4.26. Plot of baseline measurement prior to vapor exposure fitted with fifth order polynomial.

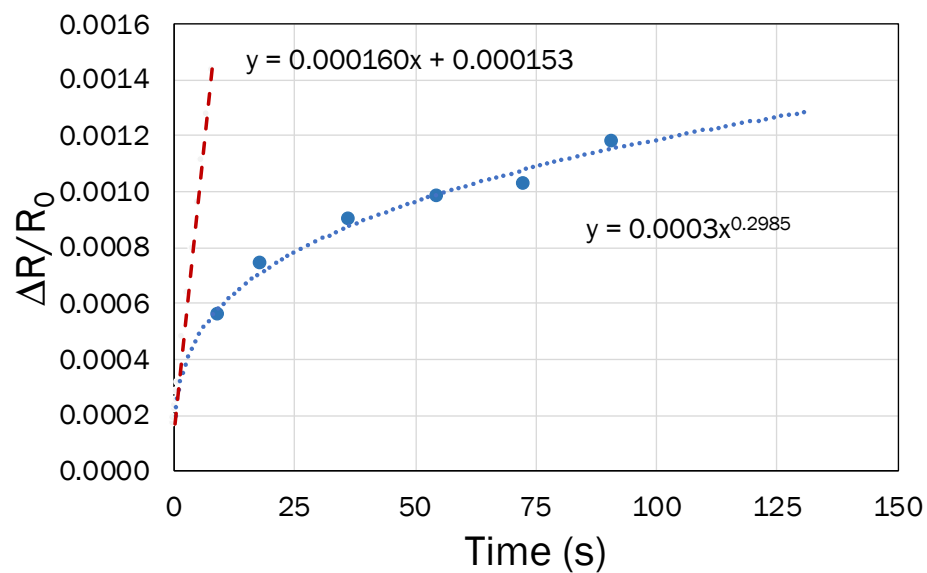


Figure 4.27. Plot of benzene concentration versus the sensor response. (Purple line = fitted power function; red line = extrapolated line from linear portion of fitted curve used to calculate LOD).

5. CONCLUSIONS

5.1. Summary

Macrocycle-derived functional materials are highly promising for adsorption-based applications. They can boast high adsorption capacities and selectivities owing to the persistent cavity inherent in macrocycles. However, the current strategies employed to synthesize these materials typically utilize toxic and expensive reagents making them unfavorable for large-scale applications.

A sustainable, scalable synthetic strategy towards cyclodextrin-derived polymer networks (CD-PN) was developed through an acid-mediated condensation reaction. MSA was utilized as both catalyst and solvent in the crosslinking reaction yielding direct ether linkages between cyclodextrin monomers. The linker-less nature of CD-PN enriched the material with a high density of macrocyclic binding sites enabling exceptional adsorption capacities of organic molecules from aqueous solutions. The persistent cavity of cyclodextrin is maintained, despite the harsh synthetic conditions, endowing CD-PN with selectivity towards analytes possessing a complementary size and shape with the cyclodextrin cavity. β -CD-PN selectively adsorbed small organic molecules from aqueous solutions, even in the presence of a large amount of interfering organic molecules. Furthermore, owing to its crosslinked nature, CD-PN was found to be highly robust upon exposure to harsh chemical environments. However, the crosslinked nature of the material also limits its further processibility and, therefore, application.

Inverse, non-aqueous emulsion polymerization was employed to control the morphology of the cyclodextrin-derived polymer networks yielding cyclodextrin-derived polymer nanoparticles (CD-PNP). The high surface area inherent in nanomaterials enhanced the accessibility of the cyclodextrin binding sites within the CD-PNPs, thus improving their overall adsorption properties. In addition, the nanoparticle morphology enabled solution processing of the insoluble, typically non-processible crosslinked CD-PN material.

The adsorption properties of CD-PNPs and CD-PNs were explored towards the vapors of benzene, toluene, ethylbenzene, and xylenes (BTEX). The importance of the nanoparticle morphology was demonstrated by the significantly higher benzene adsorption capacity of β -CD-PNP compared with bulk β -CD-PN in both isotherm and saturated vapor adsorption experiments. The adsorption selectivity of β -CD-PNP strictly follows analyte size. Smaller analytes, such as benzene, that fit more favorably into the cyclodextrin cavity were adsorbed more effectively than larger BTEX components. Overall, the adsorption capacity of β -CD-PNP was comparable to both commercial and specialized benchmark adsorption materials. However, the macrocyclic backbone of β -CD-PNP endows it with size-based selectivity that is not typically observed with commercial adsorption materials. The high adsorption capacity and enhanced selectivity of β -CD-PNP are promising for its application in BTEX sensing.

Taking advantage of the solution processibility of the nanoparticles, β -CD-PNP was incorporated into composite chemiresistor devices with carbon nanotubes as the conductive element (β -CD-PNP/CNT). The composite device performance was compared

with a bare carbon nanotube (CNT) control device. The responses of the chemiresistive devices were tested with an in-house built sensing chamber that was set up to obtain qualitative data to achieve proof of concept before moving to a more sophisticated set up.

The β -CD-PNP/CNT composite device demonstrated a scaled response to BTEX vapors following the size-based adsorption trend. The CNT control had a minimal response to each of the BTEX vapors, however no distinct trend could be observed from the responses. Although both devices demonstrated some response towards BTEX vapors, the β -CD-PNP/CNT composite device displayed significantly enhanced sensitivity to all BTEX components. The significant response enhancement enabled by β -CD-PNP is among the highest reported in the literature for BTEX sensing owing to the accessibility and high density of binding sites within the nanoparticles. A tentative limit of detection for β -CD-PNP/CNT composite device towards benzene was determined to be 279 ppb, which is within the OSHA benzene exposure limit.¹⁸⁹ Furthermore, the qualitative data obtained demonstrate the highly promising nature of β -CD-PNP in BTEX sensing.

5.2. Perspectives

5.2.1. BTEX Sensing

β -CD-PNP/CNT composite devices demonstrated promising qualitative responses towards BTEX detection. To further validate the potential of β -CD-PNP in BTEX sensing, a sophisticated sensing chamber set up is required to obtain rigorous and quantitative data. To achieve this, modifications to the current system are underway. First, a gas-tight sensing chamber has been designed and will be manufactured by the glass blowing shop

within the Texas A&M University Department of Chemistry. Second, flowmeters will be installed to precisely control the concentration of BTEX vapors being introduced into the chamber. These modifications will allow for accurate and quantitative analysis of the sensor response to BTEX vapors, which will be essential to better understand the sensing potential. Further modifications to the system to enable humidity control and mixed vapor testing would also be extremely valuable to capitalize the real-world potential of applying β -CD-PNP in sensing.

The sensing properties of α -CD-PNP should also be explored. From the adsorption data, it is expected that an α -CD-PNP/CNT composite will possess a different response pattern than the β -CD-PNP/CNT composite. If the response patterns differ enough, a sensor array could be developed to establish a “finger-print” response to complex samples that is analyzed via machine learning. If strategically designed, a highly sensitive device with the ability to detect and differentiate BTEX vapors could be developed.

5.2.2. Molecular Separation

The selective adsorption properties of β -CD-PN render it a promising stationary phase material for molecular separation. While in the presence of a high concentration of non-adsorbing molecules, β -CD-PN demonstrated the ability to selectively adsorb a low concentration of small molecules with a complementary size and shape to the cyclodextrin cavity. This property could be applied for the simple, efficient separation of components in a reaction mixture. For example, cross-coupling reactions could be simply purified using a packed column of β -CD-PN, which could theoretically adsorb the unreacted smaller molecules of the starting materials while allowing the larger molecules of the

coupling product to flow through. This method could eliminate a significant amount of solvent waste that is associated with classic column chromatography. The pharmaceutical industry utilizes many coupling reactions making it a natural target for future testing.¹⁹⁰ Representative reactions that could potentially be purified with β -CD-PN are shown in **Figure 5.1** to demonstrate the breadth of prospective applications. Niraparib is a poly (ADP-ribose) polymerase (PARP) inhibitor that is used in cancer treatments, while Lasmiditan is used for migraine treatment.^{190,191} The synthesis of Lasmiditan involves a series of coupling reactions that could potentially be purified with CD-PNs. The final coupling of Niraparib and coupling reactions 2 and 3 for Lasmiditan are viable for purification with β -CD-PN, while coupling reaction 1 for Lasmiditan seems more suited for purification with α -CD-PN.

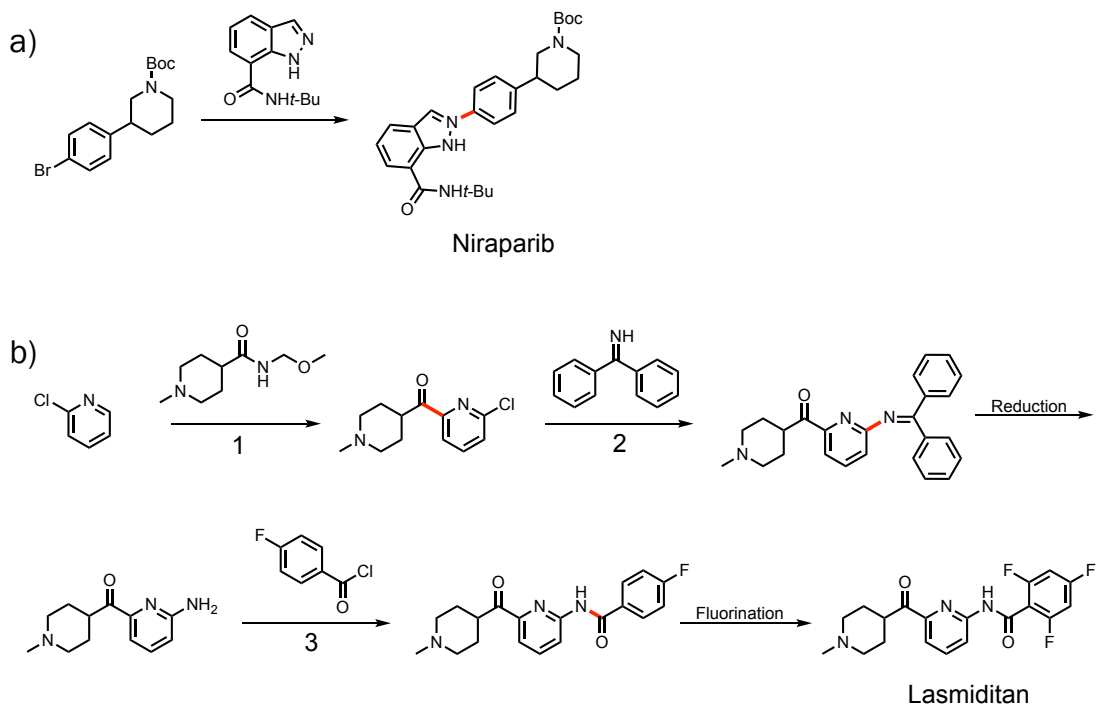


Figure 5.1. Coupling reactions utilized to synthesize a) Niraparib and b) Lasmiditan. (Coupling labels 1-3 are used for guiding the discussion; bonds formed via coupling are highlighted in red).

To realize the implementation of CD-PNs in a packed column, further tuning of the morphology is required. The development of α -/ β -CD-PNP is a step in the right direction, however the current size of the nanoparticles is too small for packing a column. With such a small particle size, the back pressure of a column would be too high. To mediate this issue, the particle size of CD-PNPs could be tuned via reformulation to synthesize microparticles. Functionalizing the current CD-PNPs onto a larger scaffold is another strategy that could be employed to achieve suitable column packing. With effective column packing, CD-PNs present a highly promising purification technique.

5.2.3. Nuclear Waste Extraction and Storage

The demand for nuclear energy has grown in recent years as the search for long-term energy solutions has evolved.¹⁹² Although nuclear energy is a promising resource, the capture and storage of radioactive nuclear waste, such as molecular and organic iodides, is a current challenge that needs to be addressed to improve the safety of nuclear energy. The volatility, radioactive nature, and harmful metabolic effects of ^{131}I make the reliable and efficient capture of ^{131}I from nuclear waste paramount.⁴⁰ However, ^{129}I needs to be efficiently captured and reliably stored afterwards owing to its particularly long half-life. The development of economical, sustainable materials for nuclear waste management is of the utmost importance for further advancement of the field. Macrocyclic materials have been utilized for the capture of radioiodine and organic iodides in both solution and vapor phases owing to their strong and specific adsorption properties.^{109,192-194} The iodide inclusion complexes of cyclodextrins have long been studied along with their potential for nuclear waste management. The binding of iodine with both α - and β -cyclodextrins is thermodynamically favorable, however the smaller cavity size of α -cyclodextrin is more favorable.¹⁹⁵ This phenomenon was partially demonstrated with the lingering rose bengal adsorption that was observed with α -CD-PN and not β -CD-PN.¹⁰² Building on this knowledge, it is reasonable that α -CD-PNP could be an excellent material for nuclear waste management. The high density of macrocyclic binding sites can enable high adsorption capacities, while the favorable binding between the α -cyclodextrin cavity and iodine could lead to prolonged storage without subsequent leaching into the environment.

Overall, the scalable, sustainable synthesis of CD-PNPs presents a promising platform for nuclear waste management.

5.2.4. Mixed Polymer Membrane Separation

Mixed matrix membranes have been widely explored for industrial gas separations. Membrane separations are an energetically favorable alternative to thermally driven separations, which currently dominate the market.¹⁹⁶ Mixed matrix membranes consist of a polymer membrane with an inorganic filler, such as metal-organic frameworks or zeolites, dispersed throughout the polymer. Typically, the polymer is chosen based on processibility and permeability, while the inorganic filler endows the mixed matrix membrane with selectivity. Although interest in mixed matrix membranes is rapidly growing, a few key challenges persist within the field: (i) interfacial incompatibility between polymers and inorganic fillers, (ii) mechanical integrity of inorganic fillers, and (iii) physical aging and plasticization of the polymer membrane.

The interfacial compatibility issues lead to particle agglomeration and voids between the inorganic particles and the polymer, which undermines selectivity. The mechanical robustness of inorganic fillers is typically lacking, so with higher particle loadings in the mixed matrix membrane, the mechanical integrity of the overall membrane suffers. Physical aging is caused by the reorganization of polymer chains to eliminate free volume, which decreases the permeability of the membrane. Plasticization, on the other hand, is caused by the swelling of the polymer matrix due to a high concentration of highly sorbing gas, which leads to increased diffusion and decreased selectivity. Higher particle loadings are favorable for enhancing the selectivity and mediating physical aging and

plasticization. However, higher particle loadings have generally been problematic in mixed matrix membranes due to the interfacial defects and mechanical integrity issues that accompany increased inorganic filler content. While several approaches have been developed to mediate these issues for mixed matrix membranes, the strategic development of mixed polymer membranes could present a new class of membrane materials that overcome these barriers.

An example mixed polymer membrane could incorporate CD-PNPs into a cellulose acetate polymer membrane, thus taking advantage of the selectivity demonstrated by CD-PNPs (**Figure 5.2**). These materials should have strong interfacial compatibility, thus preventing particle agglomeration and the formation of defects at the particle-polymer interface. The lack of interfacial defects and more robust nature of CD-PNP, when compared with inorganic materials, could also enable higher particle loadings to enhance selectivity without compromising mechanical integrity. High loading of CD-PNP in a mixed polymer membrane could also prevent physical aging and plasticization of the polymer membrane, while the crosslinked nature of CD-PNPs prevents the plasticization and physical aging of CD-PNP itself.

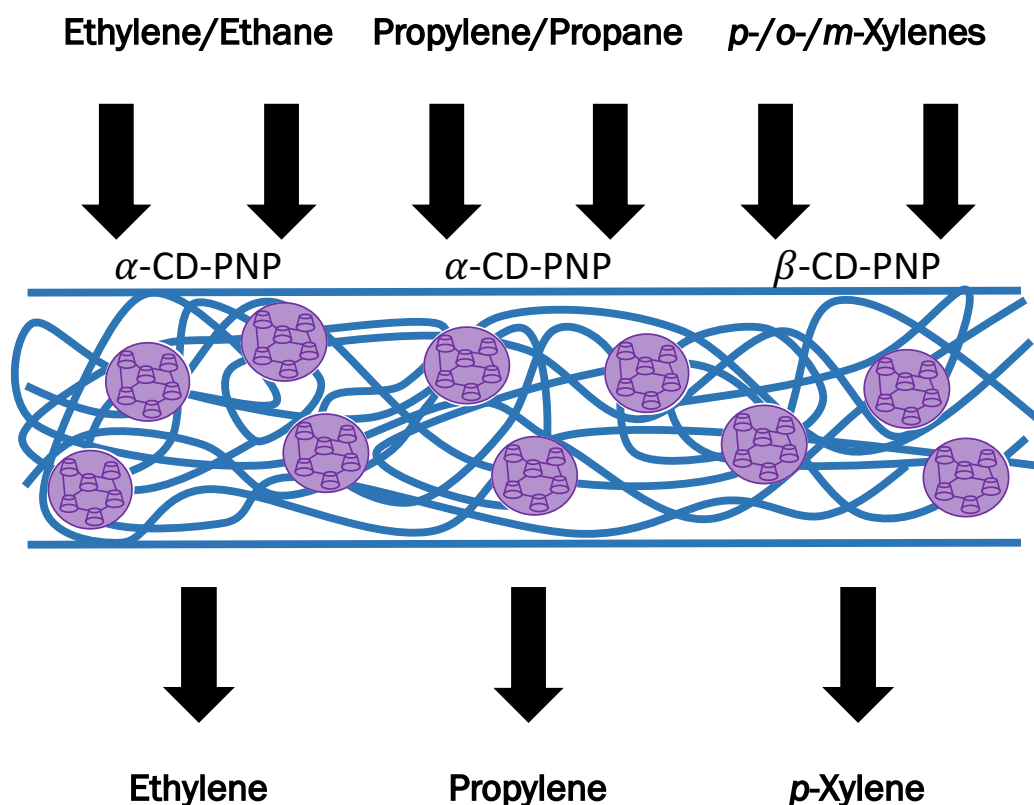


Figure 5.2. Example separations that could be achieved with CD-PNP-based mixed polymer membranes (blue represents cellulose acetate polymer membrane; purple represents CD-PNPs).

CD-PNP-based mixed polymer membranes could be applicable in a variety of separations. The cavity size of α -cyclodextrin renders α -CD-PNP-based mixed polymer membranes viable for paraffin/olefin separations, such as ethane/ethylene and propane/propylene separation (**Figure 5.2**). Ethylene and propylene are among the largest chemical feedstocks produced at the industrial scale. Thermally driven olefin/paraffin separation is estimated to consume 0.3% of global energy use, so the development of more energetically conservative separation techniques is highly desirable. β -CD-PNP-based

mixed polymer membranes, on the other hand, would be more viable for xylenes separation with *p*-xylene being a valuable raw material in the polymer industry (**Figure 5.2**). The xylene separation potential of β -cyclodextrin has been demonstrated in a variety of materials.¹⁹⁷⁻¹⁹⁹ Although the *p*-xylene adsorption of β -CD-PNP was not explicitly investigated, it is expected to be similar to toluene, so efficient separation of xylene isomers is feasible. The development of mixed polymer membranes with CD-PNP fillers presents a promising direction for future energetically conservative industrial membrane separations.

REFERENCES

1. Huang, F. H.; Anslyn, E. V., Introduction: Supramolecular Chemistry. *Chem. Rev.* **2015**, *115*, 6999-7000.
2. Anslyn, E. V.; Dougherty, D. A., *Modern physical organic chemistry*. University Science: Sausalito, CA, 2006.
3. Bonaccorso, C.; Ciadamidaro, A.; Zito, V.; Sgarlata, C.; Sciotto, D.; Arena, G., Molecular recognition of organic anions by a water-soluble calix[4]arene: Evidence for enthalpy-entropy compensation. *Thermochim. Acta.* **2012**, *530*, 107-115.
4. Atwood, J. L.; Gokel, G. W.; Barbour, L. J., *Comprehensive Supramolecular Chemistry II*. Elsevier Ltd.: Amsterdam, Netherlands, 2017; Vol. 1.
5. Mormann, W.; Hellwich, K. H., Structure-based nomenclature for cyclic organic macromolecules. *Pure. Appl. Chem.* **2008**, *80*, 201-232.
6. Pinalli, R.; Pedrini, A.; Dalcanale, E., Environmental Gas Sensing with Cavitands. *Chem.-Eur. J.* **2018**, *24*, 1010-1019.
7. Jie, K. C.; Liu, M.; Zhou, Y. J.; Little, M. A.; Bonakala, S.; Chong, S. Y.; Stephenson, A.; Chen, L. J.; Huang, F. H.; Cooper, A. I., Styrene Purification by Guest-Induced Restructuring of Pillar[6]arene. *J. Am. Chem. Soc.* **2017**, *139*, 2908-2911.
8. Wu, J. R.; Yang, Y. W., Geminiarene: Molecular Scale Dual Selectivity for Chlorobenzene and Chlorocyclohexane Fractionation. *J. Am. Chem. Soc.* **2019**, *141*, 12280-12287.
9. Zhao-Karger, Z.; Gao, P.; Ebert, T.; Klyatskaya, S.; Chen, Z.; Ruben, M.; Fichtner, M., New Organic Electrode Materials for Ultrafast Electrochemical Energy Storage. *Adv. Mater.* **2019**, *31*.
10. Adeoye, O.; Cabral-Marques, H., Cyclodextrin nanosystems in oral drug delivery: A mini review. *Int. J. Pharmaceut.* **2017**, *531*, 521-531.
11. Feng, W. W.; Jin, M.; Yang, K.; Pei, Y. X.; Pei, Z. C., Supramolecular delivery systems based on pillararenes. *Chem. Commun.* **2018**, *54*, 13626-13640.

12. Alsbaiee, A.; Smith, B. J.; Xiao, L. L.; Ling, Y. H.; Helbling, D. E.; Dichtel, W. R., Rapid removal of organic micropollutants from water by a porous beta-cyclodextrin polymer. *Nature*. **2016**, *529*, 190-U146.
13. Shetty, D.; Jahovic, J.; Raya, J.; Asfari, Z.; Olsen, J. C.; Trabolsi, A., Porous Polycalix[4]arenes for Fast and Efficient Removal of Organic Micropollutants from Water. *Acs Appl. Mater. Inter.* **2018**, *10*, 2976-2981.
14. Schonbeck, C.; Li, H.; Han, B. H.; Laursen, B. W., Solvent Effects and Driving Forces in Pillararene Inclusion Complexes. *J. Phys. Chem. B*. **2015**, *119*, 6711-6720.
15. Chen, W.; Chang, C. E.; Gilson, M. K., Calculation of cyclodextrin binding affinities: Energy, entropy, and implications for drug design. *Biophys. J.* **2004**, *87*, 3035-3049.
16. Liu, Y.; Zhao, W.; Chen, C. H.; Flood, A. H., Chloride capture using a C-H hydrogen-bonding cage. *Science*. **2019**, *365*, 159-161.
17. Phillips, B.; Banerjee, S.; Tu, X.; Fang, L., Electrical vapour sensing with macrocyclic molecular receptors. *Supramol. Chem.* **2020**, *32*, 165-177.
18. Gutsche, C. D., Calixarenes. *Acc. Chem. Res.* **1983**, *16*, 161-170.
19. Takeshita, M.; Shinkai, S., Recent Topics on Functionalization and Recognition Ability of Calixarenes - the 3rd Host Molecule. *B. Chem. Soc. Jpn.* **1995**, *68*, 1088-1097.
20. Kumar, S.; Chawla, S.; Zou, M. C., Calixarenes based materials for gas sensing applications: a review. *J. Incl. Phenom. Macro.* **2017**, *88*, 129-158.
21. Sarkar, T.; Srinives, S.; Rodriguez, A.; Mulchandani, A., Single-walled Carbon Nanotube-Calixarene Based Chemiresistor for Volatile Organic Compounds. *Electroanal.* **2018**, *30*, 2077-2084.
22. Ziganshin, M. A.; Yakimov, A. V.; Konovalov, A. I.; Antipin, I. S.; Gorbachuk, V. V., Effect of the size of calixarene macrocycle on the thermodynamic parameters of formation of inclusion compounds in guest vapor-solid host systems. *Russ. Chem. B.* **2004**, *53*, 1536-1543.

23. Murray, J.; Kim, K.; Ogoshi, T.; Yao, W.; Gibb, B. C., The aqueous supramolecular chemistry of cucurbit[n]urils, pillar[n]arenes and deep-cavity cavitands. *Chem. Soc. Rev.* **2017**, *46*, 2479-2496.
24. Moran, J. R.; Karbach, S.; Cram, D. J., Cavitands - Synthetic Molecular Vessels. *J. Am. Chem. Soc.* **1982**, *104*, 5826-5828.
25. Purse, B. W.; Rebek, J., Functional cavitands: Chemical reactivity in structured environments. *P. Natl. Acad. Sci. USA.* **2005**, *102*, 10777-10782.
26. Ogoshi, T.; Kanai, S.; Fujinami, S.; Yamagishi, T. A.; Nakamoto, Y., para-bridged symmetrical pillar[5]arenes: Their Lewis acid catalyzed synthesis and host-guest property. *J. Am. Chem. Soc.* **2008**, *130*, 5022-5023.
27. Yang, K.; Pei, Y. X.; Wen, J.; Pei, Z. C., Recent advances in pillar[n]arenes: synthesis and applications based on host-guest interactions. *Chem. Commun.* **2016**, *52*, 9316-9326.
28. Wu, J. R.; Mu, A. U.; Li, B.; Wang, C. Y.; Fang, L.; Yang, Y. W., Desymmetrized Leaning Pillar[6]arene. *Angew. Chem. Int. Ed.* **2018**, *57*, 9853-9858.
29. Bojtar, M.; Simon, A.; Bombicz, P.; Bitter, I., Expanding the Pillararene Chemistry: Synthesis and Application of a 10+1 Functionalized Pillar[5]arene. *Org. Lett.* **2017**, *19*, 4528-4531.
30. Xue, M.; Yang, Y.; Chi, X. D.; Zhang, Z. B.; Huang, F. H., Pillararenes, A New Class of Macrocycles for Supramolecular Chemistry. *Acc. Chem. Res.* **2012**, *45*, 1294-1308.
31. Barrow, S. J.; Kasera, S.; Rowland, M. J.; del Barrio, J.; Scherman, O. A., Cucurbituril-Based Molecular Recognition. *Chem. Rev.* **2015**, *115*, 12320-12406.
32. Ananthnag, G. S.; Shetti, V. S., Synthesis, structure and catalysis of organometallic porphyrin-pincer hybrids: a review. *Dalton T.* **2017**, *46*, 14062-14082.
33. Gentemann, S.; Medforth, C. J.; Forsyth, T. P.; Nurco, D. J.; Smith, K. M.; Fajer, J.; Holten, D., Photophysical Properties of Conformationally Distorted Metal-Free Porphyrins - Investigation into the Deactivation Mechanisms of the Lowest Excited Singlet-State. *J. Am. Chem. Soc.* **1994**, *116*, 7363-7368.

34. Hiroto, S.; Miyake, Y.; Shinokubo, H., Synthesis and Functionalization of Porphyrins through Organometallic Methodologies. *Chem. Rev.* **2017**, *117*, 2910-3043.
35. Liu, S. F.; Moh, L. C. H.; Swager, T. M., Single-Walled Carbon Nanotube-Metalloporphyrin Chemiresistive Gas Sensor Arrays for Volatile Organic Compounds. *Chem. Mater.* **2015**, *27*, 3560-3563.
36. Dunbar, A. D. F.; Brittle, S.; Richardson, T. H.; Hutchinson, J.; Hunter, C. A., Detection of Volatile Organic Compounds Using Porphyrin Derivatives. *J. Phys. Chem. B.* **2010**, *114*, 11697-11702.
37. Ogoshi, T.; Harada, A., Chemical sensors based on cyclodextrin derivatives. *Sens. (Basel)*. **2008**, *8*, 4961-4982.
38. Tijunelyte, I.; Dupont, N.; Milosevic, I.; Barbey, C.; Rinnert, E.; Lidgi-Guigui, N.; Guenin, E.; de la Chapelle, M. L., Investigation of aromatic hydrocarbon inclusion into cyclodextrins by Raman spectroscopy and thermal analysis. *Environ. Sci. Pollut. R.* **2017**, *24*, 27077-27089.
39. Ling, Y. H.; Klemes, M. J.; Xiao, L. L.; Alsbaiee, A.; Dichtel, W. R.; Helbling, D. E., Benchmarking Micropollutant Removal by Activated Carbon and Porous (beta-Cyclodextrin Polymers under Environmentally Relevant Scenarios. *Environ. Sci. Tech.* **2017**, *51*, 7590-7598.
40. Jie, K. C.; Zhou, Y. J.; Li, E. R.; Huang, F. H., Nonporous Adaptive Crystals of Pillararenes. *Acc. Chem. Res.* **2018**, *51*, 2064-2072.
41. Zhang, H. C.; Zou, R. Q.; Zhao, Y. L., Macrocyclic-based metal-organic frameworks. *Coordin. Chem. Rev.* **2015**, *292*, 74-90.
42. Zadmand, R.; Hokmabadi, F.; Jalali, M. R.; Akbarzadeh, A., Recent progress to construct calixarene-based polymers using covalent bonds: synthesis and applications. *Rsc Adv.* **2020**, *10*, 32690-32722.
43. Zhou, Y. J.; Jie, K. C.; Zhao, R.; Huang, F. H., Supramolecular-Macrocyclic-Based Crystalline Organic Materials. *Adv. Mater.* **2020**, *32*.
44. Crini, G., Cyclodextrin-epichlorohydrin polymers synthesis, characterization and applications to wastewater treatment: a review. *Environ. Chem. Lett.* **2021**, *19*, 2383-2403.

45. *Epichlorohydrin*; MSDS No. E1055 [Online]; Sigma-Aldrich: Darmstadt, Germany, October 2, 2020. <https://www.sigmaaldrich.com/US/en/sds/aldrich/e1055> (accessed 6/24/21).
46. *Tetrahydrofuran*; MSDS No. 401757 [Online]; Sigma-Aldrich: Darmstadt, Germany, June 1, 2021. <https://www.sigmaaldrich.com/US/en/sds/sial/401757> (accessed 6/24/21).
47. *Tetrafluoroterephthalonitrile*; MSDS No. 104426 [Online]; Sigma-Aldrich: Darmstadt, Germany, September 18, 2019. <https://www.sigmaaldrich.com/US/en/sds/aldrich/104426> (accessed 6/24/21).
48. Shetty, D.; Jahovic, I.; Raya, J.; Ravaux, F.; Jouiad, M.; Olsen, J. C.; Trabolsi, A., An ultra-absorbent alkyne-rich porous covalent polycalix[4]arene for water purification. *J. Mater. Chem. A*. **2017**, *5*, 62-66.
49. Jiang, L. G.; Cao, S. Q.; Cheung, P. P. H.; Zheng, X. Y.; Leung, C. W. T.; Peng, Q.; Shuai, Z. G.; Tang, B. Z.; Yao, S. H.; Huang, X. H., Real-time monitoring of hydrophobic aggregation reveals a critical role of cooperativity in hydrophobic effect. *Nat. Commun.* **2017**, *8*.
50. Klemes, M. J.; Ling, Y. H.; Chiapasco, M.; Alsaiee, A.; Helbling, D. E.; Dichtel, W. R., Phenolation of cyclodextrin polymers controls their lead and organic micropollutant adsorption. *Chem. Sci.* **2018**, *9*, 8883-8889.
51. Pan, J. X.; Li, S. M.; Dang, F. Q.; Zhang, Z. Q.; Zhang, J., Fabrication of a porous beta-cyclodextrin-polymer-coated solid-phase microextraction fiber for the simultaneous determination of five contaminants in water using gas chromatography-mass spectrometry. *Rsc Adv.* **2018**, *8*, 22422-22428.
52. Xu, G. Z.; Xie, X. C.; Qin, L.; Hu, X. J.; Zhang, D. L.; Xu, J.; Li, D. W.; Ji, X. W.; Huang, Y.; Tu, Y. Z.; Jiang, L.; Wei, D. Y., Simple synthesis of a swellable porous beta-cyclodextrin-based polymer in the aqueous phase for the rapid removal of organic micro-pollutants from water. *Green Chem.* **2019**, *21*, 6062-6072.
53. Shi, B. B.; Guan, H. X.; Shangguan, L. Q.; Wang, H.; Xia, D. Y.; Kong, X. Q.; Huang, F. H., A pillar[5]arene-based 3D network polymer for rapid removal of organic micropollutants from water. *J. Mater. Chem. A*. **2017**, *5*, 24217-24222.

54. Lu, P. P.; Cheng, J. C.; Li, Y. F.; Li, L.; Wang, Q.; He, C. Y., Novel porous beta-cyclodextrin/pillar[5]arene copolymer for rapid removal of organic pollutants from water. *Carbohydr. Polym.* **2019**, *216*, 149-156.
55. Cataldo, S.; Lo Meo, P.; Conte, P.; Di Vincenzo, A.; Milea, D.; Pettignano, A., Evaluation of adsorption ability of cyclodextrin-calixarene nanosponges towards Pb(2+) ion in aqueous solution. *Carbohydr. Polym.* **2021**, *267*, 118151.
56. Tian, B. R.; Hua, S. Y.; Tian, Y.; Liu, J. Y., Cyclodextrin-based adsorbents for the removal of pollutants from wastewater: a review. *Environ. Sci. Pollut. R.* **2021**, *28*, 1317-1340.
57. Liu, Q. M.; Zhou, Y.; Lu, J.; Zhou, Y. B., Novel cyclodextrin-based adsorbents for removing pollutants from wastewater: A critical review. *Chemosphere.* **2020**, *241*.
58. Abubakar, S.; Skorjanc, T.; Shetty, D.; Trabolsi, A., Porous Polycalix[n]arenes as Environmental Pollutant Removers. *ACS Appl. Mater. Inter.* **2021**, *13*, 14802-14815.
59. Pinalli, R.; Pedrini, A.; Dalcanale, E., Biochemical sensing with macrocyclic receptors. *Chem. Soc. Rev.* **2018**, *47*, 7006-7026.
60. Niu, X. H.; Mo, Z. L.; Yang, X.; Sun, M. Y.; Zhao, P.; Li, Z. L.; Ouyang, M. X.; Liu, Z. Y.; Gao, H. H.; Guo, R. B.; Liu, N. J., Advances in the use of functional composites of beta-cyclodextrin in electrochemical sensors. *Microchimica Acta.* **2018**, *185*.
61. Kumar, R.; Sharma, A.; Singh, H.; Suating, P.; Kim, H. S.; Sunwoo, K.; Shim, I.; Gibb, B. C.; Kim, J. S., Revisiting Fluorescent Calixarenes: From Molecular Sensors to Smart Materials. *Chem. Rev.* **2019**, *119*, 9657-9721.
62. Zhang, H. C.; Han, J.; Li, C., Pillararene-based conjugated porous polymers. *Polym. Chem. (Uk).* **2021**, *12*, 2808-2824.
63. Tan, L. L.; Li, H. W.; Tao, Y. C.; Zhang, S. X. A.; Wang, B.; Yang, Y. W., Pillar[5]arene-Based Supramolecular Organic Frameworks for Highly Selective CO₂-Capture at Ambient Conditions. *Adv. Mater.* **2014**, *26*, 7027-7031.
64. Li, E.; Zhou, Y.; Zhao, R.; Jie, K.; Huang, F., Dihalobenzene Shape Sorting by Nonporous Adaptive Crystals of Perbromoethylated Pillararenes. *Angew. Chem. Int. Ed.* **2019**, *58*, 3981-3985.

65. Jie, K. C.; Liu, M.; Zhou, Y. J.; Little, M. A.; Pulido, A.; Chong, S. Y.; Stephenson, A.; Hughes, A. R.; Sakakibara, F.; Ogoshi, T.; Blanc, F.; Day, G. M.; Huang, F. H.; Cooper, A. I., Near-Ideal Xylene Selectivity in Adaptive Molecular Pillar[n]arene Crystals. *J. Am. Chem. Soc.* **2018**, *140*, 6921-6930.
66. Chen, L.; Zhu, D. D.; Ji, G. J.; Yuan, S.; Qian, J. F.; He, M. Y.; Chen, Q.; Zhang, Z. H., Efficient adsorption separation of xylene isomers using a facilely fabricated cyclodextrin-based metal-organic framework. *J. Chem. Technol. Biot.* **2018**, *93*, 2898-2905.
67. Moosa, B.; Alimi, L. O.; Shkurenko, A.; Fakim, A.; Bhatt, P. M.; Zhang, G. W.; Eddaoudi, M.; Khashab, N. M., A Polymorphic Azobenzene Cage for Energy-Efficient and Highly Selective p-Xylene Separation. *Angew. Chem. Int. Ed.* **2020**, *59*, 21367-21371.
68. Sun, N.; Wang, S. Q.; Zou, R. Q.; Cui, W. G.; Zhang, A. Q.; Zhang, T. Z.; Li, Q.; Zhuang, Z. Z.; Zhang, Y. H.; Xu, J. L.; Zaworotko, M. J.; Bu, X. H., Benchmark selectivity p-xylene separation by a non-porous molecular solid through liquid or vapor extraction. *Chem. Sci.* **2019**, *10*, 8850-8854.
69. Wang, F.; Yang, Y.; Swager, T. M., Molecular Recognition for High Selectivity in Carbon Nanotube/Polythiophene Chemiresistors. *Angew. Chem. Int. Ed.* **2008**, *47*, 8394-8396.
70. Bew, S. P.; Burrows, A. D.; Duren, T.; Mahon, M. F.; Moghadam, P. Z.; Sebestyen, V. M.; Thurston, S., Calix[4]arene-based metal-organic frameworks: towards hierarchically porous materials. *Chem. Commun.* **2012**, *48*, 4824-4826.
71. Schulz, M.; Gehl, A.; Schlenkrich, J.; Schulze, H. A.; Zimmermann, S.; Schaate, A., A Calixarene-Based Metal-Organic Framework for Highly Selective NO₂ Detection. *Angew. Chem. Int. Ed.* **2018**, *57*, 12961-12965.
72. Talapaneni, S. N.; Kim, D.; Barin, G.; Buyukcakir, O.; Je, S. H.; Coskun, A., Pillar[5]arene Based Conjugated Microporous Polymers for Propane/Methane Separation through Host-Guest Complexation. *Chem. Mater.* **2016**, *28*, 4460-4466.
73. Alzate-Sanchez, D. M.; Smith, B. J.; Alsbaiee, A.; Hinstroza, J. P.; Dichtel, W. R., Cotton Fabric Functionalized with a beta-Cyclodextrin Polymer Captures Organic Pollutants from Contaminated Air and Water. *Chem. Mater.* **2016**, *28*, 8340-8346.

74. Wu, J. R.; Yang, Y. W., Synthetic Macrocyclic-Based Nonporous Adaptive Crystals for Molecular Separation. *Angew. Chem. Int. Ed.* **2021**, *60*, 1690-1701.
75. Morohashi, N.; Hattori, T., Selective guest inclusion by crystals of calixarenes: potential for application as separation materials. *J. Incl. Phenom. Macro.* **2018**, *90*, 261-277.
76. Rajkumar, T.; Kukkar, D.; Kim, K. H.; Sohn, J. R.; Deep, A., Cyclodextrin-metal-organic framework (CD-MOF): From synthesis to for applications. *J. Ind. Eng. Chem.* **2019**, *72*, 50-66.
77. Wang, T.; Huang, D.; Yang, Z.; Xu, S. S.; He, G. L.; Li, X. L.; Hu, N. T.; Yin, G. L.; He, D. N.; Zhang, L. Y., A Review on Graphene-Based Gas/Vapor Sensors with Unique Properties and Potential Applications. *Nano-Micro. Lett.* **2016**, *8*, 95-119.
78. Afzal, A.; Iqbal, N.; Mujahid, A.; Schirhagl, R., Advanced vapor recognition materials for selective and fast responsive surface acoustic wave sensors: A review. *Anal. Chim. Acta.* **2013**, *787*, 36-49.
79. Acikbas, Y.; Bozkurt, S.; Erdogan, M.; Halay, E.; Sirit, A.; Capan, R., Optical and Vapor Sensing Properties of Calix[4]arene Langmuir-Blodgett Thin Films with Host-Guest Principles. *J. Macromol. Sci. A.* **2018**, *55*, 526-532.
80. Halay, E.; Acikbas, Y.; Capan, R.; Bozkurt, S.; Erdogan, M.; Unal, R., A novel triazine-bearing calix[4]arene: Design, synthesis and gas sensing affinity for volatile organic compounds. *Tetrahedron.* **2019**, *75*, 2521-2528.
81. Zeng, W.; Zhang, M. Q.; Rong, M. Z.; Zheng, Q., Conductive polymer composites as gas sensors with size-related molecular discrimination capability. *Sens. Actuat. B-Chem.* **2007**, *124*, 118-126.
82. Liu, Y.; Wang, K. R.; Guo, D. S.; Jiang, B. P., Supramolecular Assembly of Perylene Bisimide with beta-Cyclodextrin Grafts as a Solid-State Fluorescence Sensor for Vapor Detection. *Adv. Funct. Mater.* **2009**, *19*, 2230-2235.
83. Lai, C. S. I.; Moody, G. J.; Thomas, J. D. R.; Mulligan, D. C.; Stoddart, J. F.; Zarzycki, R., Piezoelectric Quartz Crystal Detection of Benzene Vapor Using Chemically Modified Cyclodextrins. *J. Chem. Soc. Perkin. Trans. 2.* **1988**, 319-324.

84. Kursunlu, A. N.; Acikbas, Y.; Ozmen, M.; Erdogan, M.; Capan, R., Preparation of pillar[5] arene-quinoline Langmuir-Blodgett thin films for detection of volatile organic compounds with host-guest principles. *Analyst*. **2017**, *142*, 3689-3698.
85. Vashist, S. K.; Vashist, P., Recent Advances in Quartz Crystal Microbalance-Based Sensors. *J. Sensors*. **2011**, *2011*.
86. Sun, X. C.; Wang, Y.; Lei, Y., Fluorescence based explosive detection: from mechanisms to sensory materials. *Chem. Soc. Rev*. **2015**, *44*, 8019-8061.
87. Boonkitpatarakul, K.; Yodta, Y.; Niamnont, N.; Sukwattanasinitt, M., Fluorescent phenylethynylene calix[4]arenes for sensing TNT in aqueous media and vapor phase. *Rsc Adv*. **2015**, *5*, 33306-33311.
88. Barata, P. D.; Prata, J. V., Fluorescent Calix[4]arene-Carbazole-Containing Polymers as Sensors for Nitroaromatic Explosives. *Chemosensors*. **2020**, *8*.
89. Zhu, C. Z.; Fang, L., Mingling Electronic Chemical Sensors with Supramolecular Host-Guest Chemistry. *Curr. Org. Chem*. **2014**, *18*, 1957-1964.
90. Sokolov, A. N.; Roberts, M. E.; Johnson, O. B.; Cao, Y. D.; Bao, Z. A., Induced Sensitivity and Selectivity in Thin-Film Transistor Sensors via Calixarene Layers. *Adv. Mater*. **2010**, *22*, 2349-2353.
91. Acikbas, Y.; Aksoy, M.; Aksoy, M.; Karaagac, D.; Bastug, E.; Kursunlu, A. N.; Erdogan, M.; Capan, R.; Ozmen, M.; Ersoz, M., Recent progress in pillar[n]arene-based thin films on chemical sensor applications. *J. Incl. Phenom. Macro*. **2021**, *100*, 39-54.
92. McGinn, C. K.; Lamport, Z. A.; Kymissis, I., Review of Gravimetric Sensing of Volatile Organic Compounds. *Acs Sens*. **2020**, *5*, 1514-1534.
93. Li, X.; Li, Z.; Yang, Y. W., Tetraphenylethylene-Interweaving Conjugated Macrocyclic Polymer Materials as Two-Photon Fluorescence Sensors for Metal Ions and Organic Molecules. *Adv. Mater*. **2018**, *30*.
94. Julien, P. A.; Mottillo, C.; Friscic, T., Metal-organic frameworks meet scalable and sustainable synthesis. *Green Chem*. **2017**, *19*, 2729-2747.
95. Ayoub, A. S.; Rizvi, S. S. H., An Overview on the Technology of Cross-Linking of Starch for Nonfood Applications. *J. Plast. Film. Sheet*. **2009**, *25*, 25-45.

96. Guo, Z. H.; Wang, C. X.; Zhang, Q.; Che, S.; Zhou, H. C.; Fang, L., Cost-effective synthesis and solution processing of porous polymer networks through methanesulfonic acid-mediated aldol triple condensation. *Materials Chemistry Frontiers*. **2018**, *2*, 396-401.
97. Huang, J.; Turner, S. R., Hypercrosslinked Polymers: A Review. *Polym. Rev.* **2018**, *58*, 1-41.
98. Biwer, A.; Antranikian, G.; Heinzle, E., Enzymatic production of cyclodextrins. *Appl. Microbiol. Biot.* **2002**, *59*, 609-617.
99. Szejtli, J., Past, present, and future of cyclodextrin research. *Pure. Appl. Chem.* **2004**, *76*, 1825-1845.
100. Palden, T.; Onghena, B.; Regadio, M.; Binnemans, K., Methanesulfonic acid: a sustainable acidic solvent for recovering metals from the jarosite residue of the zinc industry. *Green Chem.* **2019**, *21*, 5394-5404.
101. Zou, Y.; Yuan, T. Y.; Yao, H. Q.; Frazier, D. J.; Stanton, D. J.; Sue, H. J.; Fang, L., Solution-Processable Core-Extended Quinacridone Derivatives with Intact Hydrogen Bonds. *Org. Lett.* **2015**, *17*, 3146-3149.
102. Phillips, B.; Wang, C.; Tu, X.; Chang, C. H.; Banerjee, S.; Al-Hashimi, M.; Hu, W.; Fang, L., Cyclodextrin-derived polymer networks for selective molecular adsorption. *Chem. Commun.* **2020**, *56*, 11783-11786.
103. Feng, S. T.; Bagia, C.; Mpourmpakis, G., Determination of Proton Affinities and Acidity Constants of Sugars. *J. Phys. Chem. A.* **2013**, *117*, 5211-5219.
104. Dee, S. J.; Bell, A. T., A Study of the Acid-Catalyzed Hydrolysis of Cellulose Dissolved in Ionic Liquids and the Factors Influencing the Dehydration of Glucose and the Formation of Humins. *Chemsuschem.* **2011**, *4*, 1166-1173.
105. Wang, C. X.; Li, C. X.; Rutledge, E. R. C.; Che, S.; Lee, J.; Kalin, A. J.; Zhang, C. L.; Zhou, H. C.; Guo, Z. H.; Fang, L., Aromatic porous polymer network membranes for organic solvent nanofiltration under extreme conditions. *J. Mater. Chem. A.* **2020**, *8*, 15891-15899.
106. Crini, G.; Fourmentin, S.; Fenyvesi, E.; Torri, G.; Fourmentin, M.; Morin-Crini, N., Fundamentals and Applications of Cyclodextrins. *Cyclodextrin Fundamentals, Reactivity and Analysis.* **2018**, 1-55.

107. Ali, I.; Asim, M.; Khan, T. A., Low cost adsorbents for the removal of organic pollutants from wastewater. *J. Environ. Manage.* **2012**, *113*, 170-183.
108. Menya, E.; Olupot, P. W.; Storz, H.; Lubwama, M.; Kiros, Y., Production and performance of activated carbon from rice husks for removal of natural organic matter from water: A review. *Chem. Eng. Res. Des.* **2018**, *129*, 271-296.
109. Szente, L.; Fenyvesi, E.; Szejtli, J., Entrapment of iodine with cyclodextrins: Potential application of cyclodextrins in nuclear waste management. *Environ. Sci. Tech.* **1999**, *33*, 4495-4498.
110. Haller, J.; Kaatze, U., On the complexation of alpha-cyclodextrin in iodide and iodide-iodine aqueous solutions. *J. Mol. Liq.* **2008**, *138*, 34-39.
111. Do, D. D.; Do, H. D., Effects of adsorbate-adsorbate interaction in the description of adsorption isotherm of hydrocarbons in micro-mesoporous carbonaceous materials. *Appl. Surf. Sci.* **2002**, *196*, 13-29.
112. Umpleby, R. J.; Baxter, S. C.; Chen, Y.; Shah, R. N.; Shimizu, K. D., Characterization of Molecularly Imprinted Polymers with the Langmuir-Freundlich Isotherm. *Anal. Chem.* **2001**, *73*, 4584-4591.
113. Yu, T. T.; Xue, Z. M.; Zhao, X. H.; Chen, W. J.; Mu, T. C., Green synthesis of porous beta-cyclodextrin polymers for rapid and efficient removal of organic pollutants and heavy metal ions from water. *New J. Chem.* **2018**, *42*, 16154-16161.
114. Wang, R. Q.; Wei, X. B.; Feng, Y. Q., beta-Cyclodextrin Covalent Organic Framework for Selective Molecular Adsorption. *Chem.-Eur. J.* **2018**, *24*, 10979-10983.
115. Morin-Crini, N.; Crini, G., Environmental applications of water-insoluble beta-cyclodextrin-epichlorohydrin polymers. *Prog. Polym. Sci.* **2013**, *38*, 344-368.
116. Kono, H.; Nakamura, T.; Hashimoto, H.; Shimizu, Y., Characterization, molecular dynamics, and encapsulation ability of beta-cyclodextrin polymers crosslinked by polyethylene glycol. *Carbohydr. Polym.* **2015**, *128*, 11-23.
117. Wang, Z. H.; Zhang, P. B.; Hu, F.; Zhao, Y. F.; Zhu, L. P., A crosslinked beta-cyclodextrin polymer used for rapid removal of a broad-spectrum of organic micropollutants from water. *Carbohydr. Polym.* **2017**, *177*, 224-231.

118. Zhou, Y. B.; Hu, Y. H.; Huang, W. W.; Cheng, G.; Cui, C. Z.; Lu, J., A novel amphoteric beta-cyclodextrin-based adsorbent for simultaneous removal of cationic/anionic dyes and bisphenol A. *Chem. Eng. J.* **2018**, *341*, 47-57.
119. Xiao, L. L.; Ling, Y. H.; Alsaiee, A.; Li, C. J.; Helbling, D. E.; Dichtel, W. R., beta-Cyclodextrin Polymer Network Sequesters Perfluorooctanoic Acid at Environmentally Relevant Concentrations (vol 139, pg 7689, 2017). *J. Am. Chem. Soc.* **2017**, *139*, 10585-10585.
120. Li, Y. R.; Lu, P. P.; Cheng, J. C.; Zhu, X. L.; Guo, W.; Liu, L. J.; Wang, Q.; He, C. Y.; Liu, S. R., Novel microporous beta-cyclodextrin polymer as sorbent for solid-phase extraction of bisphenols in water samples and orange juice. *Talanta.* **2018**, *187*, 207-215.
121. Wang, J.; Harrison, M., Removal of organic micro-pollutants from water by β -cyclodextrin triazine polymers. *J. Incl. Phenom. Macro.* **2018**, *92*, 347-356.
122. Alzate-Sanchez, D. M.; Ling, Y. H.; Li, C. J.; Frank, B. P.; Bleher, R.; Fairbrother, D. H.; Helbling, D. E.; Dichtel, W. R., beta-Cyclodextrin Polymers on Microcrystalline Cellulose as a Granular Media for Organic Micropollutant Removal from Water. *Acs Appl. Mater. Inter.* **2019**, *11*, 8089-8096.
123. Schiffman, J. D.; Schauer, C. L., One-step electrospinning of cross-linked chitosan fibers. *Biomacromolecules.* **2007**, *8*, 2665-2667.
124. Kishan, A. P.; Nezarati, R. M.; Radzicki, C. M.; Renfro, A. L.; Robinson, J. L.; Whitely, M. E.; Cosgriff-Hernandez, E. M., In situ crosslinking of electrospun gelatin for improved fiber morphology retention and tunable degradation (vol 3, pg 7930, 2015). *J. Mater. Chem. B.* **2015**, *3*, 8212-8212.
125. Liu, S. Q.; Chen, D. R.; Zheng, J.; Zeng, L. W.; Jiang, J. J.; Jiang, R. F.; Zhu, F.; Shen, Y.; Wu, D. C.; Ouyang, G. F., The sensitive and selective adsorption of aromatic compounds with highly crosslinked polymer nanoparticles. *Nanoscale.* **2015**, *7*, 16943-16951.
126. Rao, J. P.; Geckeler, K. E., Polymer nanoparticles: Preparation techniques and size-control parameters. *Prog. Polym. Sci.* **2011**, *36*, 887-913.
127. Khan, I.; Saeed, K.; Khan, I., Nanoparticles: Properties, applications and toxicities. *Arab. J. Chem.* **2019**, *12*, 908-931.

128. Santhosh, C.; Velmurugan, V.; Jacob, G.; Jeong, S. K.; Grace, A. N.; Bhatnagar, A., Role of nanomaterials in water treatment applications: A review. *Chem. Eng. J.* **2016**, *306*, 1116-1137.
129. Mallakpour, S.; Behranvand, V., Polymeric nanoparticles: Recent development in synthesis and application. *Express Polym. Lett.* **2016**, *10*, 895-913.
130. Wackerlig, J.; Schirhagl, R., Applications of Molecularly Imprinted Polymer Nanoparticles and Their Advances toward Industrial Use: A Review. *Anal. Chem.* **2016**, *88*, 250-261.
131. Hussain, M.; Kotova, K.; Lieberzeit, P. A., Molecularly Imprinted Polymer Nanoparticles for Formaldehyde Sensing with QCM. *Sens. (Basel)*. **2016**, *16*.
132. McClements, D. J., Nanoemulsions versus microemulsions: terminology, differences, and similarities. *Soft Matter*. **2012**, *8*, 1719-1729.
133. Chern, C. S., *Principles and Applications of Emulsion Polymerization*. Wiley: 2008.
134. Slomkowski, S.; Aleman, J. V.; Gilbert, R. G.; Hess, M.; Horie, K.; Jones, R. G.; Kubisa, P.; Meisel, I.; Mormann, W.; Penczek, S.; Stepto, R. F. T., Terminology of polymers and polymerization processes in dispersed systems (IUPAC Recommendations 2011). *Pure. Appl. Chem.* **2011**, *83*, 2229-2259.
135. Nagarajan, R., Molecular packing parameter and surfactant self-assembly: The neglected role of the surfactant tail. *Langmuir*. **2002**, *18*, 31-38.
136. Lombardo, D.; Kiselev, M. A.; Magazu, S.; Calandra, P., Amphiphiles Self-Assembly: Basic Concepts and Future Perspectives of Supramolecular Approaches. *Adv. Cond. Matter. Phys.* **2015**, *2015*.
137. Roitman, D. B.; Mcalister, J.; Oaks, F. L., Composition Characterization of Methanesulfonic-Acid. *J. Chem. Eng. Data.* **1994**, *39*, 56-60.
138. Sachin, K. M.; Karpe, S. A.; Singh, M.; Bhattarai, A., Self-assembly of sodium dodecylsulfate and dodecyltrimethylammonium bromide mixed surfactants with dyes in aqueous mixtures. *Roy. Soc. Open Sci.* **2019**, *6*.

139. Sohrabi, B.; Gharibi, H.; Tajik, B.; Javadian, S.; Hashemianzadeh, M., Molecular Interactions of Cationic and Anionic Surfactants in Mixed Monolayers and Aggregates. *J. Phys. Chem. B.* **2008**, *112*, 14869-14876.
140. Oprea, S.; Dodita, T., Influence of agitation during emulsion polymerization of acrylic-styrene latexes on end product properties. *Prog. Org. Coat.* **2001**, *42*, 194-201.
141. Slominska, M.; Krol, S.; Namiesnik, J., Removal of BTEX Compounds From Waste Gases; Destruction and Recovery Techniques. *Crit. Rev. Env. Sci. Tec.* **2013**, *43*, 1417-1445.
142. Lin, C. W.; Liu, Y. L.; Thangamuthu, R., Investigation of the relationship between surface thermodynamics of the chemically synthesized polypyrrole films and their gas-sensing responses to BTEX compounds. *Sens. Actuat. B-Chem.* **2003**, *94*, 36-45.
143. Bahrami, M.; Pirmohammadi, Z.; Bahrami, A., A review of new adsorbents for separation of BTEX biomarkers. *Biomed. Chromatogr.* **2021**.
144. Zhu, L. L.; Shen, D. K.; Luo, K. H., A critical review on VOCs adsorption by different porous materials: Species, mechanisms and modification methods. *J. Hazard. Mater.* **2020**, *389*.
145. Anjum, H.; Johari, K.; Gnanasundaram, N.; Ganesapillai, M.; Arunagiri, A.; Regupathi, I.; Thanabalan, M., A review on adsorptive removal of oil pollutants (BTEX) from wastewater using carbon nanotubes. *J. Mol. Liq.* **2019**, *277*, 1005-1025.
146. Mukherjee, S.; Sensharma, D.; Qazvini, O. T.; Dutta, S.; Macreadie, L. K.; Ghosh, S. K.; Babarao, R., Advances in adsorptive separation of benzene and cyclohexane by metal-organic framework adsorbents. *Coordin. Chem. Rev.* **2021**, *437*.
147. Lian, Q. Y.; Konggidinata, M. I.; Ahmad, Z. U.; Gang, D. D.; Yao, L. G.; Subramaniam, R.; Revellame, E.; Holmes, W. B.; Zappi, M., Combined effects of textural and surface properties of modified ordered mesoporous carbon (OMC) on BTEX adsorption. *J. Hazard. Mater.* **2019**, *377*, 381-390.
148. Liu, G. Q.; Wan, M. X.; Huang, Z. H.; Kang, F. Y., Preparation of graphene/metal-organic composites and their adsorption performance for benzene and ethanol. *New Carbon Mater.* **2015**, *30*, 566-571.

149. Karimnezhad, L.; Haghghi, M.; Fatehifar, E., Adsorption of benzene and toluene from waste gas using activated carbon activated by ZnCl₂. *Front. Env. Sci. Eng.* **2014**, *8*, 835-844.
150. Vohra, M. S., Adsorption-Based Removal of Gas-Phase Benzene Using Granular Activated Carbon (GAC) Produced from Date Palm Pits. *Arab. J. Sci. Eng.* **2015**, *40*, 3007-3017.
151. Khan, A.; Szulejko, J. E.; Samaddar, P.; Kim, K. H.; Liu, B. T.; Maitlo, H. A.; Yang, X.; Ok, Y. S., The potential of biochar as sorptive media for removal of hazardous benzene in air. *Chem. Eng. J.* **2019**, *361*, 1576-1585.
152. Yu, L.; Wang, L.; Xu, W. C.; Chen, L. M.; Fu, M. L.; Wu, J. L.; Ye, D. Q., Adsorption of VOCs on reduced graphene oxide. *J. Environ. Sci.* **2018**, *67*, 171-178.
153. Deng, L. L.; Yuan, P.; Liu, D.; Annabi-Bergaya, F.; Zhou, J. M.; Chen, F. R.; Liu, Z. W., Effects of microstructure of clay minerals, montmorillonite, kaolinite and halloysite, on their benzene adsorption behaviors. *Appl. Clay. Sci.* **2017**, *143*, 184-191.
154. Yuan, W. W.; Yuan, P.; Liu, D.; Deng, L. L.; Zhou, J. M.; Yu, W. B.; Chen, F. R., A hierarchically porous diatomite/silicalite-1 composite for benzene adsorption/desorption fabricated via a facile pre-modification in situ synthesis route. *Chem. Eng. J.* **2016**, *294*, 333-342.
155. Yu, W. B.; Deng, L. L.; Yuan, P.; Liu, D.; Yuan, W. W.; Chen, F. R., Preparation of hierarchically porous diatomite/MFI-type zeolite composites and their performance for benzene adsorption: The effects of desilication. *Chem. Eng. J.* **2015**, *270*, 450-458.
156. Zhu, M. P.; Hu, P.; Tong, Z. F.; Zhao, Z. X.; Zhao, Z. X., Enhanced hydrophobic MIL(Cr) metal-organic framework with high capacity and selectivity for benzene VOCs capture from high humid air. *Chem. Eng. J.* **2017**, *313*, 1122-1131.
157. Kim, B.; Lee, Y. R.; Kim, H. Y.; Ahn, W. S., Adsorption of volatile organic compounds over MIL-125-NH₂. *Polyhedron.* **2018**, *154*, 343-349.
158. Long, C.; Li, Y.; Yu, W. H.; Li, A. M., Removal of benzene and methyl ethyl ketone vapor: Comparison of hypercrosslinked polymeric adsorbent with activated carbon. *J. Hazard. Mater.* **2012**, *203*, 251-256.
159. Wang, J. H.; Wang, W. Q.; Hao, Z. P.; Wang, G.; Li, Y.; Chen, J. G.; Li, M. M.; Cheng, J.; Liu, Z. T., A superhydrophobic hyper-cross-linked polymer synthesized

at room temperature used as an efficient adsorbent for volatile organic compounds. *Rsc Adv.* **2016**, *6*, 97048-97054.

160. Wang, X. J.; Ma, C.; Xiao, J.; Xia, Q. B.; Wu, J. L.; Li, Z., Benzene/toluene/water vapor adsorption and selectivity of novel C-PDA adsorbents with high uptakes of benzene and toluene. *Chem. Eng. J.* **2018**, *335*, 970-978.

161. Yang, X.; Yi, H. H.; Tang, X. L.; Zhao, S. Z.; Yang, Z. Y.; Ma, Y. Q.; Feng, T. C.; Cui, X. X., Behaviors and kinetics of toluene adsorption-desorption on activated carbons with varying pore structure. *J. Environ. Sci.* **2018**, *67*, 104-114.

162. Li, L. Q.; Sun, Z.; Li, H. L.; Keener, T. C., Effects of activated carbon surface properties on the adsorption of volatile organic compounds. *J. Air Waste Manage.* **2012**, *62*, 1196-1202.

163. Hsi, H. C.; Horng, R. S.; Pan, T. A.; Lee, S. K., Preparation of Activated Carbons from Raw and Biotreated Agricultural Residues for Removal of Volatile Organic Compounds. *J. Air Waste Manage.* **2011**, *61*, 543-551.

164. Hu, L. J.; Peng, Y.; Wu, F.; Peng, S. Z.; Li, J. J.; Liu, Z. Z., Tubular activated carbons made from cotton stalk for dynamic adsorption of airborne toluene. *J. Taiwan Inst. Chem. E.* **2017**, *80*, 399-405.

165. Yu, X. N.; Liu, S. J.; Lin, G. X.; Zhu, X. C.; Zhang, S.; Qu, R. Y.; Zheng, C. H.; Gao, X., Insight into the significant roles of microstructures and functional groups on carbonaceous surfaces for acetone adsorption. *Rsc Adv.* **2018**, *8*, 21541-21550.

166. Zhu, J. X.; Zhang, P.; Wang, Y. B.; Wen, K.; Su, X. L.; Zhu, R. L.; He, H. P.; Xi, Y. F., Effect of acid activation of palygorskite on their toluene adsorption behaviors. *Appl. Clay. Sci.* **2018**, *159*, 60-67.

167. Chu, F. C.; Zheng, Y.; Wen, B. Y.; Zhou, L.; Yan, J.; Chen, Y. L., Adsorption of toluene with water on zeolitic imidazolate framework-8/graphene oxide hybrid nanocomposites in a humid atmosphere. *Rsc Adv.* **2018**, *8*, 2426-2432.

168. Nien, K. C.; Chang, F. T.; Chang, M. B., Adsorption of mesitylene via mesoporous adsorbents. *J. Air Waste Manage.* **2017**, *67*, 1319-1327.

169. Sui, H.; Liu, H. X.; An, P.; He, L.; Li, X. G.; Cong, S., Application of silica gel in removing high concentrations toluene vapor by adsorption and desorption process. *J. Taiwan Inst. Chem. E.* **2017**, *74*, 218-224.

170. Vellingiri, K.; Kumar, P.; Deep, A.; Kim, K. H., Metal-organic frameworks for the adsorption of gaseous toluene under ambient temperature and pressure. *Chem. Eng. J.* **2017**, *307*, 1116-1126.
171. Hu, L. Q.; Jia, F. C.; Wang, S.; Shao, X. Y.; Wang, X. M.; Sun, Y. P.; Yin, G. C.; Zhou, T.; Rajan, R.; Feng, Z. Y.; Liu, B., The nano-composite of Co-doped g-C₃N₄ and ZnO sensors for the rapid detection of BTEX gases: stability studies and gas sensing mechanism. *J. Mater. Sci.* **2021**, *56*, 5041-5052.
172. Kang, Y.; Kim, K.; Cho, B.; Kwak, Y.; Kim, J., Highly Sensitive Detection of Benzene, Toluene, and Xylene Based on CoPP-Functionalized TiO₂ Nanoparticles with Low Power Consumption. *Acs Sens.* **2020**, *5*, 754-763.
173. Arockiam, C. J.; Rajalakshmi, A.; Parthasarathy, S.; Akshay, K., Room temperature selective sensing of benzene vapor molecules using mixed oxide thin film of zinc oxide and cadmium oxide. *Mater. Sci. Semicond. Process.* **2021**, *132*, 105930.
174. Moon, Y. K.; Jeong, S. Y.; Jo, Y. M.; Jo, Y. K.; Kang, Y. C.; Lee, J. H., Highly Selective Detection of Benzene and Discrimination of Volatile Aromatic Compounds Using Oxide Chemiresistors with Tunable Rh-TiO₂ Catalytic Overlayers. *Adv. Sci.* **2021**, *8*.
175. Im, J.; Sterner, E. S.; Swager, T. M., Integrated Gas Sensing System of SWCNT and Cellulose Polymer Concentrator for Benzene, Toluene, and Xylenes. *Sens. (Basel)*. **2016**, *16*.
176. Luo, S. X. L.; Lin, C. J.; Ku, K. H.; Yoshinaga, K.; Swager, T. M., Pentiptycene Polymer/Single-Walled Carbon Nanotube Complexes: Applications in Benzene, Toluene, and o-Xylene Detection. *Acs Nano*. **2020**, *14*, 7297-7307.
177. Sarkar, T.; Srinives, S., Single-walled carbon nanotubes-calixarene hybrid for sub-ppm detection of NO₂. *Microelectron. Eng.* **2018**, *197*, 28-32.
178. Sarkar, T.; Ashraf, P. M.; Srinives, S.; Mulchandani, A., Calixarene-functionalized single-walled carbon nanotubes for sensitive detection of volatile amines. *Sens. Actuat. B-Chem.* **2018**, *268*, 115-122.
179. Ndiaye, A. L.; Brunet, J.; Varenne, C.; Pauly, A., Functionalized CNTs-Based Gas Sensors for BTX-Type Gases: How Functional Peripheral Groups Can Affect the Time Response through Surface Reactivity. *J. Phys. Chem. C.* **2018**, *122*, 21632-21643.

180. Ndiaye, A.; Bonnet, P.; Pauly, A.; Dubois, M.; Brunet, J.; Varenne, C.; Guerin, K.; Lauron, B., Noncovalent Functionalization of Single-Wall Carbon Nanotubes for the Elaboration of Gas Sensor Dedicated to BTX Type Gases: The Case of Toluene. *J. Phys. Chem. C*. **2013**, *117*, 20217-20228.
181. Clement, P.; Korom, S.; Struzzi, C.; Parra, E. J.; Bittencourt, C.; Ballester, P.; Llobet, E., Deep Cavitand Self-Assembled on Au NPs-MWCNT as Highly Sensitive Benzene Sensing Interface. *Adv. Funct. Mater.* **2015**, *25*, 4011-4020.
182. Machin, W. D., Temperature-Dependence of Hysteresis and the Pore-Size Distributions of 2 Mesoporous Adsorbents. *Langmuir*. **1994**, *10*, 1235-1240.
183. Horikawa, T.; Do, D. D.; Nicholson, D., Capillary condensation of adsorbates in porous materials. *Adv. Colloid Interfac.* **2011**, *169*, 40-58.
184. Steiner, T.; Koellner, G., Crystalline Beta-Cyclodextrin Hydrate at Various Humidities - Fast, Continuous, and Reversible Dehydration Studied by X-Ray-Diffraction. *J. Am. Chem. Soc.* **1994**, *116*, 5122-5128.
185. Kauffman, D. R.; Star, A., Carbon nanotube gas and vapor sensors. *Angew. Chem. Int. Ed.* **2008**, *47*, 6550-6570.
186. *Chemical Sensors: nanostructured materials*. Momentum Press: New York, 2010; Vol. 2, p 300.
187. Wei, P. R.; Leng, H. M.; Chen, Q. Y.; Adyincula, R. C.; Pentzer, E. B., Reprocessable 3D-Printed Conductive Elastomeric Composite Foams for Strain and Gas Sensing. *Acs Appl. Polym. Mater.* **2019**, *1*, 885-892.
188. Yuan, H. Y.; Li, N. X.; Linghu, J. J.; Dong, J. Q.; Wang, Y. X.; Karmakar, A.; Yuan, J. R.; Li, M. S.; Buenconsejo, P. J. S.; Liu, G. L.; Cai, H.; Pennycook, S. J.; Singh, N.; Zhao, D., Chip-Level Integration of Covalent Organic Frameworks for Trace Benzene Sensing. *Acs Sens.* **2020**, *5*, 1474-1481.
189. Substance Safety Data Sheet, Benzene. <https://www.osha.gov/laws-regs/regulations/standardnumber/1910/1910.1028AppA> (accessed July 7, 2021).
190. Buskes, M. J.; Blanco, M. J., Impact of Cross-Coupling Reactions in Drug Discovery and Development. *Molecules*. **2020**, *25*.

191. Chung, C. K.; Bulger, P. G.; Kosjek, B.; Belyk, K. M.; Rivera, N.; Scott, M. E.; Humphrey, G. R.; Limanto, J.; Bachert, D. C.; Emerson, K. M., Process Development of C-N Cross-Coupling and Enantioselective Biocatalytic Reactions for the Asymmetric Synthesis of Niraparib. *Org. Process Res. Dev.* **2014**, *18*, 215-227.
192. Jie, K. C.; Zhou, Y. J.; Sun, Q.; Li, B.; Zhao, R.; Jiang, D. E.; Guo, W.; Chen, H.; Yang, Z. Z.; Huang, F. H.; Dai, S., Mechanochemical synthesis of pillar[5]quinone derived multi-microporous organic polymers for radioactive organic iodide capture and storage. *Nature Communications.* **2020**, *11*.
193. Dai, D. H.; Yang, J.; Zou, Y. C.; Wu, J. R.; Tan, L. L.; Wang, Y.; Li, B.; Lu, T.; Wang, B.; Yang, Y. W., Macrocyclic Arenes-Based Conjugated Macrocyclic Polymers for Highly Selective CO₂ Capture and Iodine Adsorption. *Angew. Chem. Int. Ed.* **2021**, *60*, 8967-8975.
194. Su, K. Z.; Wang, W. J.; Li, B. B.; Yuan, D. Q., Azo-Bridged Calix[4]resorcinarene-Based Porous Organic Frameworks with Highly Efficient Enrichment of Volatile Iodine. *Acs Sustain. Chem. Eng.* **2018**, *6*, 17402-17409.
195. Inoue, Y.; Hakushi, T.; Liu, Y.; Tong, L. H.; Shen, B. J.; Jin, D. S., Thermodynamics of Molecular Recognition by Cyclodextrins .1. Calorimetric Titration of Inclusion Complexation of Naphthalenesulfonates with Alpha-Cyclodextrin, Beta-Cyclodextrin, and Gamma-Cyclodextrin - Enthalpy Entropy Compensation. *J. Am. Chem. Soc.* **1993**, *115*, 475-481.
196. Qian, Q. H.; Asinger, P. A.; Lee, M. J.; Han, G.; Rodriguez, K. M.; Lin, S.; Benedetti, F. M.; Wu, A. X.; Chi, W. S.; Smith, Z. P., MOF-Based Membranes for Gas Separations. *Chem. Rev.* **2020**, *120*, 8161-8266.
197. Zhang, L.; Li, L. L.; Liu, N. J.; Chen, H. L.; Pan, Z. R.; Lue, S. J., Pervaporation Behavior of PVA Membrane Containing beta-Cyclodextrin for Separating Xylene Isomeric Mixtures. *Aiche J.* **2013**, *59*, 604-612.
198. Takaba, H.; Way, J. D., Separation of isomeric xylenes using cyclodextrin-modified ceramic membranes. *Ind. Eng. Chem. Res.* **2003**, *42*, 1243-1252.
199. Chen, H. L.; Wu, L. G.; Tan, J.; Zhu, C. L., PVA membrane filled beta-cyclodextrin for separation of isomeric xylenes by pervaporation. *Chem. Eng. J.* **2000**, *78*, 159-164.